

UC Davis

UC Davis Electronic Theses and Dissertations

Title

Structural Determinants of Voltage-Gated Ion Channel Modulation by Invertebrate Toxins

Permalink

<https://escholarship.org/uc/item/1b94g3nf>

Author

Kimball, Ian H

Publication Date

2021

Peer reviewed|Thesis/dissertation

Structural Determinants of Voltage-Gated Ion
Channel Modulation by Invertebrate Toxins

By

IAN HOWARD KIMBALL
DISSERTATION

Submitted in partial satisfaction of the requirements for the degree of

DOCTOR OF PHILOSOPHY

in

Molecular, Cellular and Integrative Physiology

in the

OFFICE OF GRADUATE STUDIES

of the

UNIVERSITY OF CALIFORNIA

DAVIS

Approved:

Vladimir Yarov-Yarovoy, Chair

Jon Sack

Heike Wulff

Committee in Charge

2021

Table of Contents

Dedication...vi

Abstract...vii

Chapter 1. Synthetic analogues of the snail toxin 6-bromo-2-mercaptotryptamine dimer (BrMT) reveal that lipid bilayer perturbation does not underlie its modulation of voltage-gated potassium channels...1

Introduction...3

Materials and Methods...4

Results...4

Synthesis of Novel BrMT Analogues...4

BrMT Derivatization Alters the Potency of Ion Channel Modulation...6

BrMT Derivatization Alters Bilayer Partitioning, but Partitioning Does Not Predict Ion Channel Modulation...7

Membrane Perturbation by BrMT Derivatives Is Not Correlated with Bilayer Partitioning...8

Potency of Channel Modulation is Not Dictated by Bilayer Perturbation...9

Discussion...9

Limitations...9

Implications...10

BrMT Analogues as Research Tools...10

Author Information...10

Acknowledgements...10

References...11

Electrophysiology Methods...15

Chapter 2. Molecular Determinants of μ -Conotoxin KIIIA interaction with the Voltage-Gated Sodium Channel Nav1.7...17

Abstract...18

Introduction...19

Results...21

Molecular modeling reveals asymmetric binding of KIIIA to hNav1.7 pore...21

Pairwise interactions identified from the KIIIA - hNav1.7 complex model...22

Functional mapping of KIIIA residues at toxin – channel interface...23

Functional mapping of hNav1.7 residues at toxin – channel interface...25

Double Mutant Cycle Analysis of Key pairwise interactions between KIIIA and hNav1.7...26

Marked difference for KIIIA binding specificity among Nav channel isoforms...28

Difference in structural dynamics of KIIIA binding to hNav1.7 and hNav1.2 revealed by molecular dynamics simulations...30

Discussion...33

Conclusions...35

Acknowledgements...35

Materials and Methods...37

Homology modeling of hNav1.7 based on EeNav1.4 structure...37

Molecular docking of KIIIA to the hNav1.7 model...37
Molecular dynamics simulation of hNav1.7-KIIIA and hNav1.2-KIIIA complexes....38
Cell culture and preparation....39
Toxin preparation...40
Electrophysiology...40
Data analysis...42
Equations...42
Figures...44
References...54

Chapter 3. Structural modeling of Nav1.7 DIV voltage-sensor and docking of spider toxin modulators...57

Abstract...58
Introduction...59
Results and Discussion...64
Electrophysiological characterization of SGTx-1 activity on hNav1.7...64
State-modeling of Nav1.7 VSDIV...65
State-dependent docking of spider toxins to VSDIV models highlight potential contacts....66
Structural alignment of related toxins Pn3a and SGTx-1 reveals key differences at putative binding interface...69
Conclusions...70

Acknowledgements...	70
Methods...	71
Cell culture, transfection, and preparation...	71
Electrophysiology...	71
Electrophysiology analysis...	73
Modeling of the Nav1.7 VSD-IV activated and resting states...	74
Docking of SGTx1 to the hNav1.7-VSDIV resting state model...	75
EM-density guided docking of ProTx-II to the hNav1.7-VSDIV activated state...	75
Figures...	76
References...	85

This work is dedicated:

To my loving wife, Kilianne. Without her steady determination to push me closer to my potential, this would never have been possible.

To our children Ethan, Mila, and Ewan. Watching them face and overcome the daily challenges of childhood in an increasingly uncertain world inspires me every day.

To my parents and parents-in-law who have always supported me, and were always there to pick up the slack, or kids, when experiments ran late and deadlines loomed.

To my Yarov-Yarovoy lab mates T, Drew, and Jan, whose many hours of discussion, distraction and all-important Scrubs breaks helped smooth the path of discovery.

To the rest of the Sack-Yarov-Yarovoy lab who have consistently been the best group of people I have ever worked with.

To Ken, who never got mad for pestering him with questions, and who would have finished my first chapter much faster than I did.

To Jon and Vladimir, whose guidance, motivation, patience, and infectious love of science made this happen, and who make me proud to have been a member of their lab.

Abstract

Animals from cockroaches to humans, utilize electrochemical gradients to perform rapid, long-distance communication between cells like neurons and muscle for these functions, requiring the coordinated action of voltage-gated ion channels (VGICs). Such channels allow for the selective transport of ions down their individual electrochemical gradients and act *en masse* to control the voltage of the cell promoting further propagation of an electrical signal, or the triggering of other signaling processes. Two classes of VGIC, voltage-gated potassium (Kv) and voltage-gated sodium (Nav) channels are found throughout excitable tissues such as neurons, skeletal and cardiac muscle, and are particularly responsible for the outward and inward currents of action potentials, respectively. While these channel types share structural homology, the presence or absence of different domains and variations in their amino acid sequences lead to drastic differences in their function, and their concerted action is necessary for proper cell function. This variability is further compounded by differential tissue expression of Nav and Kv channel subtypes, leading to more specific physiological and pathophysiological roles. To better understand these channels and their roles in normal and disease states, we require targeted pharmacological tools and a knowledge of the structural underpinnings of their mode of action. The importance of VGICs can be further demonstrated by the ubiquity of toxins produced by organisms from dinoflagellates (saxitoxin) to venomous snakes (α -bungarotoxin) that target ion channel function to alter the behavior of animal predators and prey alike. These toxins provide molecular tools for understanding the mechanisms of ion channel function and potential therapeutics for treating diseases either caused or affected by aberrant ion channel activity. Such toxins can be small molecules or peptide toxins and can act on a wide variety of VGICs or selectively target certain channel subtypes with high specificity. The diversity of channel

sensitivities to such toxins is matched in the diversity of mechanisms by which these toxins act; they can bind to the conducting pore of the channel, bind to voltage sensing domains altering the kinetics of channel voltage sensitivity, and can even alter the properties of the cell membrane to affect channel function.

I have studied the structural elements driving the modulation of two different ion channels by molecules from invertebrates and their derivatives. Two of the three invertebrate toxins, a small molecule toxin and a peptide toxin, were produced by marine snails and have the ability to alter the function of vertebrate VGICs either for defense or predation. The other is a peptide toxin found in the venom of a tarantula used both defensively and to immobilize prey. Such toxins selectively target voltage-gated ion channels to disrupt the normal motor function or produce pain in their victims. The two channels are involved in very different physiological roles: Kv1.4 is found in cardiac myocytes and is responsible for the transient outward current (I_{to1}) during the phase 1 repolarization of ventricular myocytes; Nav1.7 is found in the fibers of dorsal root ganglion neurons and known to be important in the generation of action potentials important in pain signaling.

My Thesis is divided into 3 chapters that combine high-throughput and traditional electrophysiology experiments with computational modeling to study the molecular interactions of toxins and ion channels. While the relationship between structure and function is central to physiology in general, it is especially important in determining molecular mechanisms, potency, and selectivity of ion-channel modulators for specific targets. In Chapter 1 we examined how the structure of toxin derivatives affected their ability to partition and perturb membranes, and used high-throughput electrophysiology to determine how this translated to effects on channel function. In Chapters 2 and 3 we utilized predictive modelling of Nav1.7 channel structure to

identify potential toxin binding modes and unseen states of channel domains. The recent explosion of structural data available for membrane proteins has aided in understanding of how channels work, and provided new avenues for modeling of channel-toxin interactions. Experimental validation of such models furthers our structural knowledge of these channels and their molecular mechanisms of modulation, and provides opportunities for designing novel molecular tools for study.

The first chapter of my thesis documents the study of a small molecule inhibitor of Kv1.4— 6-Bromo-2-mercaptotryptamine (BrMT) and its derivatives that alter the kinetics of channel activation. In this study we developed a method for distinguishing between the effects of membrane perturbation and direct interaction with ion channels in understanding the mechanism of ion channel toxins. As a part of a multi-assay structure-activity study, I performed an electrophysiology assay to determine the sensitivity of Kv1.4 channel currents in exogenously expressing Chinese Hamster Ovary (CHO) cells to toxin derivatives. Derivatives were synthesized to create greater stability than the native toxin and alter its potential to interact with the cell membrane. These modifications consisted of multiple substituted sidechains and linkages that affected the hydrophobicity and geometry allowing for a structure-activity relationship on these measures to be determined. Seeking to identify the contribution of these substitutions to their efficacy against Kv1.4 I conducted concentration response experiments examining both the efficacy of these variants and changes in the apparent kinetics of channel activation in response to depolarizing voltage steps with toxin present. I compared the results of my assay with those of measures of membrane partitioning and perturbation to assess the role of these factors in affecting channel function in the presence of toxin. While certain chemical groups affected

membrane partitioning and perturbation, the observed effects on the channels could not be explained by the effect on membrane perturbation alone, suggesting direct interactions with the channel were influenced by toxin structure. These findings can help the future study of the mechanisms of ion channel-toxin interactions and enable the design of novel therapeutics from toxin scaffolds.

My second chapter details the search for an accurate model of the interaction of the small cyclic peptide conotoxin, KIIIA, with the voltage-gate sodium channel Nav1.7 to guide the future design of novel inhibitors of the channel. Lacking crystallographic or cryo-EM data on the structure of Nav1.7, we used homology modeling to identify contacts between the channel and toxin residues. I performed an electrophysiological assay to determine the association and dissociation kinetics of toxin variants with key residues. These variants were chosen in concert with corresponding mutations in the channel to remove contacts identified from previous studies and our modeling efforts. Double-mutant cycle analysis, a comparison of the toxin affinities from single mutant (toxin or channel) and double mutant (toxin and channel) conditions, allowed us to identify energetic contributions of the interactions between basic residues on the toxin with acidic residues on the outer channel pore. The orientation of the toxin in our computational model was further corroborated by molecular dynamics simulations. With this combined approach we were able to independently produce a well-supported model of the toxin binding to the outer pore of the channel that comports with recently published structure of the Nav1.2-KIIIA complex. Our model provides insight into potential mechanism of channel block and specificity, while providing a scaffold for future design of novel channel inhibitors for the treatment and study of Nav1.7-associated disorders. I assisted in the study design, prepared test

solutions, performed the electrophysiology experiments and data analysis and writing and editing all sections of the manuscript.

My third chapter describes my efforts to characterize multiple states of the Domain IV voltage sensor (DIV-VSD) of the voltage-gated sodium channel Nav1.7, and its potential interaction with the peptide tarantula toxin SGTx-1, and the spider toxin ProTx-II. The DIV-VSD of Nav channels is known to be important for the channel fast-inactivation leading to rapid reduction in Na⁺ conduction following depolarizing voltages. The crucial role of this voltage-sensing domain has made it a target of researchers aiming to control Na⁺ conductance and is a known binding site of a class of scorpion toxins and new small-molecule inhibitors. The discovery that the tarantula toxin SGTx-1 could inhibit Nav1.2-DIV-VSD movement provides a potential smaller toxin for redesign of a Nav1.7-DIV-VSD-selective tool. I performed electrophysiological experiments that revealed a slowing of channel kinetics that could be explained by the toxin stabilizing a resting state of the Domain IV VSD as had been suggested for Nav1.2. I modeled active and resting states of the channel based on published structures of homologous ion channels and performed *in silico* docking of the toxin to identify potential points of contact between the channel and toxin. Candidate residues based on my docking results comport with findings of mutagenesis studies on toxin binding to the potassium channel Kv2.1. I further examined the interaction of the toxin ProTx-II with an active state of the Nav1.7-DIV-VSD guided by recently published density map data. I performed all structural modeling, electrophysiological experiments, data analysis, and writing in this study.

CHAPTER 1

Synthetic analogues of the snail toxin 6-bromo-2-mercaptotryptamine dimer (BrMT) reveal that lipid bilayer perturbation does not underlie its modulation of voltage-gated potassium channels

This chapter contains my research investigating whether a series of snail toxin derivatives inhibit ion channels by interacting with an ion channel protein or the lipid membrane in which it is embedded.

Published in 2018 as:

Dockendorff C, Gandhi DM, **Kimball IH**, Eum KS, Rusinova R, Ingolfsson HI, Kapoor R, Peyear T, Dodge MW, Martin SF, Aldrich RW, Andersen OS, Sack JT. Synthetic analogues of the snail toxin 6-bromo-2-mercaptotryptamine dimer (BrMT) reveal that lipid bilayer perturbation does not underlie its modulation of voltage-gated potassium channels.

Biochemistry 57: 2733-2743

I conducted electrophysiology experiments, analyzed data, and wrote for the following sections:

BrMT Derivatization Alters the Potency of Ion Channel Modulation.

Figure 2. Structure–activity relationship of Kv1.4 inhibition

BrMT Derivatization Alters Bilayer Partitioning, But Partitioning Does Not Predict Ion Channel Modulation

Figure 3. Membrane partition coefficients do not predict channel inhibition

Membrane Perturbation by BrMT Derivatives Is Not Correlated with Bilayer Partitioning

Figure 4. Membrane perturbation is distinct from partitioning and does not predict channel inhibition

Potency of Channel Modulation is Not Dictated by Bilayer Perturbation

Figure 4. Membrane perturbation is distinct from partitioning and does not predict channel inhibition

Figure S1. Representative Kv1.4 current responses to modulators

Synthetic Analogues of the Snail Toxin 6-Bromo-2-mercaptotryptamine Dimer (BrMT) Reveal That Lipid Bilayer Perturbation Does Not Underlie Its Modulation of Voltage-Gated Potassium Channels

Chris Dockendorff,^{*,†} Disha M. Gandhi,[†] Ian H. Kimball,[‡] Kenneth S. Eum,^{‡,#} Radda Rusinova,[‡] Helgi I. Ingólfsson,[‡] Ruchi Kapoor,[‡] Thasin Peyear,[‡] Matthew W. Dodge,[‡] Stephen F. Martin,[‡] Richard W. Aldrich,[§] Olaf S. Andersen,^{*,‡} and Jon T. Sack^{*,†}

[†]Department of Chemistry, Marquette University, P.O. Box 1881, Milwaukee, Wisconsin 53201-1881, United States

[‡]Department of Physiology & Membrane Biology, University of California, 1 Shields Avenue, Davis, California 95616, United States

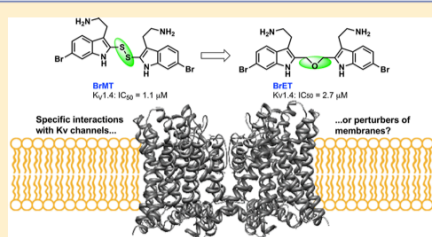
[§]Department of Neuroscience, University of Texas at Austin, 1 University Station, Austin, Texas 78712, United States

^{||}Department of Chemistry, University of Texas at Austin, 1 University Station, Austin, Texas 78712, United States

[⊥]Department of Physiology and Biophysics, Weill Cornell Medical College, New York, New York 10065, United States

Supporting Information

ABSTRACT: Drugs do not act solely by canonical ligand–receptor binding interactions. Amphiphilic drugs partition into membranes, thereby perturbing bulk lipid bilayer properties and possibly altering the function of membrane proteins. Distinguishing membrane perturbation from more direct protein–ligand interactions is an ongoing challenge in chemical biology. Herein, we present one strategy for doing so, using dimeric 6-bromo-2-mercaptotryptamine (BrMT) and synthetic analogues. BrMT is a chemically unstable marine snail toxin that has unique effects on voltage-gated K⁺ channel proteins, making it an attractive medicinal chemistry lead. BrMT is amphiphilic and perturbs lipid bilayers, raising the question of whether its action against K⁺ channels is merely a manifestation of membrane perturbation. To determine whether medicinal chemistry approaches to improve BrMT might be viable, we synthesized BrMT and 11 analogues and determined their activities in parallel assays measuring K⁺ channel activity and lipid bilayer properties. Structure–activity relationships were determined for modulation of the Kv1.4 channel, bilayer partitioning, and bilayer perturbation. Neither membrane partitioning nor bilayer perturbation correlates with K⁺ channel modulation. We conclude that BrMT’s membrane interactions are not critical for its inhibition of Kv1.4 activation. Further, we found that alkyl or ether linkages can replace the chemically labile disulfide bond in the BrMT pharmacophore, and we identified additional regions of the scaffold that are amenable to chemical modification. Our work demonstrates a strategy for determining if drugs act by specific interactions or bilayer-dependent mechanisms, and chemically stable modulators of Kv1 channels are reported.



Biological membranes are composites of lipid bilayers and embedded proteins. It has long been known that membrane protein function is sensitive to the composition of the host bilayer.^{1–4} Commonly, drugs that modulate membrane proteins are presumed to target proteins, while in fact many act by changing the bulk properties of the host bilayer, thereby altering membrane protein conformational equilibria.^{5–8} Modulators that act by bilayer perturbation promiscuously modulate a broad spectrum of unrelated membrane proteins.^{5,7,9–15} Upon interpretation of the mechanisms underlying the physiological actions of a drug, it thus becomes crucial to determine whether the action of an amphiphilic modulator may

involve bulk bilayer perturbation, in addition to more specific interactions.

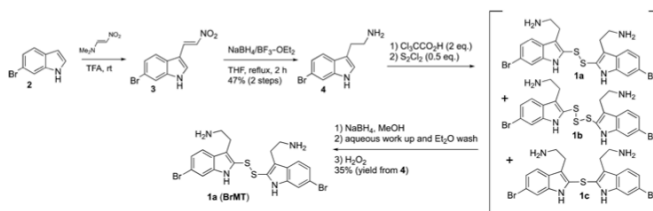
A prominent example of the importance of understanding drug mechanism involves capsaicin, a natural product of chili peppers that stimulates mammalian peripheral neurons to evoke a sensation of burning heat. Capsaicin perturbs bilayers and modulates a wide variety of membrane proteins, including Na⁺, K⁺, and TRP channels. Capsaicin modulates voltage-gated

Received: March 8, 2018

Revised: April 2, 2018

Published: April 4, 2018

Scheme 1. Total Synthesis of BrMT



Na⁺ and K⁺ channels via lipid bilayer perturbation,^{5,7} but capsaicin also has a specific receptor site on TRPV1.¹⁶ Medicinal chemistry approaches have been successful in generating analogues of capsaicin that are selective TRPV1 inhibitors.¹⁷ Similar efforts to selectively modulate Na⁺ or K⁺ channels with capsaicin analogues would be foolhardy, however, because modulation of membrane proteins via bilayer perturbation is fundamentally promiscuous. Thus, determining if lipid bilayer perturbation underlies modulation of a target is critical for the prediction of undesired effects on other membrane proteins.

Because lipophilic and amphiphilic drugs, by their chemical nature, partition into membranes and perturb the function of transmembrane proteins, it is a significant challenge to determine whether bilayer perturbation is the relevant mechanism underlying modulation of any particular target protein. To identify whether drugs operate by a bilayer mechanism, we previously developed a method of testing modulators for promiscuous activity against multiple unrelated classes of membrane proteins.⁷ Although this method is effective, it requires significant resources and expertise with many membrane protein preparations. Herein, we report a greatly simplified strategy for using the structure–activity relationships (SARs) of a modulator against a single target of interest, in combination with synthetic membrane assays, to dissect the effects of bulk bilayer perturbation from those of direct protein binding.

The medicinal chemistry target in this study is the natural product ion channel modulator dimeric 6-bromo-2-mercapto-tryptamine (BrMT, 1a). A component of the defensive mucus of the marine snail *Calliostoma canaliculatum*, it inhibits voltage-gated K⁺ channels of the Kv1 and Kv4 subfamilies.¹⁸ BrMT is an allosteric modulator that inhibits channels by slowing the voltage activation steps that precede pore opening, without blocking the central channel pore.^{19,20} Allosteric modulators of Kv channels are valuable not only as research tools but also potentially as therapeutics.^{21,22} BrMT itself has limited utility because it contains a chemically labile disulfide bond that is degraded by light and reducing conditions.¹⁹ BrMT is thus an attractive target for medicinal chemistry efforts to improve its stability.

Several observations suggest that the activity of BrMT against Kv channels may be affected by nonspecific membrane partitioning. First, high concentrations of BrMT applied to outside-out membrane patches disrupt the patch clamp seal.¹⁹ Second, a series of chimeras between the BrMT-sensitive Shaker Kv channel and the insensitive Kv2.1 channel suggest that the region imparting sensitivity is in the S1, S2, and/or S3 transmembrane regions of sensitive channels.²³ Third, the

wash-in and wash-out kinetics of BrMT are multiphasic, suggesting slow accumulation of BrMT in the cell membrane during prolonged exposures.^{23,24} Together, these effects are consistent with BrMT partitioning in and out of cell membranes and acting through the membrane to alter channel function. Similar to many other amphiphilic molecules that act by bilayer perturbation, the biological effect of BrMT, with its two aminoethyl groups, depends on the side of the membrane to which it is applied.^{25–28} BrMT slows Kv channel voltage activation only when applied from the extracellular side of the membrane,¹⁹ suggesting that its two positive charges may prevent it from crossing the membrane entirely. Certain Kv modulator peptides from animal venoms partition into, but do not cross, the outer leaflet of the plasma membrane bilayer. Many of these peptides bind to the transmembrane voltage sensor domains of the channels.^{29–31} However, other closely related venom peptides modulate ion channels via bilayer perturbation.³² It remains unclear whether BrMT modulates K⁺ channels by direct channel binding, by perturbing the bilayer in an indirect manner, or a combination of both.³³ To elucidate the mode of action of BrMT and potentially improve its properties as a lead compound for future mechanistic or therapeutic studies, we synthesized a series of analogues, including several with stable disulfide replacements. The resulting SARs were assessed separately in membrane partitioning, perturbation, and ion channel assays to test whether specific or nonspecific interactions drive K⁺ channel activities with these bis-indole compounds.

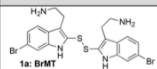
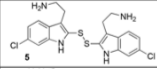
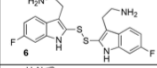
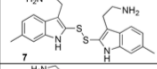
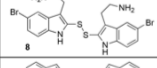
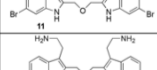
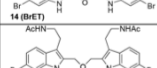
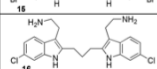
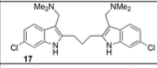
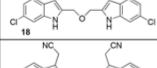
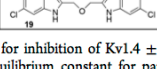
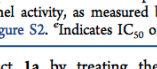
MATERIALS AND METHODS

The Supporting Information contains detailed descriptions of the synthesis of all BrMT analogues, cell culture, electrophysiology, gramicidin-based fluorescence quench assay, and isothermal titration calorimetry.

RESULTS

Synthesis of Novel BrMT Analogues. To determine the minimal structural features required for modulation of Kv channels with BrMT (1a), we designed a flexible synthesis that would enable facile modification of the tryptamine scaffold as well as the disulfide linker (Scheme 1). Our synthetic route is similar to that reported by Gallin and Hall.³⁴ 6-Bromotryptamine (4) was prepared from 6-bromoindole according to the sequence reported by Davidson.³⁵ Protonation of 4 with trichloroacetic acid,^{36,37} yielded a mixture of mono-, di-, and trisulfides 1a–c that was characterized by LC-MS. Using a protocol reported by Showalter for the preparation of bisindole diselenides as tyrosine kinase inhibitors,³⁸ we increased the yield of the

Table 1. Compilation of Properties of BrMT Derivatives

Structure	IC ₅₀ (μM) ^a	Hill coeff. ^a	ClogP ^b	K _p ^{N→L, c}	gA ₂ (μM) ^d
 1a: BrMT	1.1 ± 0.1 N = 10	1.7 ± 0.3 N = 10	5.32	560 ± 5 N = 3	40 ± 5 N = 3
 5	0.8 ± 0.2 N = 10	1.4 ± 0.3 N = 10	4.99	1000 ± 200 N = 5	13 ± 1 N = 3
 6	26 ± 9 N = 9	1.1 ± 0.5 N = 9	4.06	800 ± 200 N = 5	28 ± 1 N = 3
 7	2.1 ± 0.2 N = 21	1.8 ± 0.2 N = 21	4.81	450 ± 80 N = 4	12 ± 1 N = 3
 8	2.1 ± 0.2 N = 7	1.3 ± 0.2 N = 7	5.32	1900 ± 600 N = 4	inactive ^e (50 μM) N = 3
 11	inactive ^e (100 μM) N = 8	–	5.15	600 ± 200 N = 4	inactive ^e (50 μM) N = 3
 14 (BrET)	2.7 ± 0.3 N = 23	1.9 ± 0.3 N = 23	3.98	3100 ± 700 N = 3	2.9 ± 0.2 N = 3
 15	70 ± 30 N = 10	0.7 ± 0.2 N = 10	3.62	3900 ± 500 N = 4	1.9 ± 0.1 N = 3
 16	2.3 ± 0.3 N = 6	1.8 ± 0.2 N = 6	4.72	3300 ± 800 N = 3	12.8 ± 0.7 N = 3
 17	35 ± 7 N = 8	1.3 ± 0.3 N = 8	5.77	670 ± 90 N = 4	5.1 ± 0.3 N = 3
 18	inactive ^e (25 μM) N = 6	–	4.82	1400 ± 200 N = 4	inactive ^e (50 μM) N = 3
 19	inactive ^e (25 μM) N = 8	–	4.21	3500 ± 1100 N = 3	32 ± 5 N = 3

^aCalculated as the best fit for inhibition of Kv1.4 ± standard deviation of the parameter fit. ^bCalculated using ChemAxon MarvinSketch version 17.4.3.0. ^cK_p^{W→L} is the equilibrium constant for partitioning from water to lipid. Calculated as the geometric mean ± positive standard error. ^dGramicidin A (gA) channel activity, as measured by the rate of quenching of intravesicular ANTS fluorescence by Tl⁺. gA₂ fits are shown in Supporting Information Figure S2. ^eIndicates IC₅₀ or gA₂ was not measured (highest concentration tested in parentheses).

desired disulfide product **1a** by treating the mixture with sodium borohydride to reduce the di- and trisulfides. Extraction of the nonpolar monosulfide **1c** with ether from the basic aqueous solution of the resulting indole-2-thiolate, followed by oxidation of the thiolate with hydrogen peroxide, gave the disulfide **1a**, which was purified by semipreparative HPLC and treated with HCl in dioxane to yield the bis-hydrochloride salt. Five different tryptamines were prepared via variations of literature protocols (see the Supporting Information for details), and these were transformed into the analogous bistryptamine-disulfides **5–8** (Table 1) according to the sequence of reactions in Scheme 1.

The relative instability of bistryptamine-disulfides, and their potential for disulfide exchange reactions *in vivo*,³⁹ inspired us to explore the use of alternative linkers between the indole moieties. Several two-carbon indole linkers have been reported

in the literature,^{40,41} but we expected that these would be too rigid and/or short to be effective disulfide replacements. Accordingly, we pursued a convergent synthesis of symmetrical bis-indoles by reacting suitable aniline derivatives with bis-alkynes. Dipropargyl ether was selected as our first choice, as it could provide a three-atom, ether-based linker between the two indole rings that would provide a distance between indole moieties comparable to that of the disulfide linker.

The optimized synthesis of the ether-linked compounds is given in Scheme 2. Commercially available 4-bromo-2-nitroaniline was subjected to a Sandmeyer reaction⁴² to yield aryl iodide **9d** in 94% yield. The nitro group of **9d** was reduced to aniline **9a** using SnCl₂ and concentrated HCl, followed by *N*-acylation with acetic anhydride to provide the amide **9c**. Amide **9c** was subjected to the double Sonogashira cross coupling conditions (Table S1, entry 7) to yield the bis-alkyne **10c** in

Scheme 2. Synthesis of Ether-Linker Analogues 14 (BrET) and 15

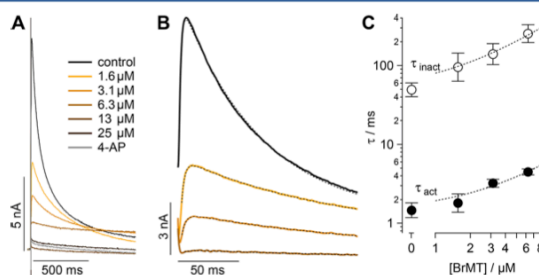
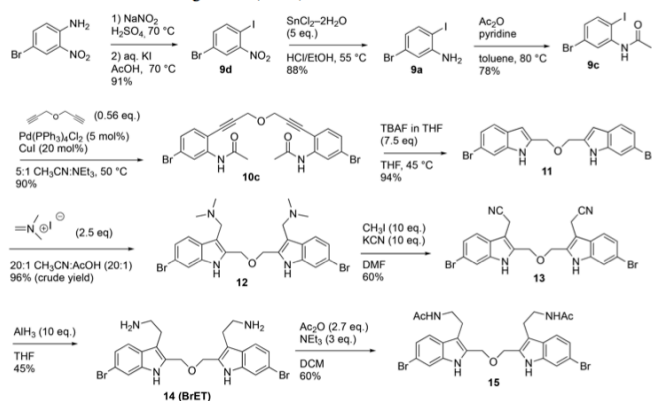


Figure 1. BrMT inhibits Kv1.4 channel activation. (A) Kv1.4 current responses to indicated BrMT concentrations during voltage steps from -100 to 0 mV. (B) Kv1.4 current responses. Colored lines correspond to the same BrMT concentrations as in panel A. Stippled lines are fits of eq 2, in the Supporting Information. Voltage steps from -100 to 0 mV. Vehicle $\tau_{\text{act}} = 1.72 \pm 0.02$, $\tau_{\text{inact}} = 67.3 \pm 0.2$; $1.5 \mu\text{M}$ $\tau_{\text{act}} = 2.54 \pm 0.02$, $\tau_{\text{inact}} = 136.6 \pm 0.6$; $3 \mu\text{M}$ $\tau_{\text{act}} = 3.17 \pm 0.03$, $\tau_{\text{inact}} = 181 \pm 2$; $6 \mu\text{M}$ $\tau_{\text{act}} = 4.2 \pm 0.4$, $\tau_{\text{inact}} = 300 \pm 20$. (C) Time constants of activation (filled circles) and inactivation (empty circles). Error bars indicate SEM ($n = 9$). Stippled lines are fits for K_d , as in ref 19. K_d from $\tau_{\text{act}} = 2.9 \pm 1.0 \mu\text{M}$, and K_d from $\tau_{\text{inact}} = 1.6 \pm 0.7 \mu\text{M}$.

90% yield. Treatment of **10c** with aqueous TBAF followed by amide hydrolysis gave **11** (see SI for details). Alkylation of the bis-indole **11** with Eschenmosher's salt⁴³ gave the bis-gramine **12** in excellent yield. Owing to the potential instability of **12**, it was converted without purification to bis-nitrile **13** upon treatment with excess iodomethane and sodium cyanide in DMF. Reduction of the nitrile groups in **13** with LiAlH_4 was problematic and led to partial reduction of the aryl bromide, but reduction of **13** with alane⁴⁴ proceeded smoothly to give the bis-amine **14** (termed BrET) in 45% yield. Acetylation of **14** with acetic anhydride furnished the bis-amide **15** in 60% yield. The related BrMT analogues **16–19** (Table 1) were prepared by a sequence of reactions similar to those depicted in Scheme 2. Initial attempts to reduce **19** to the corresponding diamine were unsuccessful in generating a compound of acceptable purity.

BrMT Derivatization Alters the Potency of Ion Channel Modulation. We assessed the modulatory effects of BrMT analogues on currents through voltage-gated

potassium channels. To measure the dose–response relations of many compounds in parallel, we developed an automated whole-cell voltage clamp assay against a BrMT-sensitive ion channel. BrMT inhibits Kv1 (Shaker-type) channels from invertebrates and vertebrates.¹⁸ Among members of the Kv1 family, Kv1.4 was chosen because it is a potential target for chronic pain and lacks high-affinity modulators.^{45–48} Moreover, Kv1.4 is transported efficiently and reliably to the plasma membrane in mammalian cell lines, making it optimal for automated electrophysiology.^{49,50} We therefore created a CHO-K1 cell line with a tetracycline-inducible expression of Kv1.4 to provide a scalable cell culture with consistent current levels amenable to automated patch clamp methods.

Amphiphilic drugs often have variable potencies in different experimental preparations. This preparation-dependent variability may stem from membrane partitioning that is sensitive to the exact composition of the cell membrane, solution flow, and other factors.^{24,51,52} Not surprisingly, BrMT has different potencies against Shaker Kv1 channels in patches and whole-

cell voltage clamp of HEK cells, CHO cells, and *Xenopus* oocytes.^{2,5} To serially compare the effects of BrMT derivatives with minimal variability, the assays were conducted with a commercially available automated patch clamp system that applied consistent solution flow for different experiments.

When BrMT was applied to voltage-clamped cells expressing Kv1.4, it inhibited the currents by slowing gating kinetics and reducing peak currents (Figure 1A). The effects of BrMT on kinetics were quantified by fitting a double exponential to the rise and decay of the current after a depolarizing voltage step (Figure 1B). Increasing concentrations of BrMT progressively slowed the gating kinetics (Figure 1C). These effects are similar to those seen with Shaker Kv1 channels.¹⁹ BrMT has two phenomenological effects on Kv1 channels: a slowing of activation kinetics and a diminishment of peak current amplitude after a voltage step.¹⁹ Peak current amplitudes of Kv1.4 are affected more dramatically than the rate of channel activation by BrMT (Figures 1, 2A). This greater sensitivity of the peak amplitudes may be due to a stronger coupling between activation and inactivation in Kv1.4 as compared to Shaker channels.⁵³ For comparison among the BrMT analogues, we therefore used the IC_{50} values determined from the changes in peak current because their fitting was better constrained than the results obtained from the more complex curve fitting procedures needed to analyze the activation kinetics. Modulation of Kv1.4 currents is apparent over a range of concentrations (Figure S1), and IC_{50} estimates were successfully obtained for most BrMT analogues (Figure 2). The Hill slopes deduced from these fits are between 1 and 2 for most analogues. Hill slopes greater than 1 could arise from cooperative interactions of the BrMT analogue with multiple subunits of Kv channels.²⁰ One analogue, 15, has a lower Hill slope, which could indicate that this weakly modulating analogue acts by a different mechanism, but its low potency precludes any significant interpretations.

Factors affecting channel inhibition emerge from analysis of SAR data. Replacement of the 6-bromo moiety of BrMT with a chloro or methyl group as in 5 and 7 had little effect on inhibitor potency, whereas substitution with the smaller and more electronegative fluoro group as in 6 led to a decrease in potency by an order of magnitude ($IC_{50} = 26 \mu\text{M}$). Prior measurements with a BrMT analogue containing only a hydride at position 6 indicated that it was also an order of magnitude less potent than BrMT against Shaker K^+ channels.⁵⁴ Moving the bromo group to the 5-position on the indole ring as in 8 had only a minor effect on potency. These results suggest that variable indole substituents are tolerated.

BrMT loses its potency against Kv channels when the disulfide is reduced to form monomeric compounds.¹⁹ On the other hand, the disulfide linkage between the indole groups is remarkably tolerant to replacement. For example, activity is retained when the disulfide moiety in BrMT is replaced with the ether linkage in 14 or when the disulfide in the 6-chloro-substituted analogue 5 is replaced with the trimethylene linker in 16. The idea that alterations in the linker between the indoles have only mild effects on Kv potency was also reported by Gallin and Hall,³⁴ who found that Kv1 channel inhibition was maintained for 1a–c, wherein the number of sulfur atoms bridging the indole rings was varied from one to three.

The discovery that Kv inhibition is retained with an ether or alkyl linkage between the indole rings permitted additional SAR studies using these more chemically stable scaffolds. We found that compounds 11, 18, and 19, which each lack the aminoethyl

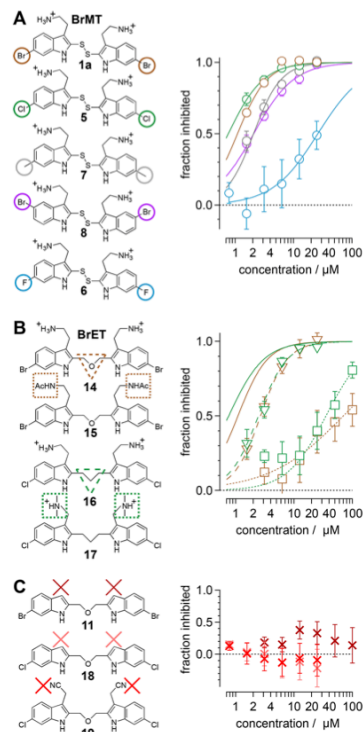


Figure 2. Structure–activity relationship of Kv1.4 inhibition. Average inhibition of peak Kv1.4 currents as a function of concentration. The shapes and colors of markers correspond to compounds with modifications indicated by shapes in the left column. Error bars indicate SEM. Lines are fits of eq 1, in the Supporting Information, with parameter values indicated in Table 1. The color and pattern of lines correspond to compounds with modifications indicated by the shapes in the left column. (A) BrMT and analogues with modifications at the 6-positions on the indole rings. (B) Analogues with modifications of the disulfide linker and amines. (C) Ineffective analogues without aminoethyl groups.

side chain, are inactive at the highest concentrations tested. Moreover, the *N*-acetyl derivative 15 and the *N,N*-dimethylaminoethyl analogue 17 are less potent than the parent compound BrET (14) by more than an order of magnitude. Collectively, these results indicate that modification at the 2- and 6-positions of the indole rings of BrMT is well-tolerated, but the aminoethyl groups at the 3-positions are critical for channel activity: compounds lacking basic side chains at the 3-position were inactive (e.g., 11, 18, and 19).

BrMT Derivatization Alters Bilayer Partitioning, but Partitioning Does Not Predict Ion Channel Modulation. We measured the degree to which the BrMT analogues partition into membranes using isothermal titration calorimetry (ITC).⁵⁵ These experiments were conducted with suspensions

of large unilamellar phospholipid vesicles (LUVs) (see SI) as a surrogate for the bilayer component of cell membranes. All of the analogues partitioned into the bilayer with water → bilayer partition coefficients (K_p^{W-L}) ranging between 450 and 3900 (Table 1); the calculated $\log([n\text{-octanol}]/[\text{water}])$ (ClogP) values are also listed for comparison. K_p^{W-L} values increased when the disulfide linkage was replaced with a three-atom alkyl or an ether linkage. For example, replacing the disulfide linkage of BrMT (1a) ($K_p^{W-L} = 560$) with an ether linkage as in 14 ($K_p^{W-L} = 3100$) led to an increase in K_p^{W-L} values, as did replacing the disulfide bridge of the chloro analogue 5 ($K_p^{W-L} = 1000$) with a trimethylene linkage in 16 ($K_p^{W-L} = 3300$). If channel modulation results from compounds partitioning into the membrane bilayer, we would expect that the Kv1.4 IC_{50} values would correlate with the K_p^{W-L} values, but this is not the case (Figure 3). Examination of small structural changes that

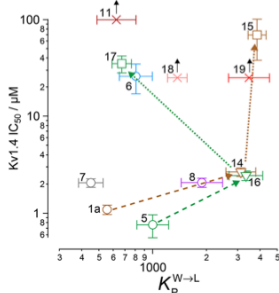


Figure 3. Membrane partition coefficients do not predict channel inhibition. Numbers by each marker denote the analogue identity. The shape and color of markers correspond to Figure 2. Values are from Table 1. Black arrows denote analogues with such a low activity that we could not measure it (null response), with the marker indicating the highest concentration tested. Brown and green arrows with dashed lines indicate modification of the disulfide linker. Brown and green arrows with dotted lines indicate modification of aminoethyl groups.

influence partitioning and/or channel modulation also indicates that the two properties are independent. Replacing the disulfide linkage of BrMT (1a) with the ether moiety in 14 increases K_p^{W-L} values but has little impact on IC_{50} . The acetylated, nonbasic compound 15 has an increased fraction in membranes vs its basic parent 14 ($K_p^{W-L} = 3900$ vs 3100), but its potency against Kv1.4 drops substantially ($IC_{50} = 70 \mu\text{M}$ vs $2.7 \mu\text{M}$) (Figure 3, brown arrows). Replacing the disulfide linkage of 5 with a trimethylene linkage in 16 also increases K_p^{W-L} values with little impact on IC_{50} . Comparison of 16 to the related *N,N*-dimethylaminomethyl compound 17 shows a rare example of a relatively minor structural change that simultaneously decreases both the K_p^{W-L} values and inhibitory potency (Figure 3, green arrows). Overall, increases in the partition coefficient were not coupled to an increase of inhibitory potency. Fitting a linear regression to K_p^{W-L} and IC_{50} values did not yield any significance ($r = 0.34$, $p = 0.37$). The fraction of a BrMT analogue in the bilayer does not correlate with its potency, which suggests that bilayer partitioning is not sufficient for Kv channel modulation.

Membrane Perturbation by BrMT Derivatives Is Not Correlated with Bilayer Partitioning.

Bilayer partitioning itself did not underlie the variable potencies of Kv channel inhibitors, but it remains a possibility that nonspecific bilayer perturbation might affect their inhibition of Kv1.4 because small membrane-perturbing amphiphiles are known to inhibit many Kv channels.⁷ We therefore probed for bilayer-modifying effects using a gramicidin A (gA)-based fluorescence assay that monitors changes of gA activity in LUVs.^{56,57} This assay exploits the gramicidin channel-permeant thallous ion (Tl^+), which quenches the fluorescence of the water-soluble fluorophore 8-aminonaphthalene-1,3,6-trisulfonate (ANTS). gA permits transmembrane Tl^+ flux only as a dimer, and the equilibrium between monomeric and dimeric gA is altered by lipid bilayer perturbation. ANTS fluorescence is measured after addition of Tl^+ to a suspension of ANTS-loaded gA-containing LUVs, and the time course of fluorescence quenching (Figure 4A) provides a measure of the changes in intravesicular $[Tl^+]$. The initial rate of fluorescence quenching provides a measure of the initial rate of Tl^+ influx into the LUVs,^{58–60} which varies with changes in the number of dimeric gA molecules in the LUV membrane. It is thus possible to determine how a drug, or other amphiphile, shifts the gA monomer/dimer equilibrium, which provides a measure of the bilayer-modifying potency of the molecule of interest. The BrMT analogue concentration that elicits a doubling of the rate of gA-dependent quenching is denoted as gA_2 and serves as a metric for the bilayer-perturbing potency (Figure S2). Note that a lower gA_2 concentration indicates more potent bilayer perturbation. Some noticeable structural trends were observed (Table 1). Analogues 11 and 18 that lack aminoethyl side chains did not have a measurable gA_2 because they caused no changes in the quench rate at the highest concentration tested. This result indicates that these analogues have minimal effects on bilayer properties. The linkage between the tryptamine monomers also affected bilayer perturbation. For example, the ether-linked derivatives 14 and 15 had the lowest gA_2 , and replacing the disulfide linkage of 5 with a trimethylene chain as in 16 did not detectably change gA_2 . Other changes to the aminoethyl side chains as shown by 14 vs 15 and 16 vs 17 increased the bilayer-modifying potency.

Bilayer partitioning did not predict the bilayer-perturbing potency, as there was no obvious correlation between K_p^{W-L} and gA_2 (Figure 4B) ($r = -0.27$, $p = 0.47$). Divergent effects of structure on K_p^{W-L} and gA_2 can also be seen when comparing the related analogues 1a vs 14 and 15, as well as 5 vs 16 and 17. For compounds 1a, 14, and 15, a decreasing gA_2 was consistent with an increasing K_p^{W-L} , as would be expected if an increase in the partition coefficient decreased the aqueous concentration needed to reach a mole fraction in the bilayer that caused the perturbation. Substituting an ether linkage into 1a giving 14, for example, increased bilayer partitioning and perturbation. When the aminoethyl groups in 14 are acetylated to give 15, there is a further slight increase of bilayer partitioning and perturbation (Figure 4B, brown arrows). However, in a sequence of modifications at the same positions of the Cl-substituted disulfide in the series 5, 16, and 17, gA_2 appeared insensitive to K_p^{W-L} (5 → 16, Figure 4B, stippled green arrows) and then anticorrelated (16 → 17). A particularly striking example of the divergence between gA_2 and K_p^{W-L} is seen when the bromo group at C6 in 1a is moved to C5 in 8, resulting in a moderate increase in K_p^{W-L} yet complete inactivity in the gA assay (Figure 4A, right panel). Overall, BrMT analogues did not

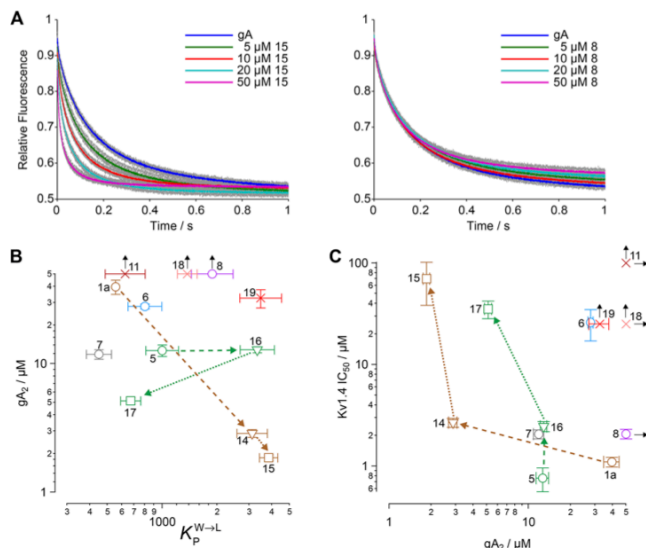


Figure 4. Membrane perturbation is distinct from partitioning and does not predict channel inhibition. (A) Gramicidin A (gA) channel activity, as measured by the rate of quenching of intravesicular ANTS fluorescence by Ti^+ . For each trace, the gray dots denote the results obtained in the nine individual repeats, whereas the colored dots denote the average value at each time point. (B) Membrane partition–perturbation relationships. Numbers next to the different markers denote the analogue’s identity. The shape and color of markers are as in Figure 2. Data from Table 1. Black arrows indicate a null response, with the marker indicating the highest concentration tested. Brown and green arrows with dashed lines indicate modification of the disulfide linker. Brown and green arrows with dotted lines indicate modification of aminoethyl groups. (C) Membrane perturbation–inhibition relationship (data from Table 1).

show a consistent dependence of bilayer perturbation on partitioning.

Potency of Channel Modulation Is Not Dictated by Bilayer Perturbation. Bilayer perturbation was altered by BrMT analogues in a fashion distinct from partitioning, so we then assessed whether perturbation might be the mechanism underlying Kv modulation. When Kv1.4 IC_{50} values are plotted vs gA_2 values as a measure of bilayer perturbation, there is no obvious correlation ($r = -0.37$, $p = 0.36$) (Figure 4C). In fact, more potent bilayer-perturbing compounds are generally weaker inhibitors of Kv1.4. Substitution of the native disulfide linkage of **1a** for the ether linker in **14** led to a 10-fold decrease in gA_2 (10-fold increase in bilayer-perturbing potency) with a slight decrease in potency of channel inhibition ($\text{IC}_{50} = 2.7 \mu\text{M}$ for **14** vs $1.1 \mu\text{M}$ for **1a**). In contrast, when the disulfide linkage in the 6-chloro analogue **5** is replaced with the trimethylene linker in **16**, there is little change in gA_2 , but there is a 3-fold increase in IC_{50} . Changes to the aminoethyl side chain (e.g., **14** → **15** or **16** → **17**) decrease gA_2 but increase IC_{50} (Figure 4C). Notably, analogue **8**, which does not perturb bilayers at the highest concentration tested, is a strong modulator of Kv1.4, whereas the most bilayer-perturbing analogue **15** is a weak modulator of Kv1.4 channels. Inspection of the current traces recorded in the presence of **15** reveals that inactivation is accelerated. This action is consistent with prior findings that bilayer-perturbing detergents modulate inactivation of Kv1 channels⁶¹ and suggests that Kv1.4 modulation by **15** may

occur via a mechanism different from that of the less bilayer-perturbing BrMT analogues.

DISCUSSION

Overall, these relationships show that Kv1.4 inhibition does not correlate with either bilayer partitioning or bilayer perturbation. We conclude that though BrMT and its analogues that are active against ion channels all partition into bilayers and usually perturb bilayer properties, the partitioning and alterations in bilayer properties do not drive potassium channel modulation. We conclude that specific interactions between Kv1.4 and “strong” modulators such as BrMT and BrET are critical for activity.

Limitations. Our results show that bilayer partitioning and perturbation are not critical determinants of modulation of Kv channels by BrMT or its analogues. These conclusions rely on interpretations that have caveats:

1. The bilayer partitioning and perturbation experiments were conducted with bilayers formed by synthetic phosphocholine lipids. Results in multicomponent bilayers,^{62–64} and whole cells,¹⁰ have been found to be similar to those obtained in single-component bilayers. On the basis of these previous validations, we expect the impact of compounds on single-component bilayers will extend to living cells more generally. However, our experiments do not exclude the possibility that BrMT derivatives partition differently into CHO cells and/or interact in a binding pocket with specialized lipids.

2. Our interpretation assumes that the BrMT derivatives alter Ti^+ flux through gA channels by perturbing lipid membranes, not by interacting directly with the gA channel itself. Our experiments cannot completely exclude such direct effects; results with many different structurally diverse amphiphiles show that they have similar effects on right- and left-handed channels, which effectively excludes direct interactions.^{6,8,65} The achirality of the BrMT derivatives here precludes such a validation.

Implications. By using a series of analogues of the snail defensive toxin BrMT, we identified certain molecular features that determine its inhibition of potassium channels as well as its partitioning into and perturbation of membranes. Our findings are consistent with BrMT acting through a drug binding pocket at the lipid bilayer–potassium channel interface.^{31,66,67} The positive charges of other amphiphilic, membrane partitioning compounds are crucial for their inhibition of Kv1 channels,⁶⁸ which is consistent with our observations for BrMT and analogues. Compounds **1a**, **5**, **7**, **8**, **14**, and **16** each strongly inhibit Kv channels, but of these only the native compound BrMT (**1a**) has a minimal impact on membranes. The BrMT analogue **7** is the only strong Kv1.4 inhibitor that shows a relative decrease in bilayer partitioning and is a more potent bilayer perturber. On the other hand, **8** is the only strong Kv1.4 inhibitor that is a less potent bilayer perturber and has a partition coefficient higher than that of BrMT. Thus, all of our strongly Kv1.4 inhibiting analogues either partitioned into or perturbed the bilayer more than BrMT. We speculate that membrane partitioning and perturbation may have played a role in the natural selection of BrMT to be the defensive toxin of the sea snail, possibly because of its minimal negative impacts on snail membranes. We also conclude that bilayer interactions are not correlated with inhibition of Kv1.4.

BrMT Analogues as Research Tools. The determination of what conformations ion channels adopt is an ongoing challenge of molecular physiology. BrMT is a toxin that selectively binds to resting Kv conformations,¹⁹ making BrMT a powerful tool to explore conformational changes of potassium channels. Conformation-selective ligands are of increasing importance for associating functional states of proteins with structurally defined conformations. For example, conformation-selective toxins were the enabling factors for reconstructing TRPV1 ion channels in an open state,^{16,69–71} and co-crystals of ASIC ion channels with peptide toxin gating modifiers led to the identification of structures of new channel conformations.^{72–74} In functional studies, tagged conformation-selective toxins allow imaging of Kv2 channels adopting specific conformations in live cells.^{75,76} BrMT-like compounds similarly can stabilize the resting conformation of Kv1 channel voltage sensors, and they have the potential to be useful tools for studying channel conformations in cells and live tissue. The ether-linked analogue BrET (**14**) identified in this study is comparable in potency to BrMT but lacks the unstable disulfide moiety of the natural product. With the information that modifications to the indole ring and the linker between them are well-tolerated, a path is revealed for generating additional conformation-selective ligands targeting resting conformations of Kv1 ion channel voltage sensors.

■ ASSOCIATED CONTENT

Supporting Information

The Supporting Information is available free of charge on the ACS Publications website at DOI: 10.1021/acs.biochem.8b00292.

Optimization of bis-indole synthesis (Table S1), representative Kv1.4 current responses to modulators (Figure S1), gramicidin A assay data (Figure S2), and representative normalization of fluorescence in gramicidin A assay (Figure S3). Detailed methods: synthesis of tryptamine building blocks, protocol for bistrryptamine-disulfide formation, protocols for synthesis of BrET (**14**) and **15**, electrophysiology methods, isothermal calorimetry methods, and gramicidin assay methods (PDF)

■ AUTHOR INFORMATION

Corresponding Authors

*E-mail: christopher.dockendorff@mu.edu. Tel.: +1 4142881617.

*E-mail: sparre@med.cornell.edu. Tel.: +1 2127466350.

*E-mail: jsack@ucdavis.edu. Tel.: +1 5307524131.

ORCID

Chris Dockendorff: 0000-0002-4092-5636

Helgi I. Ingólfsson: 0000-0002-7613-9143

Stephen F. Martin: 0000-0002-4639-0695

Jon T. Sack: 0000-0002-6975-982X

Author Contributions

Chemical synthesis: C.D., M.W.D., and D.M.G. Electrophysiology: K.S.E., L.H.K., and J.T.S. Bilayer assays: O.S.A., H.L.L., R.K., T.P., and R.R. Conception of project: R.W.A., O.S.A., C.D., S.F.M., and J.T.S. Writing: O.S.A., C.D., L.H.K., J.T.S., and S.F.M.

Funding

This work was financially supported by Marquette University, the Texas Institute for Drug and Diagnostics Development (TI-3D), and the University of California, Davis. Support for our research programs was also provided by NIH grants R15 HL127636 (C.D.), T32 GM099608 (L.H.K.), R01 NS096317 (J.T.S.), and R01 GM021432 (O.S.A.).

Notes

The authors declare no competing financial interest.

[†]Deceased June 22, 2014.

An earlier version of this manuscript was submitted to the ChemRxiv preprint server: <https://doi.org/10.26434/chemrxiv.5908276.v1>.

■ ACKNOWLEDGMENTS

We thank the staff of the UT-Austin NMR and Mass Spectrometry facilities; Dr. Sheng Cai (Marquette University), for analytical chemistry support; Drs. Ali Yehia and Juliette Johnson (Fluxion) as well as Jeffrey Webber (Molecular Devices) for generous access to and technical assistance with the IonFlux automated patch clamp; Justin Du Bois and Justin Litchfield (Stanford University) for help conceiving the project, preliminary synthesis attempts, and electrophysiology; ACD Laboratories for NMR processing software; and ChemAxon Ltd. for software to calculate ClogP.

■ ABBREVIATIONS

ACN, acetonitrile; ANTS, 8-aminonaphthalene-1,3,6-trisulfonate (disodium salt); ASIC, acid-sensing ion channel; 4-AP, 4-aminopyridine; BrET, BrMT analogue 2-[2-({3-(2-aminoethyl)-6-bromo-1H-indol-2-yl}methoxy)methyl]-6-bromo-1H-indol-3-yl]ethan-1-amine; BrMT, snail toxin 6-bromo-2-mercaptotryptamine dimer; ClogP, calculated log of the partition coefficient ($[n\text{-octanol}]/[\text{water}]$); gA, gramicidin A; g_{A_2} , concentration of compound that elicits a doubling of the rate of gA-dependent quenching; H_p^{W-L} , enthalpy of partitioning from water into lipid; IC_{50} , half-maximal inhibitory concentration; ITC, isothermal calorimetry; K_p^{W-L} , equilibrium constant for partitioning from water into lipid; Kv, voltage-gated potassium channels; LUVs, large unilamellar vesicles; SARs, structure-activity relationship; TRPV1, transient receptor potential vanilloid 1 channel

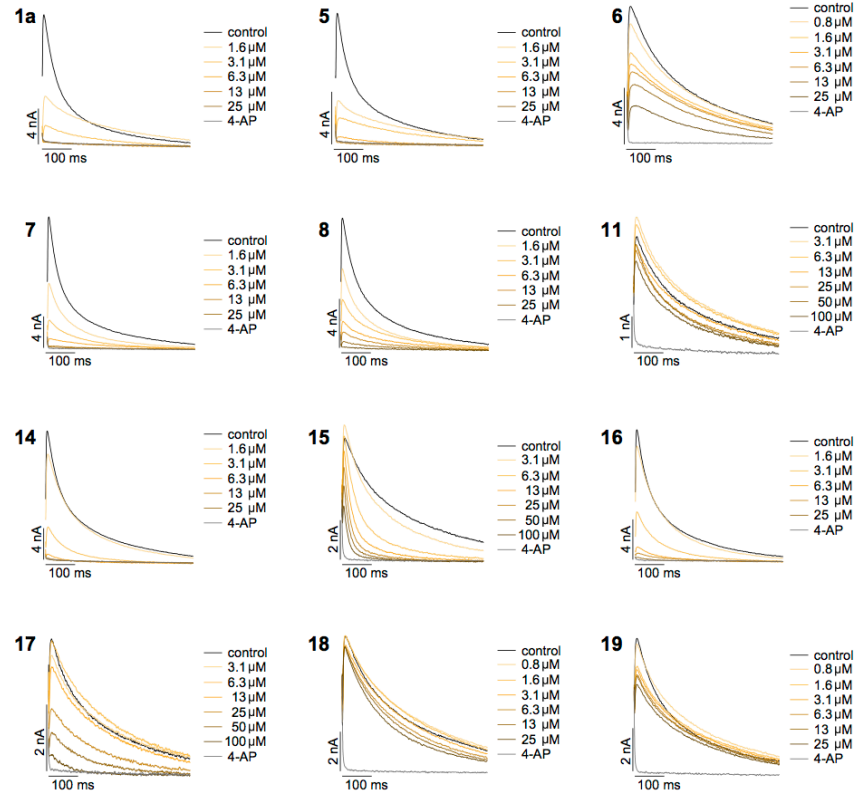
■ REFERENCES

- (1) Spector, A. A., and Yorek, M. A. (1985) Membrane lipid composition and cellular function. *J. Lipid Res.* 26 (9), 1015–1035.
- (2) Bienvenue, A., and Marie, J. S. (1994) Chapter 12 - Modulation of Protein Function by Lipids. In *Current Topics in Membranes* (Hoekstra, D., Ed.) pp 319–354, Academic Press, Inc., San Diego, CA.
- (3) Andersen, O. S., and Koeppe, R. E., 2nd (2007) Bilayer thickness and membrane protein function: an energetic perspective. *Annu. Rev. Biophys. Biomol. Struct.* 36, 107–130.
- (4) Altenbach, R. J., Adair, R. M., Bettencourt, B. M., Black, L. A., Fix-Stenzel, S. R., Gopalakrishnan, S. M., Hsieh, G. C., Liu, H. Q., Marsh, K. C., McPherson, M. J., Milicic, I., Miller, T. R., Vortherms, T. A., Warrior, U., Wetter, J. M., Wishart, N., Witte, D. G., Honore, P., Esbensen, T. A., Hancock, A. A., Brioni, J. D., and Cowart, M. D. (2008) Structure-Activity Studies on a Series of 2-Aminopyrimidine-Containing Histamine H-4 Receptor Ligands. *J. Med. Chem.* 51, 6571–6580.
- (5) Lundbaek, J. A., Birn, P., Tape, S. E., Toombes, G. E., Sogaard, R., Koeppe, R. E., 2nd, Gruner, S. M., Hansen, A. J., and Andersen, O. S. (2005) Capsaicin regulates voltage-dependent sodium channels by altering lipid bilayer elasticity. *Mol. Pharmacol.* 68, 680–689.
- (6) Rusinova, R., Herold, K. F., Sanford, R. L., Greathouse, D. V., Hemmings, H. C., Jr., and Andersen, O. S. (2011) Thiazolidinedione insulin sensitizers alter lipid bilayer properties and voltage-dependent sodium channel function: implications for drug discovery. *J. Gen. Physiol.* 138, 249–270.
- (7) Ingolfsson, H. I., Thakur, P., Herold, K. F., Hobart, E. A., Ramsey, N. B., Periole, X., de Jong, D. H., Zwama, M., Yilmaz, D., Hall, K., Maretzky, T., Hemmings, H. C., Jr., Blobel, C., Marrink, S. J., Kocer, A., Sack, J. T., and Andersen, O. S. (2014) Phytochemicals perturb membranes and promiscuously alter protein function. *ACS Chem. Biol.* 9, 1788–1798.
- (8) Lundbaek, J. A., Koeppe, R. E., 2nd, and Andersen, O. S. (2010) Amphiphile regulation of ion channel function by changes in the bilayer spring constant. *Proc. Natl. Acad. Sci. U. S. A.* 107, 15427–15430.
- (9) Lundbaek, J. A., Birn, P., Girshman, J., Hansen, A. J., and Andersen, O. S. (1996) Membrane stiffness and channel function. *Biochemistry* 35, 3825–3830.
- (10) Lundbaek, J. A., Birn, P., Hansen, A. J., Sogaard, R., Nielsen, C., Girshman, J., Bruno, M. J., Tape, S. E., Egebjerg, J., Greathouse, D. V., Mattice, G. L., Koeppe, R. E., 2nd, and Andersen, O. S. (2004) Regulation of sodium channel function by bilayer elasticity: the importance of hydrophobic coupling. Effects of Micelle-forming amphiphiles and cholesterol. *J. Gen. Physiol.* 123, 599–621.
- (11) Sogaard, R., Werge, T. M., Bertelsen, C., Lundbye, C., Madsen, K. L., and Nielsen, C. H. (2006) GABA(A) receptor function is regulated by lipid bilayer elasticity. *Biochemistry* 45, 13118–13129.
- (12) Huang, C. J., Harootyan, A., Maher, M. P., Qian, C., Raj, C. D., McCormack, K., Numann, R., Negulescu, P. A., and Gonzalez, J. E. (2006) Characterization of voltage-gated sodium-channel blockers by electrical stimulation and fluorescence detection of membrane potential. *Nat. Biotechnol.* 24, 439–446.
- (13) Morris, C. E., and Juranka, P. F. (2007) Nav channel mechanosensitivity: activation and inactivation accelerate reversibly with stretch. *Biophys. J.* 93, 822–833.
- (14) Howery, A. E., Elvington, S., Abraham, S. J., Choi, K. H., Dworschak-Simpson, S., Phillips, S., Ryan, C. M., Sanford, R. L., Almqvist, J., Tran, K., Chew, T. A., Zachariae, U., Andersen, O. S., Whitelegge, J., Matulef, K., Du Bois, J., and Maduke, M. C. (2012) A designed inhibitor of a CLC antiporter blocks function through a unique binding mode. *Chem. Biol.* 19, 1460–1470.
- (15) Lundbaek, J. A., Collingwood, S. A., Ingolfsson, H. I., Kapoor, R., and Andersen, O. S. (2010) Lipid bilayer regulation of membrane protein function: gramicidin channels as molecular force probes. *J. R. Soc., Interface* 7, 373–395.
- (16) Cao, E., Liao, M., Cheng, Y., and Julius, D. (2013) TRPV1 structures in distinct conformations reveal activation mechanisms. *Nature* 504, 113–118.
- (17) Walpole, C. S., Bevan, S., Bovermann, G., Boelsterli, J. J., Breckenridge, R., Davies, J. W., Hughes, G. A., James, I., Oberer, L., Winter, J., and Wrigglesworth, R. (1994) The discovery of capsazepine, the first competitive antagonist of the sensory neuron excitants capsaicin and resiniferatoxin. *J. Med. Chem.* 37, 1942–1954.
- (18) Kelley, W. P., Wolters, A. M., Sack, J. T., Jockusch, R. A., Jurchen, J. C., Williams, E. R., Sweedler, J. V., and Gilly, W. F. (2003) Characterization of a novel gastropod toxin (6-bromo-2-mercaptotryptamine) that inhibits shaker K channel activity. *J. Biol. Chem.* 278, 34934–34942.
- (19) Sack, J. T., Aldrich, R. W., and Gilly, W. F. (2004) A gastropod toxin selectively slows early transitions in the Shaker K channel's activation pathway. *J. Gen. Physiol.* 123, 685–696.
- (20) Sack, J. T., and Aldrich, R. W. (2006) Binding of a gating modifier toxin induces intersubunit cooperativity early in the Shaker K channel's activation pathway. *J. Gen. Physiol.* 128, 119–132.
- (21) Wulff, H., Castle, N. A., and Pardo, L. A. (2009) Voltage-gated potassium channels as therapeutic targets. *Nat. Rev. Drug Discovery* 8, 982–1001.
- (22) Bagal, S. K., Brown, A. D., Cox, P. J., Omoto, K., Owen, R. M., Pryde, D. C., Sidders, B., Skerratt, S. E., Stevens, E. B., Storer, R. I., and Swain, N. A. (2013) Ion channels as therapeutic targets: a drug discovery perspective. *J. Med. Chem.* 56, 593–624.
- (23) Sack, J. T. (2003) Voltage gating of the Shaker potassium channel is modified by 6-bromo-2-mercaptotryptamine, a novel gastropod toxin. Ph.D. Thesis. Stanford University, Palo Alto, CA.
- (24) Gingrich, K. J., Burkat, P. M., and Roberts, W. A. (2009) Pentobarbital produces activation and block of $\{\alpha\}_1\{\beta\}_2\{\gamma\}_2$ 2S GABAA receptors in rapidly perfused whole cells and membrane patches: divergent results can be explained by pharmacokinetics. *J. Gen. Physiol.* 133, 171–188.
- (25) Sheetz, M. P., and Singer, S. J. (1976) Equilibrium and kinetic effects of drugs on the shapes of human erythrocytes. *J. Cell Biol.* 70, 247–251.
- (26) Sheetz, M. P., and Singer, S. J. (1974) Biological membranes as bilayer couples. A molecular mechanism of drug-erythrocyte interactions. *Proc. Natl. Acad. Sci. U. S. A.* 71, 4457–4461.
- (27) Martinac, B., Adler, J., and Kung, C. (1990) Mechanosensitive ion channels of *E. coli* activated by amphipaths. *Nature* 348, 261–263.
- (28) Browning, J. L., and Nelson, D. L. (1976) Amphipathic amines affect membrane excitability in paramoecium: role for bilayer couple. *Proc. Natl. Acad. Sci. U. S. A.* 73, 452–456.
- (29) Lee, S. Y., and MacKinnon, R. (2004) A membrane-access mechanism of ion channel inhibition by voltage sensor toxins from spider venom. *Nature* 430, 232–235.
- (30) Milescu, M., Vobecky, J., Roh, S. H., Kim, S. H., Jung, H. J., Kim, J. I., and Swartz, K. J. (2007) Tarantula toxins interact with voltage sensors within lipid membranes. *J. Gen. Physiol.* 130, 497–511.
- (31) Gupta, K., Zamanian, M., Bae, C., Milescu, M., Krepiy, D., Tilley, D. C., Sack, J. T., Yarov-Yarovoy, V., Kim, J. I., and Swartz, K. J.

- (2015) Tarantula toxins use common surfaces for interacting with Kv and ASIC ion channels. *eLife* 4, e06774.
- (32) Suchyna, T. M., Tape, S. E., Koeppel, R. E., 2nd, Andersen, O. S., Sachs, F., and Gottlieb, P. A. (2004) Bilayer-dependent inhibition of mechanosensitive channels by neuroactive peptide enantiomers. *Nature* 430, 235–240.
- (33) Andersen, O. S. (2008) Perspectives on how to drug an ion channel. *J. Gen. Physiol.* 131, 395–397.
- (34) Gao, D., Sand, R., Fu, H., Sharmin, N., Gallin, W. J., and Hall, D. G. (2013) Synthesis of the non-peptidic snail toxin 6-bromo-2-mercaptotryptamine dimer (BrMT)(2), its lower and higher thio homologs and their ability to modulate potassium ion channels. *Bioorg. Med. Chem. Lett.* 23, 5503–5506.
- (35) Schumacher, R. W., and Davidson, B. S. (1999) Synthesis of didemnoles A-D, N9-substituted beta-carboline alkaloids from the marine ascidian Didemnum sp. *Tetrahedron* 55, 935–942.
- (36) Wieland, T., Weiberg, O., Fischer, E., and Horlein, G. (1954) *Darstellung Schwefel-Haltiger Indol-Derivate. *Liebigs Ann. Chem.* 587, 146–161.
- (37) Freter, K., Weissbach, H., Redfield, B., Udenfriend, S., and Witkop, B. (1958) Oxindole Analogs of (5-Hydroxy)-Tryptamine and (5-Hydroxy)-Tryptophan, as Inhibitors of the Biosynthesis and Breakdown of Serotonin. *J. Am. Chem. Soc.* 80, 983–987.
- (38) Showalter, H. D. H., Sercel, A. D., Leja, B. M., Wolfangel, C. D., Ambrosio, L. A., Elliott, W. L., Fry, D. W., Kraker, A. J., Howard, C. T., Lu, G. H., Moore, C. W., Nelson, J. M., Roberts, B. J., Vincent, P. W., Denny, W. A., and Thompson, A. M. (1997) Tyrosine kinase inhibitors 0.6. Structure-activity relationships among N- and 3-substituted 2,2'-diselenobis(1H-indoles) for inhibition of protein tyrosine kinases and comparative in vitro and in vivo studies against selected sulfur congeners. *J. Med. Chem.* 40, 413–426.
- (39) Nagy, P. (2013) Kinetics and mechanisms of thiol-disulfide exchange covering direct substitution and thiol oxidation-mediated pathways. *Antioxid. Redox Signaling* 18, 1623–1641.
- (40) Dann, O., Wolff, H. P., Schlee, R., and Ruff, J. (1986) Syntheses of Antileukemic (Indolylvinyl)Indoles. *Liebigs Annalen Der Chemie* 1986, 2164–2178.
- (41) Sercel, A. D., and Showalter, H. D. (2006) The synthesis of symmetrical (2-indolyl)ethynes and reduced congeners via palladium-catalyzed couplings of 2-bromoindole precursors. *J. Heterocycl. Chem.* 43, 701–707.
- (42) Altenbach, R., Black, L., Chang, S. J., Cowart, M., Faghii, R., Gfesser, G., Ku, Y. Y., Liu, H., Lukin, K., and Nersesian, D. (2004) Bicyclic-substituted amines as histamine-3 receptor ligands, WO 2004/043458.
- (43) Baran, P. S., and Shenvi, R. A. (2006) Total synthesis of (±)-chartelline C. *J. Am. Chem. Soc.* 128, 14028–14029.
- (44) Yoon, N. M., and Brown, H. C. (1968) Selective Reductions. 12. Explorations in Some Representative Applications of Aluminum Hydride for Selective Reductions. *J. Am. Chem. Soc.* 90, 2927–2938.
- (45) Du, X., and Gamper, N. (2013) Potassium channels in peripheral pain pathways: expression, function and therapeutic potential. *Current neuropharmacology* 11, 621–640.
- (46) Rasband, M. N., Park, E. W., Vanderah, T. W., Lai, J., Porreca, F., and Trimmer, J. S. (2001) Distinct potassium channels on pain-sensing neurons. *Proc. Natl. Acad. Sci. U. S. A.* 98, 13373–13378.
- (47) Wells, J. E., Rose, E. T., Rowland, K. C., and Hatton, J. F. (2007) Kv1.4 subunit expression is decreased in neurons of painful human pulp. *J. Endod.* 33, 827–829.
- (48) Gutman, G. A., Chand, K. G., Grissmer, S., Lazdunski, M., McKinnon, D., Pardo, L. A., Robertson, G. A., Rudy, B., Sanguinetti, M. C., Stuhmer, W., and Wang, X. (2005) International Union of Pharmacology. LIII. Nomenclature and molecular relationships of voltage-gated potassium channels. *Pharmacol. Rev.* 57, 473–508.
- (49) Manganas, L. N., and Trimmer, J. S. (2000) Subunit composition determines Kv1 potassium channel surface expression. *J. Biol. Chem.* 275, 29685–29693.
- (50) Manganas, L. N., Wang, Q., Scannevin, R. H., Antonucci, D. E., Rhodes, K. J., and Trimmer, J. S. (2001) Identification of a trafficking determinant localized to the Kv1 potassium channel pore. *Proc. Natl. Acad. Sci. U. S. A.* 98, 14055–14059.
- (51) Guo, L., and Guthrie, H. (2005) Automated electrophysiology in the preclinical evaluation of drugs for potential QT prolongation. *J. Pharmacol. Toxicol. Methods* 52, 123–135.
- (52) Sorota, S., Zhang, X. S., Margulis, M., Tucker, K., and Priestley, T. (2005) Characterization of a hERG screen using the IonWorks HT: comparison to a hERG rubidium efflux screen. *Assay Drug Dev. Technol.* 3, 47–57.
- (53) Rasmussen, R. L., Morales, M. J., Wang, S., Liu, S., Campbell, D. L., Brahmajothi, M. V., and Strauss, H. C. (1998) Inactivation of voltage-gated cardiac K⁺ channels. *Circ. Res.* 82, 739–750.
- (54) Litchfield, J. D. (2010) Using synthetic small molecules to probe the structure and function of voltage-gated ion channels. Ph.D. Thesis, Stanford University, Palo Alto, CA.
- (55) Heerklotz, H., and Seelig, J. (2000) Titration calorimetry of surfactant-membrane partitioning and membrane solubilization. *Biochim. Biophys. Acta, Biomembr.* 1508, 69–85.
- (56) Ingólfsson, H. I., and Andersen, O. S. (2010) Screening for small molecules' bilayer-modifying potential using a gramicidin-based fluorescence assay. *Assay Drug Dev. Technol.* 8, 427–436.
- (57) Ingólfsson, H. I., Sanford, R. L., Kapoor, R., and Andersen, O. S. (2010) Gramicidin-based fluorescence assay; for determining small molecules potential for modifying lipid bilayer properties. *J. Visualized Exp.* 44, e2131.
- (58) Moore, H. P., and Raftery, M. A. (1980) Direct spectroscopic studies of cation translocation by *Torpedo* acetylcholine receptor on a time scale of physiological relevance. *Proc. Natl. Acad. Sci. U. S. A.* 77, 4509–4513.
- (59) Ingólfsson, H. I., and Andersen, O. S. (2010) Screening for small molecules' bilayer-modifying potential using a gramicidin-based fluorescence assay. *Assay Drug Dev. Technol.* 8, 427–436.
- (60) Ingólfsson, H. I., Sanford, R. L., Kapoor, R., and Andersen, O. S. (2010) Gramicidin-based fluorescence assay for determining small molecules potential for modifying lipid bilayer properties. *J. Visualized Exp.*, e2131.
- (61) Hollerer-Beitz, G., and Heinemann, S. H. (1998) Influence of detergents on the function of cloned potassium channels. *Receptors Channels* 5 (2), 61–78.
- (62) Bruno, M. J., Koeppel, R. E., 2nd, and Andersen, O. S. (2007) Docosahexaenoic acid alters bilayer elastic properties. *Proc. Natl. Acad. Sci. U. S. A.* 104, 9638–9643.
- (63) Rusinova, R., Koeppel, R. E., 2nd, and Andersen, O. S. (2015) A general mechanism for drug promiscuity: Studies with amiodarone and other antiarrhythmics. *J. Gen. Physiol.* 146, 463–475.
- (64) Herold, K. F., Sanford, R. L., Lee, W., Andersen, O. S., and Hemmings, H. C., Jr. (2017) Clinical concentrations of chemically diverse general anesthetics minimally affect lipid bilayer properties. *Proc. Natl. Acad. Sci. U. S. A.* 114, 3109–3114.
- (65) Hwang, T. C., Koeppel, R. E., 2nd, and Andersen, O. S. (2003) Genistein can modulate channel function by a phosphorylation-independent mechanism: importance of hydrophobic mismatch and bilayer mechanics. *Biochemistry* 42, 13646–13658.
- (66) Ottosson, N. E., Silvera Ejneby, M., Wu, X., Yazdi, S., Konradsson, P., Lindahl, E., and Elinder, F. (2017) A drug pocket at the lipid bilayer-potassium channel interface. *Sci. Adv.* 3, e1701099.
- (67) Milescu, M., Bosmans, F., Lee, S., Alabi, A. A., Kim, J. I., and Swartz, K. J. (2009) Interactions between lipids and voltage sensor paddles detected with tarantula toxins. *Nat. Struct. Mol. Biol.* 16, 1080–1085.
- (68) Borjesson, S. L., Parkkari, T., Hammarstrom, S., and Elinder, F. (2010) Electrostatic tuning of cellular excitability. *Biophys. J.* 98, 396–403.
- (69) Bae, C., Anselmi, C., Kalia, J., Jara-Oseguera, A., Schwieters, C. D., Krepiy, D., Won Lee, C., Kim, E. H., Kim, J. I., Faraldo-Gomez, J. D., and Swartz, K. J. (2016) Structural insights into the mechanism of activation of the TRPV1 channel by a membrane-bound tarantula toxin. *eLife* 5, 1.

- (70) Gao, Y., Cao, E., Julius, D., and Cheng, Y. (2016) TRPV1 structures in nanodiscs reveal mechanisms of ligand and lipid action. *Nature* 534, 347–351.
- (71) Liao, M., Cao, E., Julius, D., and Cheng, Y. (2013) Structure of the TRPV1 ion channel determined by electron cryo-microscopy. *Nature* 504, 107–112.
- (72) Bacongus, I., and Gouaux, E. (2012) Structural plasticity and dynamic selectivity of acid-sensing ion channel-spider toxin complexes. *Nature* 489, 400–405.
- (73) Dawson, R. J., Benz, J., Stohler, P., Tetaz, T., Joseph, C., Huber, S., Schmid, G., Hugin, D., Pflimlin, P., Trube, G., Rudolph, M. G., Hennig, M., and Ruff, A. (2012) Structure of the acid-sensing ion channel 1 in complex with the gating modifier Psalmotoxin 1. *Nat. Commun.* 3, 936.
- (74) Bacongus, I., Bohlen, C. J., Goehring, A., Julius, D., and Gouaux, E. (2014) X-ray structure of acid-sensing ion channel 1-snake toxin complex reveals open state of a Na(+)-selective channel. *Cell* 156, 717–729.
- (75) Tilley, D. C., Eum, K. S., Fletcher-Taylor, S., Austin, D. C., Dupre, C., Patron, L. A., Garcia, R. L., Lam, K., Yarov-Yarovoy, V., Cohen, B. E., and Sack, J. T. (2014) Chemoselective tarantula toxins report voltage activation of wild-type ion channels in live cells. *Proc. Natl. Acad. Sci. U. S. A.* 111, E4789–4796.
- (76) Cobb, M. M., Austin, D. C., Sack, J. T., and Trimmer, J. S. (2015) Cell Cycle-dependent Changes in Localization and Phosphorylation of the Plasma Membrane Kv2.1 K⁺ Channel Impact Endoplasmic Reticulum Membrane Contact Sites in COS-1 Cells. *J. Biol. Chem.* 290, 29189–29201.

Figure S1. Representative Kv1.4 current responses to modulators



Current measured during voltage steps from -100 mV to 0 mV. Compound tested is indicated by number to left of each panel. Concentration tested is indicated in legend. 4-AP indicates currents remaining during application of 10 mM 4-aminopyridine.

6. Electrophysiology methods

Cell culture

A tetracycline-inducible Kv1.4 cell line was established in CHO-K1 cells stably expressing a tetracycline repressor (T-REx-CHO, ThermoFisher), and a Kv β 2 subunit to increase surface expression. The T-REx-CHO cells were maintained in tissue-culture treated polystyrene dishes 37°C in a 5% CO₂ atmosphere in Ham's F12 media containing 10% FBS (Hyclone Fetal Bovine Serum Characterized (cat. SH30071.03, lot AXM55317), 1% penicillin/streptomycin (Life Technologies 15140-122), and 10 μ g/mL blasticidin. Cells were transfected with a Kv β 2/RBG4 REF and GFP (EGFP-C1, Clontech) using Lipofectamine 2000 (ThermoFisher). GFP fluorescence was used to confirm transfection and the vector confers G418 resistance. Two days after transfection, 500 μ g/mL G418 was added to media. After emergence of G418-resistant cell colonies, cells were subcloned by dilution into 96-well plates. Wells containing single clones were expanded and screened for Kv β 2 expression by immunoblotting with an anti-Kv β 2 monoclonal antibody (UC Davis/NIH NeuroMab Facility Cat# 73-021, RRID:AB_10673520). The CHO-K1/T-REx/ Kv β 2 H7 clonal cell line was expanded for further use. Rat Kv1.4 cDNA was excised with EcoRI from a pRC/CMV expression construct (12), and ligated into a Zeocin-resistance expression vector containing tetracycline operator sequences (pcDNA4/TO, ThermoFisher) at its EcoRI site. The Kv1.4/pcDNA4/TO vector and a dsRed vector (pDsRed-monomer-C1, Clontech) were transfected using Lipofectamine 2000. dsRED fluorescence was used to confirm transfection. One day after transfection 250 μ g/mL zeocin was added to media. After emergence of zeocin-resistant cell colonies, cells were subcloned by dilution into 96-well plates. Wells containing single clones were expanded, incubated overnight with 1 μ g/mL tetracycline and screened for large inactivating K⁺ currents by manual patch clamp electrophysiology. Cell line clone E8, which also had dsRed fluorescence was selected for electrophysiology assays, and maintained with 1 μ g/ml blasticidin, 25 μ g/ml zeocin to retain Kv1.4 and the tetracycline repressor. Frozen aliquots of 5-10 million cells were prepared for electrophysiology. Cells were expanded for freezing in 175 cm² flasks in media without selection agents. 4-8 hours before freezing, 1 μ g/ml tetracycline was added to media to induce a desirable amount of channel expression. Cells were washed with divalent-free Dulbecco's Phosphate Buffered Saline (Gibco 14190144), dissociated with Detachin (Gentamicin), centrifuged at 500g for 2 minutes then resuspended to 5-10 million cells/mL in Recovery media (Gibco 12648010), frozen in cryogenic tubes in an insulated container (CoolCell, Biocision) at -80°C overnight, and stored in liquid N₂ until the day of use.

Electrophysiology

To measure currents from Kv1.4 channels, ensemble voltage-clamp recordings were performed on an automated IonFlux system (Fluxion Biosciences). Cells were thawed and resuspended in CHO-SFMII media (Life Technologies 12052-114) supplemented with 25 mM HEPES (pH 7.3), and shaken at 300 rpm in a 25 cm² polypropylene flask at room temperature for 30 minutes prior to use. Cells were centrifuged at 200 g for 3 minutes, then resuspended in extracellular solution (below) to a concentration of 5x10⁶ cells/mL and pipetted along with test compounds and intracellular solution into 384 well IonFluxHT plates immediately before recording, according to manufacturer's protocols. The extracellular solution contained (in mM): 50 HEPES, 20 KOH, 150 NaCl, 2 CaCl₂, 2 MgCl₂, 0.1 Mg-EDTA, adjusted to pH 7.3 with HCl. The intracellular solution contained (in mM): 50 KF, 70 KCl, 35 KOH, 5 EGTA, 50 HEPES, 2 TCEP adjusted to pH 7.3 with HCl. Temperature was approximately 20°C. The IonFluxHT plates contain 96 cell 'traps': electrically isolated wells with 20 holes to capture cells and establish patch clamp seals with individual cells. These allow ensemble voltage clamp recordings from up to 20 cells per trap. Trap pressure was held at 6 mmHg during cell positioning and data acquisition with a step to 12 mmHg for 15 s during break-in. Initial resistance of each well trap with these solutions was 0.5-0.7 M Ω . Currents were recorded at a sampling rate of 5 kHz. Holding potential was -120 mV. To activate Kv1.4, 1 s test pulses to 0 mV were repeated every 10 s.

Test compounds were dissolved in acetonitrile (ACN)/water solutions to 10 mM. Compound stocks were diluted serially to test concentrations in extracellular solution including 1% (v/v) FL reagent (Fluxion) and 5 μ M tetrodotoxin (Abcam Biochemicals ab120054). Vehicle controls included 1% FL reagent, 5 μ M tetrodotoxin, and acetonitrile for each compound replicate. Compounds were perfused in series from low to high concentration. All experiments were concluded with 10 mM 4-aminopyridine (Sigma A0152) in vehicle to inhibit all Kv1.4 current.

The range of analog concentrations that were tested in voltage clamp assays were limited by experimental considerations. At high concentrations, solvent concentrations posed a concern, and BrMT destabilizes the patch clamp seal at concentrations >20 μ M.^(13, 14) Concentrations of BrMT <1 μ M resulted in very slow onset of channel inhibition, which required long equilibration times (>1000 s), that were incompatible with the solution reservoirs of the IonFlux system. While another voltage clamp method (e.g. manual patch clamp or *Xenopus* oocyte voltage clamp) might enable extension of the concentration range tested, the hydrophobicity of BrMT leads to different effective concentrations in different cell preparations,^(13, 14) and we limited the concentration range tested rather than attempt to merge datasets from different preparations. As noted in the main text, this experimental system dependence is consistent with BrMT's interacting with membranes.

Electrophysiology data analysis

Linear leak currents were subtracted using the IonFlux data analysis software (Fluxion) from a 10 ms voltage step from the holding potential to -110 mV preceding 40 ms at the holding potential and the depolarizing step to 0 mV. Inactivating current was measured as the difference from the peak (6 to 25 ms) and final (990-1000 ms) current during a 1000 ms voltage step from -120 mV to 0 mV. Currents were exported from time points 15 s before each solution change and 85 s after 4-AP addition. Leak-subtracted currents were zeroed to values after 4-AP addition and normalized to maximum current. Records that did not exhibit current with Kv1.4-like activation and deactivation kinetics prior to the addition of the lowest concentration of test compound were excluded from the analysis. Records that exhibited substantial run-up, or inconsistent resistance at holding potential were also excluded. A time-dependent run-down in current was observed in nearly all vehicle control experiments. To correct for this run down, values were divided by the normalized time-matched mean current from vehicle controls.

Graphing and analysis of electrophysiology were performed in IgorPro 7 (Wavemetrics). Concentration response and kinetics curves were fit by non-linear least-squares methods employing the Levenberg-Marquardt algorithm in IgorPro. After transformation to fraction of maximal current, the concentration-response of each compound was fit with a Hill equation:

$$F_{inhib} = \frac{1}{\left\{1 + \left(\frac{IC50}{[compound]}\right)^h\right\}} \quad (1)$$

where F_{inhib} is the fraction of maximal current inhibited during a 0 mV voltage step, $IC50$ is the current at which 50% of current is inhibited, $[compound]$ is the concentration of test compound, and h is the Hill slope.

Time constants of activation and inactivation were determined by fitting a double exponential equation:

$$I_K = I_0 + A_1 \exp\left\{\frac{-(t-t_0)}{\tau_1}\right\} + A_2 \exp\left\{\frac{-(t-t_0)}{\tau_2}\right\} \quad (2)$$

to Kv1.4 currents after a step to 0 mV.

CHAPTER 2

Molecular Determinants of μ -Conotoxin KIIIA interaction with the Voltage-Gated Sodium Channel Nav1.7

This chapter details my research into the structural underpinnings of the binding and inhibition of voltage-gated sodium channels by a peptide toxin from marine snails.

This work has been submitted for publication and is in revision

Kimball, IH*, Nguyen PT*, Olivera, BM, Sack, JT, Yarov-Yarovoy, V

* - these authors contributed equally to this work

I conducted electrophysiology experiments, analyzed data, and wrote for the following sections:

Functional mapping of KIIIA residues at toxin – channel interface

Figure 6. Functional mapping of KIIIA and hNav1.7 residues at toxin – channel interface.

Functional mapping of hNav1.7 residues at toxin – channel interface

Figure 6. Functional mapping of KIIIA and hNav1.7 residues at toxin – channel interface.

Double Mutant Cycle Analysis of Key pairwise interactions between KIIIA and hNav1.7

Figure 7. Double Mutant Cycle Analysis of key pairwise interactions between KIIIA and hNav1.7.

Abstract

The voltage-gated sodium (Nav) channel subtype Nav1.7 plays a critical role in pain signaling, making it an important drug target. A number of peptide toxins from cone snails (conotoxins) bind to the extracellular vestibule of the Nav channel pore and block ion conduction. While the known conotoxins have variable selectivity among Nav channel subtypes, they form potential scaffolds for engineering of selective and potent channel inhibitors. Here we studied the molecular interactions between μ -conotoxin KIIIA (KIIIA) and the human Nav1.7 channel (hNav1.7). Using the cryo-electron microscopy (cryo-EM) structure of the electric eel Nav1.4 channel as a template we developed a structural model of hNav1.7 with Rosetta computational modeling. We performed *in silico* docking of KIIIA using RosettaDock and identified residues forming specific pairwise contacts between KIIIA and hNav1.7. Pairwise interactions were experimentally validated using mutant cycle analysis. Comparison with a recently published cryo-EM structure of the KIIIA-hNav1.2 channel complex revealed key similarities and differences between channel subtypes with potential implications for the molecular mechanism of toxin block. Our integrative approach, combining high-resolution structural data with computational modeling and experimental validation, will be useful for engineering of molecular probes to study Nav channels function and for rational design of novel biologics to treat chronic pain, cardiac arrhythmias, and epilepsy.

Introduction

Voltage-gated sodium (Nav) channels play a key role in the action potential generation in excitable cells (1, 2). The nine subtypes of Nav channel α -subunits (named 1.1-1.9) are differentially expressed throughout tissues, and are studied as potential targets for development of therapeutics for chronic pain, cardiac arrhythmias, and epilepsy (3). Human Nav1.7 (hNav1.7) is known to be important for pain signaling and its mutations have been linked to severe pain disorders ranging from complete lack of pain sensation to extreme sensitivity to pain (4-6). Clinical use of local anesthetic drugs is limited because they bind to highly conserved receptor site within the Nav channel pore lumen (7-10).

Nav channels are common targets of small disulfide-knotted peptide toxins from cone snails (conotoxins) (2), which target the extracellular vestibule of the Nav channel pore and offer useful peptide scaffolds for rational design of novel peptide-based therapeutics to treat pain, arrhythmias, and epilepsy (11, 12). μ -conotoxin KIIIA (KIIIA) is a 16 amino acid peptide that potently inhibits TTX-sensitive Nav channels (2, 13, 14), and has shown analgesic properties in animal models of pain (13) (Figure 5A). KIIIA has variable degrees of affinity and block for the different Nav channel subtypes, with 5 nM affinity for rat Nav1.2, 37 nM for r at Nav1.4, and 97 nM for hNav1.7 (2, 13, 15). Structure-activity relationship studies have identified the KIIIA residues K7, W8, R10, D11, H12 and R14 as key for binding to various Nav channel subtypes (13, 15). Specifically, K7, R10 and R14 have been shown to contribute to binding affinity and block of hNav1.7 (15). Interestingly, the relative contribution of KIIIA residues in binding to Nav channels vary between channel subtypes. For example, substitution R14A in KIIIA reduces the affinity for Nav1.2 and Nav1.4 by two orders of magnitude, while only reducing the affinity for Nav1.7 by a 5-fold (15). Substitution R10A in KIIIA similarly shows reduced effect on affinity for Nav1.7 compared to

Nav1.2 and Nav1.4, while having a more drastic effect on channel block of Nav1.7 (15). In addition, KIIIA blocks Nav channels incompletely and can co-bind with tetrodotoxin (TTX) to TTX-sensitive Nav channels, while other μ -conotoxins such as GIIIA, GIIIB, and PIIIA block Nav channels completely (16).

Previous studies identified the importance of Nav channel residues near the selectivity filter on the P2-helix in domain III (DIII) for their apparent coupling to residues R10 and R14 on KIIIA (15). Notably, the P2-helix in DIII of hNav1.7 has Threonine at position 1398 and an Isoleucine at position 1399, while all other human Nav channels have Methionine and Aspartate at the corresponding positions (15). These residues were proposed to play a role in the selectivity of KIIIA binding to Nav1.2 and Nav1.4 versus to Nav1.7 (15). Molecular modeling of KIIIA binding to rNav1.4 using restraints from experimental data also revealed contacts between KIIIA and the P2-helix in DIII (17). However, these studies have not provided an explanation for the significant effect of the KIIIA mutations H12A, W8A and D11A on toxin affinity. In this study, we used computational and experimental approaches to investigate the molecular mechanism of the KIIIA interaction with hNav1.7. We present a structural model of KIIIA binding to the hNav1.7 channel based on the eukaryotic electric eel Nav1.4 cryo-EM structure. Our model revealed asymmetric binding of KIIIA to hNav1.7 at the interface between the P2-helices in domain II (DII) and DIII, which exposed a partially open ion conduction pathway that may explain the incomplete blocking characteristic of the toxin. We identified several unique contacts between KIIIA and extracellular loops on hNav1.7, providing key structural insights into binding specificity for different Nav channels subtypes. We used mutant cycle analysis to validate representative pairwise contacts between specific KIIIA and hNav1.7 residues identified from our structural model of the KIIIA – hNav1.7 complex. Remarkably, the recently published cryo-EM structure of KIIIA - hNav1.2

complex (18) agrees with findings from our computational modeling and functional study. The high atomic accuracy of peptide toxin – Nav channel interactions modeling with Rosetta in combination with functional testing paves the way for the rational design of novel selective inhibitors targeting Nav channels with high selectivity and potency.

Results

Molecular modeling reveals asymmetric binding of KIIIA to hNav1.7 pore

To characterize the molecular mechanism of the KIIIA interaction with hNav1.7, we utilized computational modeling and functional validation approaches as described below. The cryo-EM structure of the electric eel Nav1.4 (eeNav1.4) (19) channel was the closest structural homolog available to build the homology model of hNav1.7 when this study was conducted. The eeNav1.4 structure shares ~54% sequence identity with hNav1.7 overall and ~75% sequence identity over the hNav1.7 pore region. We used the RosettaCM modeling approach (20, 21) to generate a structural model of hNav1.7 based on the eeNav1.4 structure (19) and Rosetta protein-protein docking approach (21-23) to predict structure of KIIIA – hNav1.7 complex and specific residues forming interactions between KIIIA and hNav1.7 (see Methods). Our model revealed an asymmetrical binding of KIIIA to hNav1.7, where the KIIIA helical region is positioned perpendicular to the P2-helix in DII with the positively charged KIIIA residues facing the selectivity filter (Figure 5B). This orientation is different from KIIIA binding to the P2-helix in DIII previously suggested by computational modeling (15, 17) and lanthanide-based resonance energy transfer (24) studies. Mapping of the open space surrounding the KIIIA - hNav1.7 binding interface revealed a tunnel traversing from the extracellular environment to the channel pore cavity

(Figure 5C). The minimum radius located at the most constricted part of tunnel within the selectivity filter region is of ~ 1 Å. Notably, the upper region of the selectivity filter near the KIIIA binding site has a minimum radius of ~ 2.5 Å, which is large enough to potentially allow sodium ion conduction and consistent with the characteristic incomplete block of Nav channels by KIIIA (13, 15). Notably, KIIIA is positioned just above the selectivity filter which is different from small molecular toxins, such as TTX and STX, which are positioned deeper into the selectivity region (25, 26).

Pairwise interactions identified from the KIIIA - hNav1.7 complex model

We examined contribution of the KIIIA residues to binding energy ($\Delta\Delta G$) in our KIIIA – hNav1.7 complex model (Figure 5D and E). $\Delta\Delta G$ was computed by taking the difference of the Rosetta energies of the KIIIA – hNav1.7 complex and the separated KIIIA and hNav1.7 structures. Our analysis revealed that the KIIIA residues K7, W8, R10, H12, and R14 each have significant contribution to the binding energy (Figure 5D and E). Notably, while K7, W8, R10, and H12 are located on the same face of KIIIA alpha helix, R14 is located within the C-terminal tail region. Our KIIIA – hNav1.7 model predicts that positively charged residue K7 forms a salt bridge with E919 on the P2-helix in DII (Figure 5F). In addition, W8 and H12 were shown to form hydrogen bonds with Y339 on the extracellular loop between S5 and P1-helix (S5P1) in DI and D923 on P2-helix in DII, respectively (Figure 5F). D11 is positioned near the interface between the P2-helices in DII and DIII and forms hydrogen bonds with both K7 on KIIIA and T1398 on the DIII P2 helix (Figure 5F). The other positively charged KIIIA residues, R14 and R10, interact with two negatively charged residues: E1417 on the extracellular loop between the P2-helix and S6 (P2S6) in DIII and D1662 on the extracellular loop S5P1 in DIV. Notably, R14 also interacts with Y1416 on the extracellular P2S6 loop in DIII and contributes to a cation-pi interaction tower formed by

Y1402 on the P2-helix in DIII, R896 on the extracellular loop S5P1 in DII, and Y1416. This position of R14 is different from the previously proposed proximity between R14 and D1241 on the P2-helix in DIII of rNav1.4 (15). However, the R10 position in proximity to I1399 on P2-helix in DIII is in agreement with the significant coupling energy between R10 and D1241 on P2-helix in DIII previously reported in rNav1.4 (15). We also observed the interaction between KIIIA N3 and E307 in the extracellular loop S5P1 in DI but this interaction may not be substantial as it is fully exposed in the bulk solvent. Indeed, N3 has been shown to be not critical for KIIIA interaction with rNav1.2 and rNav1.4 (13).

Functional mapping of KIIIA residues at toxin – channel interface

To characterize accuracy of our KIIIA – hNav1.7 model, we first tested the activity of the wild-type KIIIA on hNav1.7 using whole-cell voltage-clamp recordings as described in Methods. At the highest KIIIA concentration (10 μM) tested we observed up to $\sim 90\%$ inhibition of sodium current (Figure 6A), in agreement with previous studies (13, 15). To estimate the KIIIA binding affinity, we performed concentration-response experiments and obtained an IC_{50} of $0.40 \pm 0.08 \mu\text{M}$ and 95% maximal block (Figure 6B,C), which is 4-fold higher than the K_d of 97 nM previously reported for hNav1.7 (15). In our tests, the wild-type KIIIA showed very slow dissociation from the wild-type hNav1.7 during the time-course of the whole-cell voltage-clamp experiments (Figure 6A, Table 2) compared to the previously published k_{off} of 0.017 min^{-1} suggesting that our Hill fit might be underestimating the affinity of the toxin. The extremely slow dissociation of WT-KIIIA from hNav1.7 complicated accurate determination of dissociation kinetics, as less than 10% recovery was observed during the time-course of experiments lasting up to ~ 30 min. Constraining single exponential fits of the dissociation data to assume maximum recovery, we obtained k_{off} between 0.002 min^{-1} and 0.005 min^{-1} . Extrapolation of the linear rate of recovery from these

experiments provides an upper bound on the k_{off} of 0.003 min^{-1} and a K_d of 59 nM, respectively. We suggest that temperature differences between our experiments ($\sim 21^\circ\text{C}$) and previously published experiments ($\sim 25^\circ\text{C}$) might be responsible for the slower kinetics given the KIIIA binding site surrounded by the extracellular loop regions. Estimates of dissociation kinetics from constrained fits produce 7-fold higher affinity of $\sim 59 \text{ nM}$, which is closer to the previously reported K_d of 97 nM (15) and likely underestimates KIIIA block at low toxin concentrations during our concentration-response experiment. Overall, the activity of WT-KIIIA on hNav1.7 in our experiments was similar to previously reported data (15).

We next performed an alanine scan of KIIIA residues that are positioned at the interface with hNav1.7 in our model. KIIIA substitutions K7A and H12A had nearly 100-fold decreases in affinity for the wild-type hNav1.7 channel in agreement with previously published data (13, 15, 16), likewise only K7A had a major effect on block, with reduction of maximal block by 20% (Figure 6C). Our data revealed that KIIIA substitutions W8A and D11A had a 50- and 10-fold reduction in affinity for the wild-type hNav1.7 channel, respectively (Figure 6D). Notably, these KIIIA mutations have not been previously tested against hNav1.7. For most KIIIA point mutations, the association rate remained similar to wild-type KIIIA, with only D11A showing a modest 3-fold increase in association rate (Figure 6D). The change in affinity was largely driven by between 36- and 116-fold increases in toxin dissociation from neutralizing mutations for the basic KIIIA residues tested (Figure 6D). Kinetic data for k_{on} , k_{off} , K_d , and calculated fractional block at saturating concentration (F_{block}) are summarized in Table 2. KIIIA D11A substitution resulted in both an increase in k_{on} and k_{off} , which is potentially a result of the net increase in total charge caused by the mutation and the removal of a contact with T1398 on P2-helix in DIII according to our

model. Notably, D11A substitution had no effect on dissociation from rNav1.2, but had a small effect on rNav1.4 binding—increasing k_{off} 4-fold, but with very little effect on k_{on} (13).

Table 2

Kinetics of toxin variants binding to WT-hNav1.7 from whole-cell voltage-clamp experiments.

Fractional block at saturating concentrations determined from extrapolation from kinetic data.

<i>Channel and Toxin</i>	k_{on} ($\mu\text{M}^{-1}\text{min}^{-1}$)	<i>SEM</i>	k_{off} (min^{-1})	<i>SEM</i>	K_d (μM)	<i>SEM</i>	<i>Fblock</i>	<i>SEM</i>
<i>WT-hNav1.7 x WT-KIIIA</i>	0.054	0.011	0.003	0.001	0.059	0.007	0.95 ^a	0.033
<i>WT-hNav1.7 x KIIIA-K7A</i>	0.064	0.018	0.274	0.012	4.291	1.507	0.74	0.049
<i>WT-hNav1.7 x KIIIA-W8A</i>	0.110	0.045	0.329	0.097	2.990	1.719	0.90	0.094
<i>WT-hNav1.7 x KIIIA-D11A</i>	0.164	0.014	0.109	0.008	0.663	0.056	1.00	0.012
<i>WT-hNav1.7 x KIIIA-H12A^b</i>	0.047	0.027	0.349	0.240	7.405	2.801	0.88	-

a – Fractional block was determined from the Hill fit of concentration-response data (fig 5c).

b – Fractional block reported by McArthur, et al., 2011(15) was used to constrain kinetic parameter estimates from association experiments.

Functional mapping of hNav1.7 residues at toxin – channel interface

To identify the key residues forming the KIIIA receptor site on hNav1.7, we selected mutations in the P2-helices in DI and DII in the outer pore based on our earlier KIIIA – hNav1.7 model based on the bacterial channel NavAb (PDB: 3RVY, (27, 28)), which was then superseded by our current KIIIA – hNav1.7 model based on eeNav1.4 structure shown in Figure 5. Notably, our earlier and current KIIIA – hNav1.7 models have the same hNav1.7 residues in the P2-helices in DI and DII interacting with KIIIA. We tested the N365 and Y362 residues on the P2-helix in DI and E919 and D923 on the P2-helix in DII. We selected these residues to inform the accuracy of the novel orientation of KIIIA in our model (Figure 5F). The E919A mutation did not produce measurable current. The E919Q mutation produced functional currents and reduced binding of the wild-type

KIIIA by 42-fold (Figure 6E). The D923A mutation reduced affinity of the wild-type KIIIA by 40-fold (Figure 6E). N365A slightly increased toxin association, but made the block by KIIIA irreversible (Table 3). Y362C produced a modest increase in both association and dissociation yielding a 7.5-fold reduction in affinity (Figure 6E). This residue is of particular importance in TTX binding (29) and appeared to reduce the predicted maximal block by the wild-type KIIIA by ~20% (Figure 6C). Overall, hNav1.7 mutations E919Q, D923A, and Y362C reduce the binding of the wild-type KIIIA to hNav1.7 in agreement with our structural model of KIIIA – hNav1.7 complex and recent KIIIA – hNav1.2 structure (18).

Table 3

Kinetics of binding site mutations affecting WT-KIIIA from whole-cell voltage-clamp experiments.

Fractional block at saturating concentrations determined from extrapolation from kinetic data.

<i>Channel and Toxin</i>	<i>k_{on}</i> ($\mu\text{M}^{-1}\text{min}^{-1}$)	<i>SEM</i>	<i>k_{off}</i> (min^{-1})	<i>SEM</i>	<i>K_d</i> (μM)	<i>SEM</i>	<i>Fblock</i>	<i>SEM</i>
<i>WT-hNav1.7 x WT-KIIIA</i>	0.054	0.011	0.003	0.001	0.059	0.007	0.95 ^a	0.033
<i>Y362C x WT-KIIIA</i>	0.101	0.016	0.044	0.004	0.436	0.052	0.75	0.055
<i>N356A x WT-KIIIA</i>	0.086	0.006	irreversible	-	n.d.	-	n.d.	-
<i>E919Q x WT-KIIIA</i>	0.040	0.003	0.101	0.003	2.51	0.16	0.92	0.028
<i>D923A x WT-KIIIA</i>	0.083	0.022	0.193	0.022	2.34	0.41	0.89	0.037

a – Fractional block was determined from the Hill fit of concentration-response data (fig 5c)

Double Mutant Cycle Analysis of Key pairwise interactions between KIIIA and hNav1.7

To validate our KIIIA – hNav1.7 model using double mutant cycle analysis (30), we performed double-mutant experiments isolating the contributions of specific pairwise contacts to the binding energy between KIIIA and hNav1.7 (Figure 7). With KIIIA substitutions at positions K7, D11, and H12, and hNav1.7 mutations E919Q, D923A we were able to compare the single mutant to double-mutant effects to evaluate thermodynamic cycles (Figure 7A). Pairwise contacts can be identified on the basis of the path-independence from the wild-type condition to the double-mutant

condition: the reduction in binding energy resulting from a mutation to either side of an interacting pair should be non-additive in the double-mutant condition (30). Residue pairs that exhibit additive effects of the double-mutant relative to the single mutants would be expected to make little functional interaction. These effects are quantified by calculating the coupling coefficient and the coupling energy (see Methods). Strongly interacting residue pairs will have coupling coefficients significantly different from 1.0, while non-interacting pairs will trend towards a coupling coefficient close to 1 (30). While an apparent coupling of residues determined by this method can result from allosteric effects, combination with computational modeling and structural studies may suggest a direct interaction. We tested the following pairs of double mutants: E919Q x K7A, D923A x H12A, which both directly interacted in our model (Figure 8A), and E919Q x D11A, which did not interact directly in our model. E919Q x D11A greatly reduced the toxin affinity ($K_d = 14.2 \pm 5.8 \mu\text{M}$) relative to either of the single mutations, E919Q and D11A ($2.34 \pm 0.16 \mu\text{M}$ and $0.66 \pm 0.06 \mu\text{M}$, respectively) (Figure 7B and Table 4), with a coupling coefficient of 0.5 and a coupling energy of $0.4 \text{ kcal}\cdot\text{mol}^{-1}$ (Table 5). For E919Q and K7A the double-mutant showed similar binding affinity ($2.47 \pm 1.32 \mu\text{M}$ to the channel mutation alone ($2.51 \pm 0.16 \mu\text{M}$), while both had a lower affinity than the K7A variant on the wild-type channel ($4.29 \pm 1.51 \mu\text{M}$) (Figure 7A and Table 4). The D923A mutation reduced the affinity of KIIIA and did not have an additive effect with H12A (Figure 7A and Table 4). We calculated the coupling coefficients and coupling energies for the pairs as described in the materials and methods. We found strong coupling energies between H12 on KIIIA and D923 on hNav1.7 ($2.8 \text{ kcal}\cdot\text{mol}^{-1}$) (Table 5). We also found strong coupling energies between K7 on KIIIA and E919 on hNav1.7 ($2.5 \text{ kcal}\cdot\text{mol}^{-1}$) (Table 5). These results are consistent with the interactions observed in our model (Figure 8A) and the recent structure of KIIIA - Nav1.2 complex (18).

Table 4**Kinetics of double-mutant cycle pairs from whole-cell voltage-clamp experiments.**

Fractional block at saturating concentrations determined from extrapolation from kinetic data.

<i>Channel and Toxin</i>	<i>k_{on}</i> ($\mu\text{M}^{-1}\text{min}^{-1}$)	<i>SEM</i>	<i>k_{off}</i> (min^{-1})	<i>SEM</i>	<i>K_d</i> (μM)	<i>SEM</i>	<i>Fblock</i>	<i>SEM</i>
<i>WT-hNav1.7 x WT-KIIIA</i>	0.054	0.011	0.003	0.001	0.059	0.007	0.95 ^a	0.033
<i>WT-hNav1.7 x KIIIA-K7A</i>	0.064	0.018	0.274	0.012	4.29	1.51	0.74	0.049
<i>WT-hNav1.7 x KIIIA-D11A</i>	0.164	0.014	0.109	0.008	0.66	0.056	1.00	0.012
<i>WT-hNav1.7 x KIIIA-H12A^b</i>	0.047	0.027	0.349	0.240	7.40	2.80	0.88	-
<i>E919Q x WT-KIIIA</i>	0.040	0.003	0.101	0.003	2.506	0.16	0.92	0.028
<i>E919Q x KIIIA-K7A</i>	0.044	0.015	0.108	0.021	2.466	1.32	0.48	0.066
<i>E919Q x KIIIA-D11A</i>	0.124	0.046	4.640	0.461	14.19	5.79	0.92	0.028
<i>D923A x WT-KIIIA</i>	0.083	0.022	0.193	0.022	2.34	0.41	0.89	0.037
<i>D923A x KIIIA-H12A</i>	0.183	0.065	0.440	0.098	2.40	1.45	0.49	0.092

a – Fractional block was determined from the Hill fit of concentration-response data (fig 5c).*b* – Fractional block reported by McArthur, et al., 2011(15) was used to constrain kinetic parameter estimates from association experiments.**Table 5****Coupling coefficients and coupling energies from double-mutant cycle experiments**

	<i>D923A x H12A</i>	<i>E919Q x K7A</i>	<i>E919Q x D11A</i>
<i>E_{coupling} kcal·mol⁻¹</i>	2.81	2.51	0.40
Ω	0.008	0.014	0.50

Marked difference for KIIIA binding specificity among Nav channel isoforms

The differences in KIIIA binding affinity between the Nav channel isoforms likely arises from multiple sequence difference within the toxin binding site (Figure 8A and B). The recent structure of the KIIIA - hNav1.2 complex (31) confirmed the predictions from our structural model of the KIIIA - hNav1.7 complex with high accuracy. The backbone root mean square deviation (RMSD) of the KIIIA - hNav1.7 model and the KIIIA - hNav1.2 structure over the toxin binding region (formed by KIIIA, P1-helix, P2-helix, and extracellular loops) is ~ 1.0 Å. Specific pairwise

contacts between K7-E919 and H12-D923 in our KIIIA - hNav1.7 model validated by mutant cycle analysis appeared to be exact in the KIIIA - hNav1.2 complex structure with the corresponding pairwise contacts between K7-E945 and H12-D949 (Figure 8A and B) (31). Our KIIIA - hNav1.7 model also correctly predicted other non-tested contacts, including pairwise interactions between KIIIA N3 and W8 with E307 and Y339, respectively, on the extracellular S5-P1 loop of DI (Figure 8A and B). On the DI P2 helix, Y362 and N365 potentially contribute to the difference in specificity between the TTX-sensitive and TTX-nonsensitive isoforms. In the TTX-nonsensitive channels hNav1.5, hNav1.8, and hNav1.9, the corresponding residues are either Cys or Ser (for Y362) and Arg (for N365) (Figure 8B). Having a non-aromatic residue at Y362 position and Arg at the N365 position could severely influence interaction with K7 on KIIIA.

Interestingly, the KIIIA residues D11 and R10 in our KIIIA - hNav1.7 model are positioned similarly in the KIIIA - hNav1.2 structure, but details of toxin – channel interactions are different (Figure 8A). D11 forms a hydrogen bond with T1398 on the P2-helix in DIII in our KIIIA - hNav1.7 model (Figure 8A), but the substitution of Thr (T1398) hNav1.7 to Met (M1425) on the P2-helix in DIII in hNav1.2 removes this potential interaction and promoting a new hydrogen bond to be formed with the nearby residue Y1429 (31). Remarkably, residues T1398 and I1399 on the P2-helix in DIII of hNav1.7 are Met and Asp, respectively, in all other human Nav channels. R10 interacts with D1426 on the DII P2-helix in the hNav1.2 structure but the corresponding position in hNav1.7 is I1399 (Figure 8A and B). This difference potentially contributes to R10 interaction with the nearby acidic residue D1662 on the DIV extracellular S5-P1 loop in hNav1.7. Notably, Asp at position 1662 is only present in hNav1.7 - corresponding residues at this position in other Nav channel subtypes are Val, Ala, and Ser (Figure 8B).

We also identified several additional positions on the extracellular loop regions of Nav channels that may contribute to specific interactions between KIIIA and Nav channels. Both our KIIIA - hNav1.7 model and the KIIIA - hNav1.2 structure show the positively charged R14 forming cation – π interactions with Y1416 (hNav1.7) or Y1443 (hNav1.2) on the extracellular P2-S6 loop in DIII. Notably, in the KIIIA - hNav1.2 structure R14 is also in proximity to the negatively charged E919 on the extracellular S5-P1 loop in DII (31). However, in our KIIIA - hNav1.7 model R14 is in proximity to T893 on the extracellular S5-P1 loop in DII (which is corresponding to E919 in hNav1.2) and E1417 on the extracellular P2-S6 loop in DIII (Figure 8A and B). These structural and sequence differences might be responsible for KIIIA R14A mutant selectivity for hNav1.7 versus hNav1.2 (15).

Difference in structural dynamics of KIIIA binding to hNav1.7 and hNav1.2 revealed by molecular dynamics simulations

To further study the molecular mechanism of the KIIIA interaction with hNav1.7, we performed molecular dynamics (MD) simulation of our KIIIA - hNav1.7 complex model, as described in Methods. The 1 μ s simulation revealed relatively stable binding of KIIIA within the receptor site with notable dynamics of specific KIIIA residues. During the simulation the RMSD of hNav1.7 pore residues reached $\sim 5\text{\AA}$ and at the interface between KIIIA and hNav1.7 was $\sim 4\text{\AA}$ (Figure 9A). At the beginning of the simulation, a sodium ion is binding to E919 and E916 on the P1-P2-helix region in DII (Figure 9A). This agrees with the density identified as a sodium ion at the same position in the cryo-EM structure of the hNav1.2-KIIIA complex. Our MD simulation revealed that this sodium ion quickly diffused out to the extracellular bulk via the open passage formed between the KIIIA and channel, supporting the incomplete channel block observed in experiments (Figure 6) (13, 15). After the escape of the sodium ion from the selectivity filter, the KIIIA -

hNav1.7 structure relaxed in this state for about 100 ns and then dynamically changed towards a slightly different binding state in which K7 on KIIIA formed interactions with Y362 and E364 on the P2-helix in DI, and D1690 on P2-helix in DIV (Figure 9A). This agrees with our functional characterization of KIIIA - hNav1.7 interactions where we observed a 100-fold reduction in K_d for the K7A mutation on KIIIA and only a 42-fold reduction for E919Q mutation on the channel, a mutation that may not completely disrupt interaction at the 919 site with K7. R10 is still neighboring I1399 on the P2-helix in DIII and switched from interacting with D1662 on the extracellular S5-P1 loop in DIV to interacting with D1690 on the P2-helix in DIV (Figure 9A). Interestingly, with both K7 and R10 reaching towards the P2-helix in DIV during the MD simulation, the channel appeared to be more completely blocked in this configuration. In addition, we also observed dynamic coupling of other key residues on KIIIA with P2-helices and extracellular loop regions of hNav1.7 (Figure 9A). W8 interacted with K310 and Y339 on the extracellular S5-P1 loop in DI. H12 showed significant interactions with D923 on the P2-helix in DII and also with the backbone of P895 on the extracellular S5-P1 loop in DII. D11 is positioned deep at the interface between DII and DIII formed by W897 on the extracellular S5-P1 loop and E919 in P2-helix in DII and T1398 and Y1402 on P2-helix in DIII. R14 primarily interacted with Y1416 on the extracellular P2-S6 loop in DIII and did not maintain interaction with E1417 on the extracellular loop in DIII as identified in our model. Notably, R14 also formed interactions with T893, L894, and P895 on the extracellular S5-P1 loop in DII (Figure 9A).

We also studied the structural dynamics of the KIIIA interaction with hNav1.2 using the recently published cryo-EM structure of the KIIIA - hNav1.2 complex. Our MD simulation revealed relatively stable binding of KIIIA within the receptor site with notable dynamics of specific KIIIA residues. During the simulation the RMSD of the hNav1.2 pore residues reached $\sim 5\text{\AA}$ and at the

interface between KIIIA and hNav1.2 was $\sim 4\text{\AA}$ (Figure 9B). The sodium ion in the selectivity filter at the site formed by E942 and E945 on the P1-P2-helix region in DII of hNav1.2 quickly diffused out to the extracellular bulk, again in agreement with an incomplete block of KIIIA on Nav1.2 (13) and our simulation of the KIIIA - hNav1.7 model (Figure 9A and B). In contrast to our KIIIA – hNav1.7 simulation, after the escape of the sodium ion, we did not observe the transition of K7 to form interactions with E387 on P2-helix in DI and D1717 on P2 helix in DIV. K7 formed more stable interactions with E945 on the P2-helix in DII, and also N361, Y362 on the extracellular S5-P1 loop in DI. In contrast to the KIIIA - hNav1.7 simulation, R10 stably interacted with D1426 on P2-helix in DIII (Figure 9B) and did not form new interactions with D1717 on P2-helix in DIV. This configuration of K7 and R10 promoted a slight rotation of the KIIIA helical region around the principal axis and allowed other key residues to make new interactions with hNav1.2. Aside from Y362, W8 also interacted with other residues in the DI loop including N361 and K333. Interestingly, H12 mainly interacted with Y362 on the extracellular S5-P1 loop in DI and I914 and S915 on S5-P1 loop in DII (Figure 9B). D11 slightly shifted towards the P2-helix in DII and interacted with Y362 on the extracellular S5-P1 loop in DI and E945 on the P2-helix in DII. Similar to the KIIIA - hNav1.7 simulation, R14 stably interacted with Y1443 on the extracellular P2-S6 loop in DIII and E919 and L920 on the extracellular S5P1 loop in DII (Figure 9B).

We found intriguing specific differences in the K7 dynamics between KIIIA – hNav1.7 and KIIIA – hNav1.2 MD simulations. Notably, D1426 on P2-helix in DIII of hNav1.2 is conserved among all other Nav channel isoforms, except for hNav1.7, which has I1399 at this position (Figure 8). The absence of Asp at the 1399 position in hNav1.7 allowed the transition of R10 to interact with the nearby acidic residue D1690 on the P2-helix in DIV, and also promoted interaction of K7 with E364 on the P2-helix in DI and D1690 to have a more complete block of the channel as observed

in the hNav1.7-KIIIA simulations. Indeed, the functional studies showed that the mutation of Asp to Ile in Nav1.4 (D1241) at position corresponding to I1399 in hNav1.7 increased the fractional block, while the reversed substitution of Ile to Asp in Nav1.7 decreased the fractional block (15). In addition, R10A produced a 35% reduction in KIIIA block of Nav1.4, while the loss of toxin block caused by the R10A mutation was largely rescued by the Nav1.7-like Ile in the DIII P2 helix (15). These results suggest that the differential interactions that we observed here between KIIIA and hNav1.7 and hNav1.2 may indicate a potential structural basis for differences in molecular determinants of KIIIA binding to hNav1.7 versus other Nav channel isoforms.

Discussion

The cryo-EM structure of the KIIIA - hNav1.2 complex was published in January of 2019 (18) while this manuscript was in preparation. Our computational model of hNav1.7, docking of KIIIA to the hNav1.7 model, and functional testing of KIIIA and hNav1.7 mutations presented here were completed prior to the publication of KIIIA - hNav1.2 complex structure and the availability of the PDB coordinates. While hNav1.7 and hNav1.2 channels share sequence homology within most of the KIIIA binding region, they exhibit several key differences at the toxin - channel interface. Our computational structural modeling and experimental validation revealed that our KIIIA - hNav1.7 model agrees with the hNav1.2-KIIIA complex structure. Strikingly, we accurately predicted and functionally characterized specific pairwise contacts between K7 on KIIIA and E919 on the P2-helix in DII and also H12 on KIIIA and D923 on the P2-helix in DII. The similarity between our KIIIA – hNav1.7 model and the KIIIA – hNav1.2 structure highlights the predictive power of our structural modeling and functional testing approach with potential future applications to study other peptide toxin – channel interactions.

Our MD simulations provide comprehensive understanding of the dynamics of KIIIA binding to hNav1.7 and hNav1.2 channels that are beyond the static hNav1.7-KIIIA model and the hNav1.2-KIIIA structure. Different stable configurations of KIIIA binding to hNav1.7 and hNav1.2 revealed the importance of the P2-helix in DIII binding site where I1399 is potentially responsible for creating a more complete block in hNav1.7. Due to the dynamic nature of KIIIA binding to Nav channels as revealed by our simulation, we cannot rule out that both binding configurations may happen in hNav1.7 and hNav1.2 channels but with different fractions of time.

Another feature of the molecular mechanism of KIIIA binding are differences in the reversibility and irreversibility of some of the KIIIA mutants on different Nav channels. Cryo-EM structures of hNav1.2, hNav1.4, and hNav1.7 channels (25, 31, 32) revealed that the extracellular vestibule of the channel pore targeted by KIIIA is surrounded by several relatively long loop regions raising the possibility that KIIIA access pathway to the toxin binding site is relatively narrow. Restricted access and escape pathways for KIIIA binding agree with the relatively slow k_{on} and k_{off} rates observed in previously published data (2, 13, 15) and our functional studies (Figures 2 and 3).

Our computational modeling and functional testing approach to study molecular determinants of toxin – channel interactions can be potentially expanded to rational design of small peptides to target the selectivity region of Nav channels using Rosetta protein design approaches (33-35). The sequence differences between Nav channels in the pore extracellular loop regions and P2-helices suggest that protein design and optimization could create inhibitors selective for any Nav channel subtype. Novel, high-affinity, selective inhibitors of Nav channels will have transformative potential to define a new class of biologics to treat Nav channel related diseases, such as, chronic pain, cardiac arrhythmias, and epilepsy.

Conclusions

We generated a structural model of the KIIIA in complex with hNav1.7 and validated it by functional testing using alanine-scan mutagenesis of KIIIA and hNav1.7 and double mutant cycle analysis of specific pairwise toxin – channel interactions. Our structural model was further validated by long time-scale unbiased MD simulations of the KIIIA - hNav1.7 complex, which confirmed that acidic residues E919 and D923 on the P2-helix in DII of Nav1.7 contribute significantly to the binding energy, and that KIIIA forms multiple interactions with the extracellular loops in DI-III. Overall, our results are consistent with previously published experimental studies and reveal molecular determinants of the KIIIA interaction with human Nav channels. Our approach can be potentially useful for engineering of molecular probes to study Nav channels function and for rational design of novel therapeutics to treat chronic pain, cardiac arrhythmias, and epilepsy.

Acknowledgements

We would like to thank Drs. Heike Wulff, Jie Zheng, and Igor Vorobyov, and members of Yarov-Yarovoy and Sack laboratories for helpful discussions. We thank Dr. Nieng Yan (Princeton University) for sharing coordinates of electric eel and human Nav1.2 channel structures, and independent comparison of our KIIIA – hNav1.7 model to coordinates of KIIIA – hNav1.2 structure prior to release in Protein Data Bank. We thank Dr. Christoph Lossin (University of California, Davis) for providing hNav1.7 cell line and channel constructs, as well as Dr. William Catterall (University of Washington) for the tsa201 cell line. Anton 2 computer time was provided by the Pittsburgh Supercomputing Center (PSC) through Grant R01GM116961 from the National Institutes of Health. The Anton 2 machine (36) at PSC was generously made available by D.E.

Shaw Research. This research was supported by National Heart, Lung, and Blood Institute Grants U01HL126273 and R01HL128537 to VYY, UC Davis Academic Senate Award FL18YAR to VYY, NIH T32 GM099608 to IHK, and AHA 17PRE33670204 to IHK.

Materials and Methods

Homology modeling of hNav1.7 based on EeNav1.4 structure

The cryo-EM structure of the Nav1.4-beta1 complex from the electric eel (eeNav1.4) (PDB ID: 5XSY) (19) was used to generate the model of hNav1.7 channel using Rosetta structural modeling software (20, 21). Initially, we refined the published coordinates of eeNav1.4, without the beta1 subunit by using the Rosetta cryo-EM refinement protocol (37) and picked the lowest scoring density-refitted eeNav1.4 model to use as a template. The comparative modeling protocol RosettaCM (20) was then used in combination with the electron density of the eeNav1.4 to model the hNav1.7 structure. We generated 5,000 structural models of hNav1.7 and selected the top 500 lowest-scoring models for clustering analysis as described previously (38). Visual inspection of the top scoring clustered models was used to select the final model for the docking study.

Molecular docking of KIIIA to the hNav1.7 model

The solution NMR structure of KIIIA (PDB ID: 2LXG) (14) was used as an ensemble to dock to the hNav1.7 model using the RosettaScript XML scheme (21, 39). At first, we found that it is challenging for Rosetta to move the KIIIA structures to pass the narrow passage created by the extracellular loops to fully sample the binding site. We divided the docking protocol into two subsequent stages. In stage 1, docking was performed with the DI S5P1 and DIII S5P1 loops truncated and using full random translational and rotational perturbation of KIIIA at both low and high-resolution phases. This stage generated 20,000 structural models of the docking complexes. We then selected the top 1,000 models based on the total scores and filtered based on the Rosetta

$\Delta\Delta G$ (an estimate of the binding energy of a complex) to select the top 500 models. $\Delta\Delta G$ was computed by taking the difference of the Rosetta energies of the KIIIA – hNav1.7 complex and the separated KIIIA and hNav1.7 structures. We clustered these complexes using the Rosetta legacy clustering application. The center models of top 20 clusters then passed to stage 2 docking. In this stage, positions of KIIIA in the top 20 clusters were used to create 20 different starting docking trajectories with the full structure of hNav1.7 model including all the extracellular loop regions. The full translational and rotational perturbation used in the previous stage was turned off. Instead, only limited local perturbation was allowed in both centroid and full-atom refinement phases. Similar to stage 1, we generated 20,000 structural docking models and filtered based on the Rosetta total score and $\Delta\Delta G$ to select top 500 models, which then were clustered to finalize top 5 complexes for visual inspection. The selected docking model presented here has the best Rosetta $\Delta\Delta G$ and is the only one in the top 5 clusters models show good agreement with previously published data.

Molecular dynamics simulation of hNav1.7-KIIIA and hNav1.2-KIIIA complexes

The docking complex of hNav1.7-KIIIA and the cryo-EM structure of hNav1.2 (PDB ID: 6j8e) were used to setup systems for MD simulations. For the hNav1.2 structure, Rosetta density refinement protocol was applied as described above for the hNav1.7. The missing region on DI extracellular loop was modeled using Rosetta loop modeling. CHARMM-GUI (40) was used to embed the hNav1.7-KIIIA model and the hNav1.2-KIIIA structure (PDB ID: 6j8e) in a lipid bilayer of POPC with explicit TIP3P water molecules at a concentration of 150 mM NaCl. CHARMM36 forcefield was used for proteins, lipids, and waters in both systems. Equilibrations were run on our local GPU cluster using NAMD version 2.12 (41). After 10,000 steps of steepest

descent minimization, MD simulations started with a timestep of 1 fs with harmonic restraints initially applied to protein heavy atoms and some lipid tail dihedral angles as suggested by CHARMM-GUI (40). These restraints were slowly released over 2 ns. Harmonic restraints (0.1 kcal/mol/Å²) were then applied only to protein backbone atoms, and the systems were equilibrated further for 20 ns with a timestep of 2 fs. All bonds to H atoms were constrained using the SHAKE algorithm in order to use a 2 fs timestep. Simulations were performed in NPT ensemble with semi-isotropic pressure coupling to maintain the correct area per lipid, and constant temperature of 303.15 K. Particle Mesh Ewald (PME) method was used to compute electrostatic interactions. Non-bonded pair lists were updated every 10 steps with a list cutoff distance of 16 Å and a real space cutoff of 12 Å with energy switching starting at 10 Å.

We used the Anton 2 software version 1.31.0 for production runs of 1 μ s of each system on the Anton 2 supercomputer. Simulations were performed in the NPT ensemble at 303.15 K with 2 fs timestep. Non-bonded long-range interactions computed every 6 fs using the RESPA multiple time step algorithm. The multi-integrator algorithm was used for temperature and semi-isotropic pressure coupling and the u-series algorithm was used for long-range electrostatic interactions. A long-range Lennard-Jones (LJ) correction (beyond cutoff) was not used as was suggested for CHARMM36 lipid force field.

Cell culture and preparation

Electrophysiology experiments were performed on transiently transfected tsa-201 cells (gift from William Catterall) and a HEK 293T cell line stably expressing hNav1.7 (gift from Chris Lossin). Cells were grown at 37°C, 5% CO₂ in DMEM with high glucose, L-glutamine, and Sodium Pyruvate (Gibco) with 10% FBS, and 1% Penicillin/Streptomycin. The stable cell line was raised

in the same conditions with G418 as a selection agent. Cells were grown to 70% confluency in 35mm dishes and passaged every 2-3 days for tsa-201 and 3-4 days for the stable-cell line. Cells were washed with DPBS (Gibco) and dissociated with 0.05% Trypsin-EDTA (Gibco) and seeded to fresh dishes with pre-warmed media. tsa-201 cells were transfected via Lipofectamine 2000 24-48 hours prior to experiments with 1 μ g pCMV6-hNav1.7 (and mutants) and 0.5 μ g pMaxGFP for identification of transfected cells. Prior to experiments cells were washed with DPBS and dissociated in Versene (Gibco) and scraped from the dishes and transferred to a 14mL conical tube in 3:1 DMEM:Versene. They were centrifuged at 1000 x g for 2 minutes and resuspended in a microfuge tube in 1mL extracellular solution with 10 mM D-glucose and rotated at RT until use.

Toxin preparation

Lyophilized WT-KIIIA was purchased (Alomone labs, Jerusalem, IS), reconstituted in water and stored as 100 μ M stock aliquots at -80°C prior to use. Toxin variants were produced by solid state synthesis as described previously (13) and stored as stock aliquots at -80°C prior to use. Stock concentrations were checked by Nanodrop with extinction coefficients determined by the ExPASy ProtParam online tool (42). Stock aliquots of toxin were suspended in 2xExternal solution with 0.2% BSA for working solutions of toxin in vehicle of 1xExternal solution with 0.1% BSA. Vehicle for controls were prepared in the same manner.

Electrophysiology

Whole-cell voltage-clamp recordings were performed at RT (~21-22°C) in a 100 μ L recording chamber mounted on a Zeiss Axiovert 35 microscope illuminated with a Zeiss HBO 100W

AttoArc lamp and filter set for epifluorescent detection of GFP expressing cells. Approximately 40 μ L of cell suspension was added to the pre-filled chamber and allowed to adhere to the glass bottomed chamber for 2-10 minutes. Fresh external solution was perfused through the chamber prior to patching. 1-2 M Ω borosilicate pipettes (Sutter instruments) pulled, fire-polished, coated with Sylgard, and filled with the internal recording solution. GFP expressing cells were patched and signals were amplified with an Axon Axopatch 200-B (Molecular Devices). G Ω seals were obtained, and pipette capacitance was corrected for prior to break-in achieved by suction. Access resistance (R_s) was typically 1-4 M Ω . 60%-80% R_s compensation was used to reduce voltage error to less than 10mV. P/5 leak subtraction protocol was used during recording. Signals were filtered with a low-pass Bessel filter at 5-10 kHz. Signals were digitized at [20 kHz? check] and recorded with Patchmaster (version)(HEKA) on a Windows 7 PC. The solutions were as follows in mM: External 3.5 KCl, 155 NaCl, 10 HEPES, 1 MgCl₂, 1.5 CaCl₂ adjusted to pH 7.4 with NaOH, and 315 mOsm; Internal: 35 NaCl, 70 CsCl, 50 CsF, 1 EGTA, 10 HEPES adjusted to pH 7.4 with CsOH at 310 mOsm. After break-in, cells were held at -120 mV and tested for stable Na⁺ current with depolarizing 35 ms voltage steps to -10 mV from -120 mV collected every 5 s for up to 5 minutes to allow for a stable level of current prior to vehicle addition. Once stable current levels were achieved, 150 μ L of vehicle was added to the bath via pipette with displaced solution removed via an overflow vacuum line. After approximately? pulses (minutes?) whole cell parameters were checked, and toxin was added via pipette as with vehicle during recording, with vacuum suction removing displaced bath solution. Once apparent block plateaued, whole cell parameters were re-checked, and pulsing resumed. To measure dissociation, gravity fed perfusion with fresh external solution was started at a rate 1-2 mL/min during recording.

Data analysis

Electrophysiology data were analyzed and plotted in IGOR 7 Pro (Wavemetrics). Geometric means of kinetic parameters were determined using Excel (Microsoft) and plotted in IGOR 7 Pro. Peak currents during depolarizations were plotted by time and data were fit with single exponential function (equation 2) during association and dissociation to get tau values shown. The association rate k_{on} was determined by equation 3, k_{off} was determined by equation 4. Affinity was determined kinetically as the dissociation constant K_d via equation 5. The slow dissociation of WT-KIIIA from WT-hNav1.7 made thorough measurement of k_{off} difficult, thus values shown here are best estimates from fits with the amplitude constrained based on the maximal current before toxin association. The resulting values of affinity are consistent with previous reporting of kinetic determination of affinity for this channel (15). IC_{50} was determined for WT-KIIIA x WT-hNav1.7 to estimate the maximal block (equation 1). The IC_{50} was higher than expected, though when used place of K_d for coupling energy calculations the coupling energies for D923A x H12A and E919Q x K7A remain above our threshold of 1.0 kcal/mol. The low affinity of H12A hindered precise measurement of kinetics, thus the rates are extrapolated from Fractional block assuming maximal block at saturating concentration of 0.877 as reported previously (15).

Equations

[1] Hill equation to determine residual current:
$$I_{Na^+} = 1 - \frac{1}{1 + \frac{[Tox]^h}{IC_{50}}}$$

[2] Single exponential fit for association and dissociation kinetics:
$$I_{Na^+} = y_o + Ae^{-t-t_0/\tau}$$

[3] Association rate:
$$k_{on} = \frac{\frac{1}{\tau_{on}} - k_{off}}{[tox]}$$

[4] Dissociation rate: $k_{off} = \frac{1}{\tau_{off}}$

[5] Affinity: $K_d = \frac{k_{off}}{k_{on}}$

[6] Fractional block at saturating concentration: $F_b = F_{[tox]} \left(1 + \frac{K_d}{[tox]} \right)$

[7] Coupling Coefficient: $\Omega = \frac{K_{dww} * K_{dmm}}{K_{dwm} * K_{dmw}}$

[8] Coupling Energy: $E_{coupling} = -RT \ln \Omega$

Figures

Figure 5

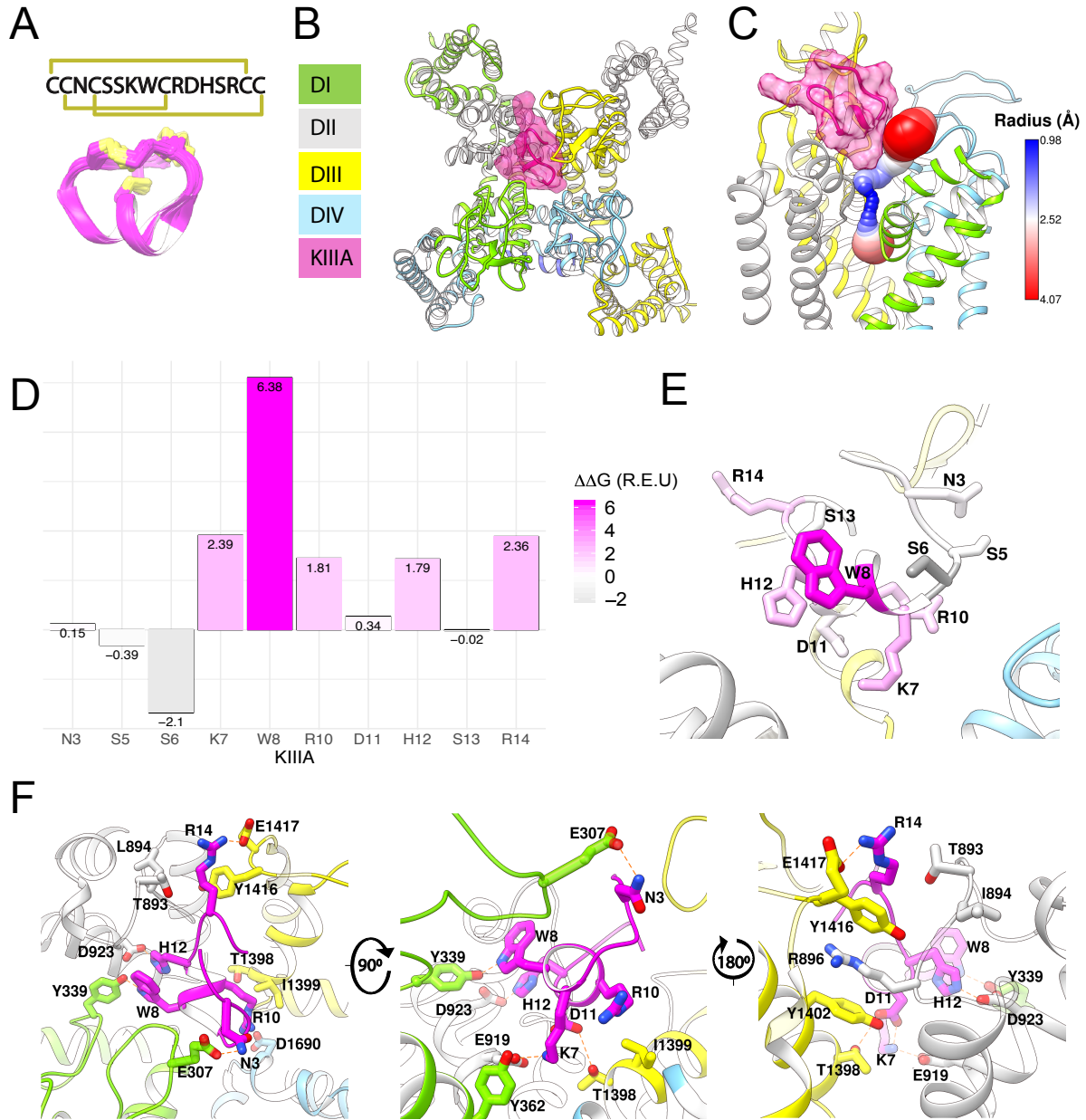


Figure 5: Homology model of hNav1.7-KIIIA features asymmetric binding of toxin to the outer pore. **(A)** Structure and sequence of KIIIA (PDB: 2LXG) (14) shows alpha helical core stabilized by three disulfide bridges and with an amidated C-terminus. **(B)** Extracellular view of our homology model of KIIIA – hNav1.7 complex based on the EeNav1.4- β 1 cryo-EM structure (19). Channel domains are depicted according to color keys, and KIIIA is depicted in pink with the ribbon and surface shown. KIIIA binds asymmetrically to the outer pore between DII and DIII. **(C)** Side view of channel pore and selectivity filter region with KIIIA bound (pink) and cavity volume colored by diameter shows that main constriction point is still the selectivity filter with enough room for Na⁺ conduction. **(D)** Rosetta $\Delta\Delta$ G determination identified residues K7, W8, R10, H12, and R14 as significant contributors to binding energy. **(E)** Heatmap of Rosetta $\Delta\Delta$ G shows the importance of the helical region for binding. **(F)** Detailed view of interacting residues at KIIIA – hNav1.7 interface predicted by our model.

Figure 6

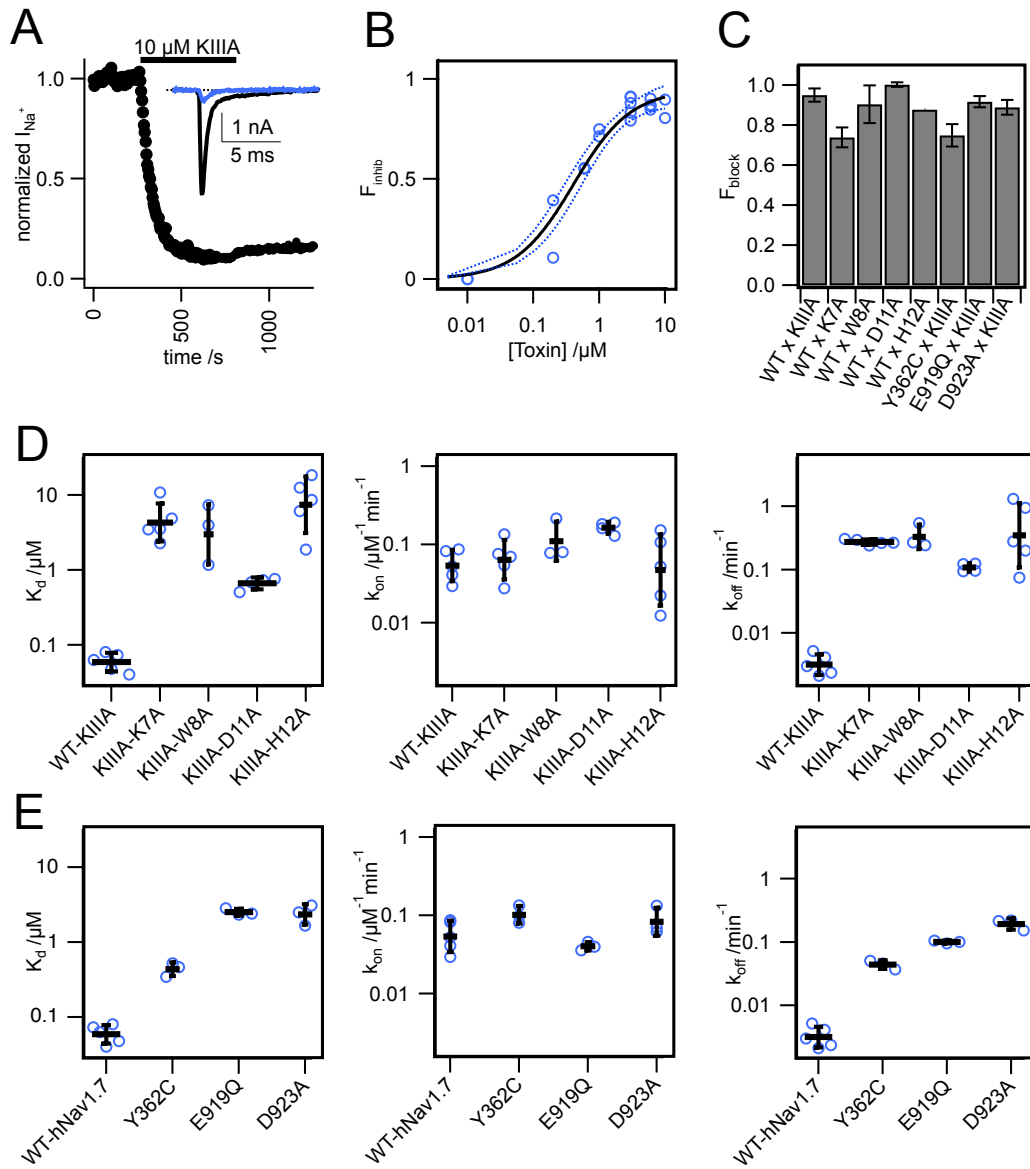
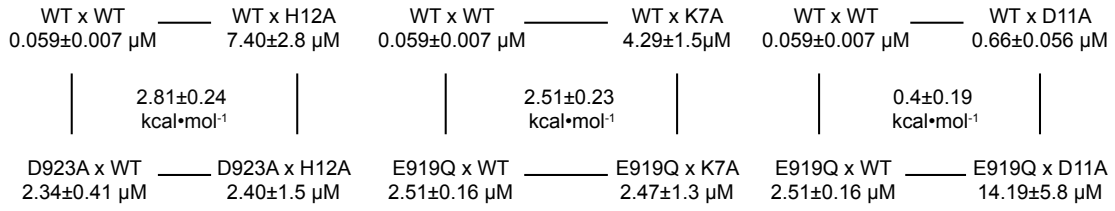


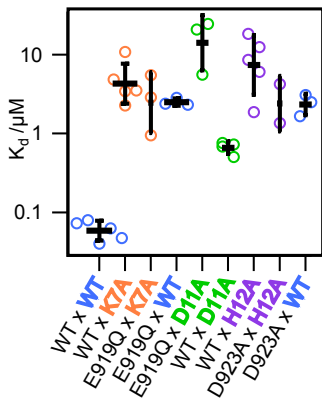
Figure 6: Functional mapping of KIIIA and hNav1.7 residues at toxin – channel interface. **(A)** WT-KIIIA blocks WT-hNav1.7 incompletely; I^*t plot of peak I_{Na^+} data from a single experiment and example current traces colored from first to last (red to blue), purple dots represent values in I^*t plot (inset). **(B)** Hill-fit of concentration-response data for WT-KIIIA against hNav1.7 in HEK293 cells ($IC_{50}=0.40\pm 0.08 \mu M$ mean \pm sd, $n=2-4$ cells per concentration), from maximum block recorded during association-dissociation experiments (right). **(C)** Calculated maximal block of KIIIA and its analogs from association-dissociation experiments. WT-hNav1.7 x H12A block data from McArthur, et al (15). **(D)** Kinetic data from electrophysiological measurements show general agreement with Rosetta predicted energies. Alanine variants of residues K7, W8, D11, and H12 showed significant reductions in affinity (left), little change in association (middle), but marked increases in toxin dissociation (right). Bars are geometric mean \pm sd from $n=3-5$ cells per variant, empty circles represent single cells. **(E)** Mutations to channel residues demonstrate reductions in affinity of the WT-KIIIA from Y362C, E919Q, and D923A (left), little change to toxin association (middle), and increases in dissociation (right), similar to the effects of toxin variants.

Figure 7

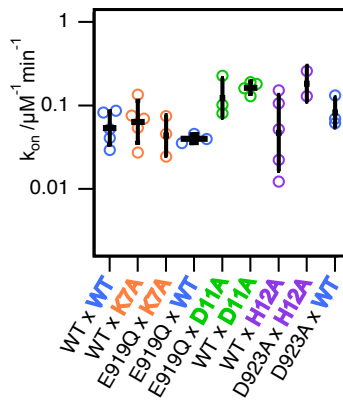
A



B



C



D

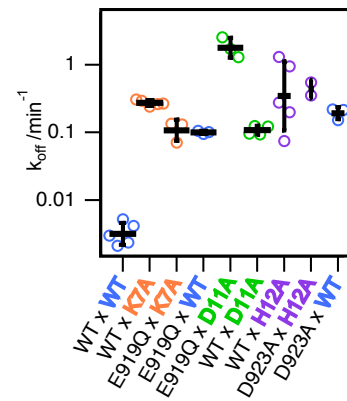
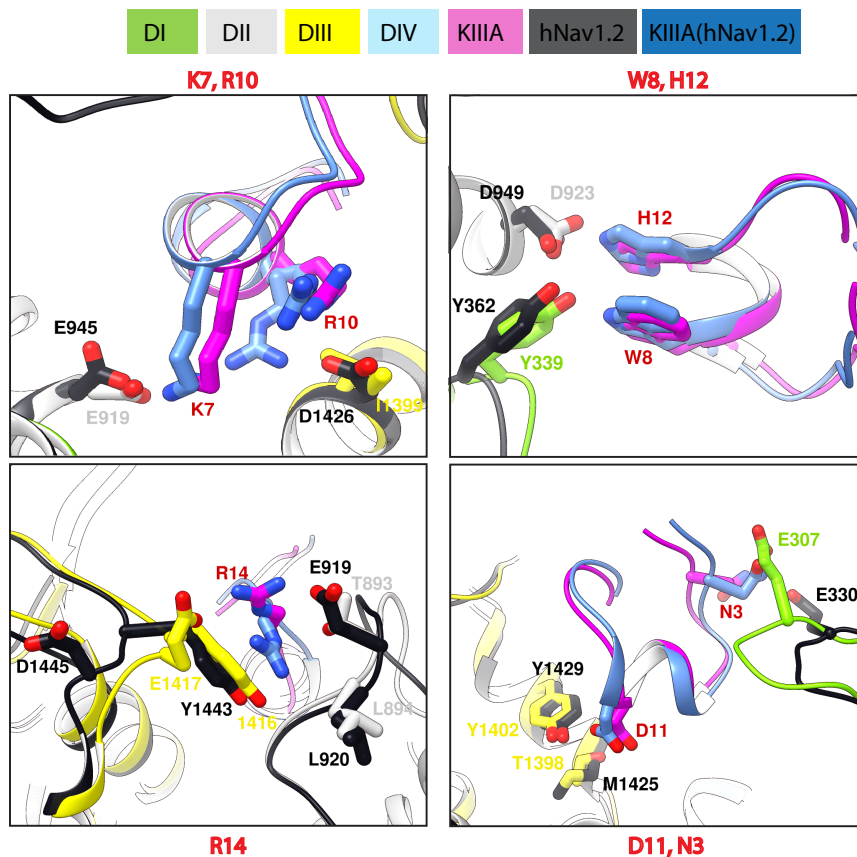


Figure 7: Double Mutant Cycle Analysis of key pairwise interactions between KIIIA and hNav1.7. (A) Double-mutant thermodynamic cycles between K7A x E919Q, H12A x D923A, and D11A x E919Q. values indicate difference from expected values if no interaction occurs. (B) Kinetic data for single and double mutants. The double mutants for K7A x E919Q and H12A x D923A were similar to the respective single mutant conditions, while the D11A x E919Q double mutant showed a much greater reduction in affinity relative to the single mutants (bars are geometric mean \pm sd, n=2-5 cells per condition, empty circles are individual cells).

Figure 8

A



B

	<u>N3</u>	<u>W8</u>	<u>K7</u>		<u>R14</u>	<u>K7</u>	<u>H12</u>
<i>DL_hNav1.7</i>	307 E G S K D A	338 D Y G	362 Y W E N L	<i>DII_hNav1.7</i>	888 I N D D C T - L -	917 W I E T M W D C	
<i>DL_hNav1.2</i>	E G Q N D A	- - - N Y G	- - - F W E N L	<i>DII_hNav1.2</i>	I S N D C E - L - - -	W I E T M W D C	
<i>DL_hNav1.1</i>	E G F L D A	- - - N Y G	- - - F W E N L	<i>DII_hNav1.1</i>	I A S D C Q - L - - -	W I E T M W D C	
<i>DL_hNav1.3</i>	D G Q K D P	- - - N Y G	- - - Y W E N L	<i>DII_hNav1.3</i>	I N D D C T - L - - -	W I E T M W D C	
<i>DL_hNav1.4</i>	E G S N D A	- - - N Y G	- - - Y W E N L	<i>DII_hNav1.4</i>	I A L D C N - L - - -	W I E T M W D C	
<i>DL_hNav1.5</i>	N G T S D V	- - - D H G	- - - C W E R L	<i>DII_hNav1.5</i>	- S D S G L - L - - -	W I E T M W D C	
<i>DL_hNav1.6</i>	P G M L E P	- - - N Y G	- - - Y W E N L	<i>DII_hNav1.6</i>	I N Q D C E - L - - -	W I E T M W D C	
<i>DL_hNav1.8</i>	R G T S D P	- - - D F N	- - - S W E R L	<i>DII_hNav1.8</i>	I S A P H E D W - - -	W I E N M W A C	
<i>DL_hNav1.9</i>	E N S P E F	- - - D Y N	- - - S W E K L	<i>DII_hNav1.9</i>	T G P T V S C L - - -	W I E N M W E C	
	S5P1 loop		P2 helix		S5P1 loop		P2 helix

	<u>R10, D11</u>	<u>R14</u>		<u>R10</u>		
<i>DIII_hNav1.7</i>	1343 T D G S R - - F P A	1398 T I I	1415 K Y E Y	<i>DIV_hNav1.7</i>	1662 D G I N	1690 D G L L A
<i>DIII_hNav1.2</i>	T T G E M - - F D V	- - - M D I	- - - K Y E D	<i>DIV_hNav1.2</i>	V G I D - - -	D G L L A
<i>DIII_hNav1.1</i>	T T G D R - - F D I	- - - M D I	- - - K Y E E	<i>DIV_hNav1.1</i>	V G I D - - -	D G L L A
<i>DIII_hNav1.3</i>	T T G N M - - F D I	- - - M D I	- - - V Y E E	<i>DIV_hNav1.3</i>	A G I D - - -	D G L L A
<i>DIII_hNav1.4</i>	T T S E R - - F D I	- - - M D I	- - - Q Y E V	<i>DIV_hNav1.4</i>	S G I D - - -	D G L L N
<i>DIII_hNav1.5</i>	T T E G D L P - L N Y	- - - M D I	- - - Q W E Y	<i>DIV_hNav1.5</i>	A G I D - - -	D G L L S
<i>DIII_hNav1.6</i>	T S E I R - - F E I	- - - M D I	- - - K Y E D	<i>DIV_hNav1.6</i>	A G I D - - -	D G L L L
<i>DIII_hNav1.8</i>	T D G E F S L V P L	- - - M D I	- - - K W E D	<i>DIV_hNav1.8</i>	A G I D - - -	D G L L S
<i>DIII_hNav1.9</i>	T D S V I N - - - Y	- - - M D I	- - - E F E S	<i>DIV_hNav1.9</i>	S G I D - - -	D S L L S
	S5P1 loop	P2 helix	P2S6 loop	S5P1 loop		P2 helix

Figure 8: Structural difference for KIIIA binding specificity among Nav channel isoforms. **(A)** Our hNav1.7 model closely resembles the hNav1.2- β 2-KIIIA cryo-EM structure especially at the key interacting points on the DII-P2 helix (left). The key sequence difference in DIII between Nav1.7 and all other isoforms T1398 I1399 vs MD, eliminates a key interaction with R10 seen in the cryo-EM structure, and introduces an interaction between D11 and T1398 (middle). The proximity of R10 to the conduction pathway is of particular importance to toxin efficacy. **(Right)** R14 makes contacts with DIII residues in both the cryo-EM structure and our model, though slight sequence differences and rotamers change the character of this interaction. T893 in DII is near R14, though is a glutamate in Nav1.2, and the E1417 in DIII adopts a different conformation to interact directly with R14 in our model while the two are separate in the Nav1.2 structure. **(B)** Sequence alignment of the different Nav subtypes with contact points (orange) and neighboring residues (yellow) show few sequence differences between the channel subtypes at the points of contact. The most prominent differences are in DIII T1398-I1399 and DIV D1609, which is an A, V, or S in all other subtypes, both of which sit near R10 in our model.

Figure 9

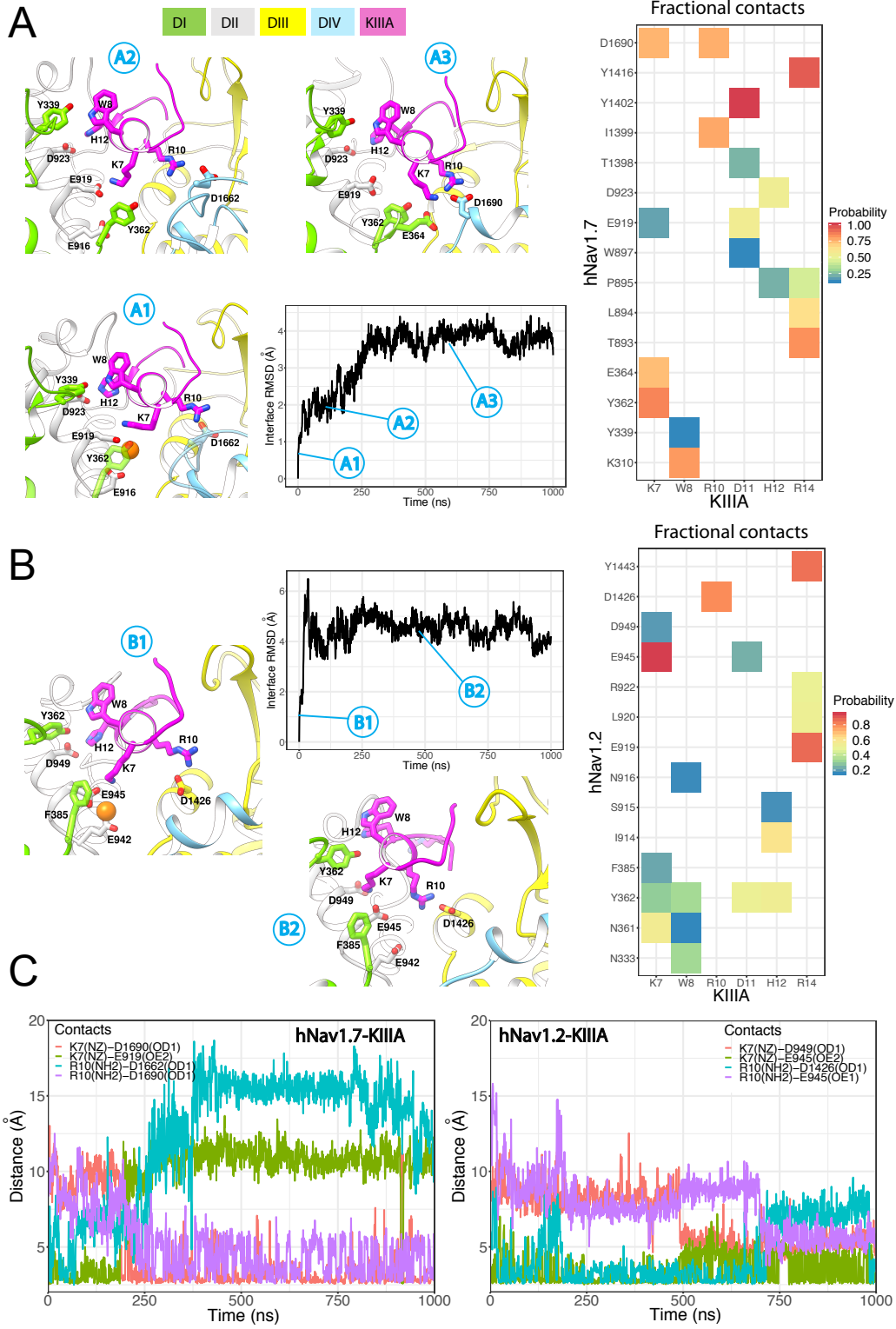


Figure 9: MD simulation of hNav1.7-KIIIA and hNav1.2-KIIIA complexes. **(A)** Structural dynamics of KIIIA binding in hNav1.7. Snapshots of KIIIA binding configurations with hNav1.7 during the simulation, associated with the interface RMSD (left and middle panels): 1, an equilibrated configuration with sodium ion in the selectivity filter; 2, a relaxed configuration after the escape of selectivity filter sodium ion; 3, stable configuration with K7, R10 reaching toward DIV P2 helix. Heatmap showing the probability of forming contacts between key residues on KIIIA and hNav1.7 channel during the simulation (right panel). **(B)** Structural dynamics of KIIIA binding in hNav1.2. Snapshots of KIIIA binding configurations with hNav1.2 during the simulation, associated with the interface RMSD (left and middle panels): 1, an equilibrated configuration with sodium ion in the selectivity filter; 2, a more stable configuration with strong interaction of R10 and D1426. Heatmap showing the probability of forming contacts between key residues on KIIIA and hNav1.2 channel during the simulation (right panel).

References

1. Hille B (2001) *Ion Channels of Excitable Membranes* (Sinauer Associates, Sunderland, MA)) 3rd Ed.
2. Wilson MJ, *et al.* (2011) μ -Conotoxins that differentially block sodium channels NaV1.1 through 1.8 identify those responsible for action potentials in sciatic nerve. *Proc Natl Acad Sci U S A* 108(25):10302-10307.
3. Catterall WA, Goldin AL, & Waxman SG (2005) International Union of Pharmacology. XLVII. Nomenclature and structure-function relationships of voltage-gated sodium channels. *Pharmacol Rev* 57(4):397-409.
4. Dib-Hajj SD, Cummins TR, Black JA, & Waxman SG (2010) Sodium channels in normal and pathological pain. *Annual review of neuroscience* 33:325-347.
5. Dib-Hajj SD, Yang Y, Black JA, & Waxman SG (2013) The Na(V)1.7 sodium channel: from molecule to man. *Nat Rev Neurosci* 14(1):49-62.
6. Lampert A, Eberhardt M, & Waxman SG (2014) Altered sodium channel gating as molecular basis for pain: contribution of activation, inactivation, and resurgent currents. *Handb Exp Pharmacol* 221:91-110.
7. Nguyen PT, DeMarco KR, Vorobyov I, Clancy CE, & Yarov-Yarovoy V (2019) Structural basis for antiarrhythmic drug interactions with the human cardiac sodium channel. *Proc Natl Acad Sci U S A* 116(8):2945-2954.
8. Yarov-Yarovoy V, *et al.* (2002) Role of amino acid residues in transmembrane segments IS6 and IIS6 of the Na⁺ channel alpha subunit in voltage-dependent gating and drug block. *J Biol Chem* 277(38):35393-35401.
9. Yarov-Yarovoy V, *et al.* (2001) Molecular determinants of voltage-dependent gating and binding of pore-blocking drugs in transmembrane segment IIIS6 of the Na(+) channel alpha subunit. *J Biol Chem* 276(1):20-27.
10. Ragsdale DS, McPhee JC, Scheuer T, & Catterall WA (1994) Molecular determinants of state-dependent block of Na⁺ channels by local anesthetics. *Science* 265(5179):1724-1728.
11. Gilchrist J, Olivera BM, & Bosmans F (2014) Animal toxins influence voltage-gated sodium channel function. *Handb Exp Pharmacol* 221:203-229.
12. French RJ, Yoshikami D, Sheets MF, & Olivera BM (2010) The tetrodotoxin receptor of voltage-gated sodium channels--perspectives from interactions with micro-conotoxins. *Mar Drugs* 8(7):2153-2161.
13. Zhang MM, *et al.* (2007) Structure/function characterization of micro-conotoxin KIIIA, an analgesic, nearly irreversible blocker of mammalian neuronal sodium channels. *J Biol Chem* 282(42):30699-30706.
14. Khoo KK, *et al.* (2012) Distinct disulfide isomers of μ -conotoxins KIIIA and KIIIB block voltage-gated sodium channels. *Biochemistry* 51(49):9826-9835.
15. McArthur JR, *et al.* (2011) Interactions of key charged residues contributing to selective block of neuronal sodium channels by μ -conotoxin KIIIA. *Mol Pharmacol* 80(4):573-584.
16. Zhang MM, *et al.* (2009) Synergistic and antagonistic interactions between tetrodotoxin and μ -conotoxin in blocking voltage-gated sodium channels. *Channels (Austin)* 3(1):32-38.
17. Korkosh VS, Zhorov BS, & Tikhonov DB (2014) Folding similarity of the outer pore region in prokaryotic and eukaryotic sodium channels revealed by docking of conotoxins

- GIIIA, PIIIA, and KIIIA in a NavAb-based model of Nav1.4. *J Gen Physiol* 144(3):231-244.
18. Pan X, *et al.* (2019) Molecular basis for pore blockade of human Na(+) channel Nav1.2 by the mu-conotoxin KIIIA. *Science* 363(6433):1309-1313.
 19. Yan Z, *et al.* (2017) Structure of the Nav1.4-beta1 Complex from Electric Eel. *Cell* 170(3):470-482 e411.
 20. Song Y, *et al.* (2013) High-resolution comparative modeling with RosettaCM. *Structure* 21(10):1735-1742.
 21. Bender BJ, *et al.* (2016) Protocols for Molecular Modeling with Rosetta3 and RosettaScripts. *Biochemistry* 55(34):4748-4763.
 22. Gray JJ, *et al.* (2003) Protein-protein docking with simultaneous optimization of rigid-body displacement and side-chain conformations. *J Mol Biol* 331(1):281-299.
 23. Wang C, Bradley P, & Baker D (2007) Protein-protein docking with backbone flexibility. *J Mol Biol* 373(2):503-519.
 24. Kubota T, *et al.* (2017) Mapping of voltage sensor positions in resting and inactivated mammalian sodium channels by LRET. *Proc Natl Acad Sci U S A* 114(10):E1857-E1865.
 25. Shen H, Liu D, Wu K, Lei J, & Yan N (2019) Structures of human Nav1.7 channel in complex with auxiliary subunits and animal toxins. *Science*.
 26. Shen H, *et al.* (2018) Structural basis for the modulation of voltage-gated sodium channels by animal toxins. *Science*.
 27. Payandeh J, Scheuer T, Zheng N, & Catterall WA (2011) The crystal structure of a voltage-gated sodium channel. *Nature* 475(7356):353-358.
 28. Kimball IH, Nguyen PT, Sack JT, & Yarov-Yarovoy V (2016) Mapping the Nav1.7 Channel Interaction with the Conotoxin KIIIA. *Biophysical Journal* 110(3):437a-437a.
 29. Penzotti JL, Fozzard HA, Lipkind GM, & Dudley SC, Jr. (1998) Differences in saxitoxin and tetrodotoxin binding revealed by mutagenesis of the Na⁺ channel outer vestibule. *Biophys J* 75(6):2647-2657.
 30. Hidalgo P & MacKinnon R (1995) Revealing the architecture of a K⁺ channel pore through mutant cycles with a peptide inhibitor. *Science* 268(5208):307-310.
 31. Pan X, *et al.* (2019) Molecular basis for pore blockade of human Na(+) channel Nav1.2 by the mu-conotoxin KIIIA. *Science*.
 32. Pan X, *et al.* (2018) Structure of the human voltage-gated sodium channel Nav1.4 in complex with beta1. *Science*.
 33. Silva DA, *et al.* (2019) De novo design of potent and selective mimics of IL-2 and IL-15. *Nature* 565(7738):186-191.
 34. Hosseinzadeh P, *et al.* (2017) Comprehensive computational design of ordered peptide macrocycles. *Science* 358(6369):1461-1466.
 35. Bhardwaj G, *et al.* (2016) Accurate de novo design of hyperstable constrained peptides. *Nature* 538(7625):329-335.
 36. Shaw DE, *et al.* (2014) Anton 2: Raising the bar for performance and programmability in a special-purpose molecular dynamics supercomputer. *Sc14: International Conference for High Performance Computing, Networking, Storage and Analysis*:41-53.
 37. Wang RY, *et al.* (2016) Automated structure refinement of macromolecular assemblies from cryo-EM maps using Rosetta. *Elife* 5.
 38. Bonneau R, *et al.* (2002) De novo prediction of three-dimensional structures for major protein families. *J Mol Biol* 322(1):65-78.

39. Fleishman SJ, *et al.* (2011) RosettaScripts: a scripting language interface to the Rosetta macromolecular modeling suite. *PloS one* 6(6):e20161.
40. Jo S, Kim T, Iyer VG, & Im W (2008) CHARMM-GUI: a web-based graphical user interface for CHARMM. *J Comput Chem* 29(11):1859-1865.
41. Jiang W, *et al.* (2011) High-performance scalable molecular dynamics simulations of a polarizable force field based on classical Drude oscillators in NAMD. *J Phys Chem Lett* 2(2):87-92.
42. Gasteiger E, *et al.* (2005) Protein Identification and Analysis Tools on the ExPASy Server;. *The Proteomics Protocols Handbook*, ed Walker JM (Humana Press), pp 571-607.

CHAPTER 3

Structural modeling of Nav1.7 DIV voltage-sensor and docking of spider toxin modulators

This chapter describes my research modeling multiple states of a voltage-gated sodium channel voltage-sensing domain to examine channel modulation by peptide toxins from spiders.

Kimball, IH, Sack JT, and Yarov-Yarovoy, V

I conceived of and conducted all electrophysiology experiments, modeling, data analysis, and writing for this chapter.

Abstract

Novel therapeutics targeting the voltage-gated sodium channel Nav1.7 have the potential to treat pain disorders. Disulfide knot toxins from tarantulas provide scaffolds with evolved potency and selectivity for specific Nav channel states. To better understand the molecular mechanisms of channel modulation by peptide toxins and aid in future design of novel therapeutics, we utilized molecular modeling of the Domain IV voltage-sensing domain (VSDIV) of Nav1.7 in multiple states, and drew on recent structural data to characterize the potential interactions of several peptide toxins with resting and active states of the Nav1.7 VSDIV.

Introduction

Voltage-gated ion channels (VGICs) are critical for the physiological function of excitable tissues throughout the body. Their vast importance in normal physiological function is matched by their diversity, with different families of VGICs selectively conducting K^+ , Na^+ , or Ca^{2+} , acting in concert to allow complex activity of the cells and tissues where they are expressed. Perturbations in channel function by mutations, drugs or toxins, can lead to significant pathophysiology. Voltage-gated sodium (Nav) channels are particularly important for the rapid depolarizations of neurons and muscle cells that lead to action potentials and are comprised of nine different subtypes, Nav1.1-Nav1.9. Nav channels are differentially expressed with Nav1.1, 1.2, 1.3, and 1.6 primarily found in the central nervous system, Nav1.4 in skeletal muscle, Nav1.5 in the heart, and Nav1.7-Nav1.9 in the peripheral nervous system (1). Despite high sequence similarity between Nav channel subtypes, there are multiple unique amino acid residues present in each individual Nav channel subtype, which makes it possible to rationally design highly specific Nav channel modulators.

Extensive research has characterized the pathways and molecular mechanisms underlying normal and pathophysiological pain. This work has clearly identified Nav channels as primary drivers of transmission of pain signals through peripheral afferent sensory neurons (2). Multiple lines of evidence have identified the human Nav1.7 channel as one of the key players in pain signaling. Inherited pain disorders like Congenital Insensitivity to Pain (CIP), Inherited Erythromelalgia (IEM), and Paroxysmal Extreme Pain Disorder (PEPD), were found to be linked to specific loss-of-function (CIP), and gain-of-function (IEM, PEPD) mutations in the SCN9A gene that encodes the Nav1.7 protein (2-5). Nav1.7 is known to drive subthreshold depolarization and the rising phase of action potentials in small diameter sensory neurons and as such is important in the

generation of pain signal transmission to the central nervous system (2). It is also expressed in olfactory neurons and vagal sensory neurons affecting irritation-induced cough, though its precise role in these tissues is less well understood (6, 7). The importance of this channel to pain research and the unknown roles it may play based on expression in sympathetic ganglia neurons, make it a prime target for further research into its function and pharmacology.

With the high sequence homology among VGICs and their ubiquitous expression throughout the body, the specificity of potential therapeutics is a particularly challenging problem in the development of new Nav channel modulators. One possible solution comes from peptide toxins from invertebrates that target VGICs to disrupt physiological functions of their recipients for defense or predation (8). One class of peptide toxins targets specifically the voltage-sensors of VGICs. The binding of these toxins stabilize resting states of the voltage sensing domains (VSDs), thus locking the pore domain helices in a closed state, preventing the ionic current that normally results from the movement of VSDs in response to membrane depolarizations (8). Many of these toxins shift the voltage-dependence of channel activation to more positive voltages, resulting in closed channels and disruption of neuronal and/or muscle activity. Many of these VSD-targeting toxins from spiders share a similar structural fold and sequence motifs that lead to their similar actions against different VGICs, though the structural contributors of this specificity are not well understood. Some toxins have a naturally high affinity for specific channel types, while others are more promiscuous and can affect multiple subtypes of one family of channels or multiple families of channels such as voltage-gated sodium (Nav) channels and voltage-gated potassium (Kv) channels. The evolved diversity, potency and specificity of these toxins makes them useful structural scaffolds for development of potential therapeutics if they can be optimized to have higher specificity and stability as has been achieved in some cases (9).

The main remaining difficulty for demonstrating that VGICs like Nav1.7 constitute druggable targets is the identification of selective modulators of channel activity that can reach the channel *in vivo* at sufficient concentration to produce the desired effect (5). Peptide-based drugs face several challenges from this perspective: their relatively large molecular weight and poor membrane permeability limit their ability to cross the blood brain barrier (BBB), they face rapid degradation and elimination in the urine, and as foreign proteins risk triggering immune responses (10). The potential for picomolar potency with such drugs provides a larger therapeutic window, with modifications such as non-canonical amino acid residues to enhance target specificity (11, 12), cyclization to prevent degradation (13), and PEGylation to limit renal elimination (14). Site-specific administration such as intrathecal injection can also limit off-target effects and provide access to non-BBB permeable drugs. Advances in the design of cyclic peptides enhance their stability and provide a future avenue for utilizing structural information from studies like this (15).

The ability to study and treat particular disorders arising from altered channel expression or function, or channelopathies, relies not just on the knowledge of target identity, but of the structure-function relationship imparted by the amino acid sequence differences between channel types and subtypes. Likewise, modulation of VGICs by toxins depends largely on the location and orientation of specific binding site that allows it to alter channel function. Nav channels are comprised of a single polypeptide chain arranged into four homologous domains that each exhibit different voltage-dependence and effect on channel conductance. Domain I (DI) through DIII contribute primarily to opening of the inner gate upon depolarization-induced activation, while DIV activation leads to fast inactivation of the channel, producing the characteristic activation and inactivation profile of Nav channels. The locations of potential binding sites and

their roles have been thoroughly studied (8, 16) and provide useful comparisons for modulation from new channel-toxin combinations. For example, several spider toxins have been shown to target Nav1.7-VSDII specifically affecting channel activation by trapping the VSDII in a resting state (17-19), while alpha-scorpion toxins are known to trap a resting state of the VSDIV, preventing channel fast-inactivation (20). Knowledge of these activities allows us to hypothesize about the mechanisms of toxins from their functional profiles.

SGTx-1 is a toxin that traps voltage sensors of Kv2.1 channels in a resting conformation ((21, 22)). This binding leads to a depolarizing shift in the voltage-dependence of activation of these channels (21). This effect is dependent on binding the voltage-sensing domain as well as significant interaction of the toxin with the membrane (23) . It has also been found to affect Nav channel voltage sensor movement in a domain selective manner in chimeric channels and heterologously expressed Nav1.2 channels (24). During depolarizing voltage steps, homotetrameric channels constructed from S1-S4 of Nav1.2- domain IV voltage-sensor (VSDIV) and the pore-forming S5-S6 from Kv2.1 were inhibited by bath application of SGTx-1. This effect was not observed by chimeric channels featuring the other 3 VSDs from Nav1.2. Other toxins, however did elicit reduction in current from multiple VSD chimeras suggesting that SGTx-1 inhibits VSDIV movement, but not other VSDs. SGTx-1 was further tested on intact Nav1.2 channels and found to slow the time-course of channel inactivation after depolarization, consistent with inhibition of VSDIV movement which is necessary for channel inactivation (25). The effect of SGTx-1 on Nav1.2 mimics the activity of scorpion toxins that bind to the canonical toxin receptor site 3 such as AaHII (16) that leads to a reduction in the rate of channel inactivation. Site 3 is known to be the VSDIV.

If the activity of SGTx-1 on Nav-VSDIV follows a similar mechanism of action as the toxin does on Kv channels, it follows that functional data from experiments examining the toxin's effect on Kv channels could inform hypotheses of toxin effect on Nav channels. Alanine-scans of SGTx-1 have identified an active surface of the toxin including residues that aid partitioning and binding including R3, L5, F6, R22, and W30 (22). These results can be used to constrain the potential mechanism of action affecting Nav channels.

Recent publication of several cryo-EM structures of invertebrate, vertebrate and human Nav structures in conjunction with peptide toxins also provides a large body of structural information to predict the binding mode of SGTx-1 to Nav1.7 VSDIV. In particular, the cryo-EM structure of the hNav1.7 in complex with β subunits β 1 and β 2 shows unresolved densities at the putative binding site of ProTx-II: the S3-S4 loop of both VSDII and VSDIV (PDB:6J8I) (26). This toxin shares a similar fold with SGTx1 and provides a template for toxin interaction with the active state of Nav1.7 VSDIV. We also have useful data from the structure of a chimeric Nav1.7-VSDII bound to the toxin in a deactivated state (PDB:6N4R) (19). While the Nav1.7-VSDII has a different sequence compared to Nav1.7-VSDIV including a shorter S3-S4 loop, the orientation of the toxin and its proximity to the membrane could inform SGTx-1 binding to Nav1.7-VSDIV. The crystal structure of an Nav1.7-VSDIV/NavPas chimera in complex with the scorpion toxin AaHII (PDB:6NT4) (27) is of particular interest to this study because it demonstrates the potential binding and VSDIV state necessary to inhibit channel inactivation by a peptide toxin. Together we have structural data that provides state and binding information yet requires further modeling to produce a plausible description of the action of toxins like SGTx-1 and their domain specificity for Nav channels. To draw on the available structures and functional data, we used

Rosetta molecular modeling software to generate models of the molecular details of peptide toxin - Nav1.7-VSDIV interactions.

Results and Discussion

Electrophysiological characterization of SGTx-1 activity on hNav1.7

The well-characterized Kv channel peptide toxin inhibitor SGTx-1 has been shown to target the VSDIV of Nav1.2, preventing activation of Nav1.2-Kv2.1 chimeric channels and prolonging fast-inactivation in hNav1.2 channels (24). Given the sequence homology between neuronal Nav subtypes, we sought to determine if SGTx-1 will also have an effect on fast-inactivation in hNav1.7. I performed whole-cell voltage-clamp electrophysiology in tsa201 cells heterologously expressing Nav1.7 alpha subunits. Addition of 5 μM SGTx-1 rapidly slowed the apparent inactivation time-constant of hNav1.7 current during depolarizing voltage steps, with the kinetics returning to baseline upon toxin washout (Figure 10A-C). Single exponential fits of the change in these time-constants from toxin association (Figure 10A, B) and dissociation (Figure 10C) yielded time-constants to calculate the on-rate (k_{on}) and off-rate (k_{off}) and affinity (K_d) (see Materials and Methods). Proper fitting at the concentration tested was too rapid to measure with 5 s pulsing (Figure 10B), but assuming a τ_{on} of 5 s allowed for an upper bound of $k_{on} = 0.0351 \pm 8.74 \times 10^{-5} \mu\text{M}^{-1}\text{s}^{-1}$ (mean \pm sd), and $k_{off} = 0.0244 \pm 4.37 \times 10^{-4} \text{s}^{-1}$ suggesting an affinity lower than $K_d = 0.694 \pm 0.142 \mu\text{M}$. More experiments need to be conducted to determine the true affinity and state-dependence of toxin binding, though these results suggest an ability to alter hNav1.7 channel gating by SGTx-1. SGTx-1 could have a non-specific membrane effect as a result of high concentrations of membrane-partitioning peptide toxin altering the channel

kinetics(28, 29). As a control for membrane partitioning and channel activity, I added 10 μ M of the Kv2-selective GxTx-1E peptide toxin, which has the same structural fold as SGTx-1 and significant membrane-partitioning(30). GxTx-1E did not alter hNav1.7 kinetics in a single trial (Figure 10D-G), supporting the claim that membrane-partitioning by a comparable peptide alone does not explain the effects seen by SGTx-1, though further replications and study would be required to definitively rule out such an effect.

State-modeling of Nav1.7 VSDIV

We have seen the potential ability of SGTx-1 to affect the apparent inactivation of hNav1.7 channels expressed in tsa201 cells (Figure 10). This ability is possibly a result of toxin binding to the DIV voltage-sensor as seen in the chimeric studies of Nav1.2 (24). To identify potential contacts between SGTx-1 and hNav1.7, we first performed modeling of multiple resting states of the hNav1.7 VSDIV using multiple structural templates as has been described previously for the bacterial sodium channel NaChBac (31). Initial models of hNav1.7 VSDIV were generated based on the bacterial channel NavAb VSD (32)PDB ID:3RVY which is found with all VSD S4 helices in a fully up-state. The sequence difference between the two channels left a 12 residue gap in the alignment of the region of the S3-S4 loop (Figure 11A). The S1-S2, and S3-S4 loops were rebuilt de novo. Top scoring models were compared by clustering and visual inspection and the top model is displayed in Figure 11B. Resting state models were produced in the same manner, but with the S4 gating charges shifted three residues towards the C-terminus relative to the template for each VSD state to simulate the movement of S4 helix down in response to hyperpolarizing membrane potential. The corresponding S3-S4 loop was rebuilt to account for this change assuming relatively stable S1-S3 helices, for each case and top scoring models are

shown in Figure 11B. The release of new structural data of other VGICs provided potential for validation and the use of templates of alternate VSD states. Comparison of my NavAb-active state model with to the cryo-EM structure of hNav1.7 (PDB ID: 6J8I) (26) VSDIV and 5EK0-VSD-A reveals a tendency for the S3-S4 loop to be closer to the S1-S2 loop than in both structures, from a lack of curve in S3 and inward rotation of R1 and R2 sidechains. 5EK0 was closer to NavAb (Figure 11C).

In addition to the NavAb-based resting state models above, I built homology models of the hNav1.7-VSDIV based on the down-states of the S4 helices found in two subsequent structures: the Arabidopsis TPC1 (PDB:5E1J)(33), and the American cockroach sodium channel NavPas (PDB:5X0M)(34). Using Rosetta homology modeling to capture resting confirmation and rebuilding the S1-S2 and S3-S4 loops(35-37). Top scoring models from the 3 different templates showed similarities in a tendency to change conformation of the S3-S4 loop towards the center of the VSD (Figure 11D). Furthermore, following full-atom relax, the R3 gating charge in the TPC1-based model could adopt an up or down position relative to the S2 phenylalanine constituting the hydrophobic gasket, likely as a result of the elongated 3-10 helix present in the cryo-EM structure. Of these models the TPC1-based model was chosen for subsequent docking protocols due to more exposed S3-S4 segment. Following completion of these modeling efforts, several Nav structures were published that captured VSDs in resting states and bound to different invertebrate toxins(18, 19, 38, 39).

State-dependent docking of spider toxins to VSDIV models highlight potential contacts

Having generated resting state models, we sought to determine potential binding modes for the SGTx-1 peptide and performed molecular docking simulations with the Rosetta protein-protein

docking protocol (37) with resting states models of the hNav1.7 VSDIV. The resulting SGTx-1 - hNav1.7 VSDIV models suggested multiple potential docking poses that feature the C-terminal loop of the toxin facing the S3-S4 loop of the voltage sensor (Figure 12A), showing some convergence towards this result within the top 1000 scoring models (Figure 12B, 12C). Top-scoring models adopted two predominant binding modes, both with SGTx-1 oriented towards the outside of the voltage sensor with the C-terminus running along the S3-S4 loop and hydrophobic and aromatic residues facing the membrane (Figure 12D-E). The first mode shows the toxin making significant contact with the S3-S4 loop including residues that are consistent with the known toxin – membrane interactions (40) (Figure 12D). In the second, the toxin orients with the channel with the claw region facing the outer portion of S3 and making contact with the S3-S4 and the outer face of S2 (Figure 12E). Both SGTx-1 - hNav1.7 VSDIV binding modes are consistent with recent structures of the gating modifier peptide toxin - VSD complexes(18, 19, 26, 41). At the binding interface, SGTx-1 residues L5 and F6 interact with the membrane and outer edge of the S3 while W30 makes contact with the S3 and S3-S4 loop (Figure 12D,E). Comparison of these poses with the voltage-sensor trapping seen by the scorpion toxin AaHII (38) shows mechanistic contrast whereby the scorpion toxin prevents voltage sensor movement by occupying the space through which the voltage sensor would move during activation and the substitution of the voltage-sensor's R1 gating charge with its own arginine deep in the binding interface. Our SGTx-1 - hNav1.7 VSDIV model shows a more peripheral binding of the toxin to this resting state that would impinge on the remodeling of the S3-S4 loop necessary to enter an activated state, and does not appear to directly interact or interfere with the gating charges or their counter charges on the interior of the voltage sensor (Figure 12D-E).

Bosmans and Swartz (8) reviewed the functional characteristics of different mechanisms of Nav modulation by spider toxins, but at the time lacked either crystal and cryo-EM structures of Nav channels to make detailed conclusions about the molecular interactions of these channels with peptide toxins. Despite the overall similarity of many spider toxins in structural fold and sequence, SGTx-1 has promiscuous binding to different VGICs, while ProTx-II shows great specificity for Nav channels (42, 43). ProTx-II binds both VSDII and VSDIV based on functional testing (44) and recent structure determination (19, 26). The FLAD motif shown to interact with ProTx-II is present in both DII and DIV, and while it was shown to be the site of binding to DII (19), it is unknown what structural components drive the interaction with DIV. The recent cryo-EM structure of hNav1.7 in complex with ProTx-II (6J8I) (26) shows unsolved density above the activated state of the VSDIV believed to be from bound ProTx-II (Figure 13A). The density sits above the S3-S4 loop, similar to our resting state SGTx-1 docking results (Figure 12) and known toxin binding sites for other voltage sensors (19, 26, 45). We sought to characterize the interaction of ProTx-II with the activated state of VSDIV, using both docking and EM-density fitting protocols in Rosetta (Figure 13B). The top scoring models generated by this approach show a general binding mode with the C-terminal and claw portion of the toxin above the S3-S4 loop similar to that adopted by SGTx-1 in our resting state model though resting more on top of the loop (Figure 13B). This pose is stabilized by significant interactions between the basic and hydrophobic sidechains R22, W24, K26, and V20 of the toxin and the S3-S4 residues including E1589, T1590, Y1591, and V1593 with no observed interactions with the S2 segment (Figure 13C). Close comparison of the ProTx-II docking pose to our resting state model with SGTx-1 uncovers several differences. Despite targeting the same loop and attack from a similar portion of the toxin, the downward position of the S4 in the resting state presents a very

different set of contact residues for the toxins (Figure 13D). For example, in our resting state-model, Y1591 is turned in towards the S1-S2 segment for contact with SGTx-1, yet is interacting with W24 on the membrane facing surface of the VSD in the active state (Figure 13D). Indeed, Xu, et al (19) noted a similar incompatibility between the crystal structure of a hNav1.7-VSDII-NavAb chimeric channel that was resolved with ProTx-II bound, and the previous structure of an active state of Nav1.4-VSDIV bound to a small molecule inhibitor (27). While both VSDs shared the FLAD sequence at the toxin binding site, the state-dependent fold of the VSD necessitated a different binding pose of the toxin to accommodate the different VSDs, and could explain the state-dependent stabilization of voltage-sensors by such toxins.

Structural alignment of related toxins Pn3a and SGTx-1 reveals key differences at putative binding interface

Pn3a is a potent inhibitor of Nav1.7 and inhibits current in chimeric channels expressing only VSDII or VSDIV (46). Unlike SGTx-1, it produces a rightward shift in the voltage-dependence of channel activation and no effect on the apparent kinetics of inactivation (46). Interestingly, Pn3a shares homology with SGTx-1, yet with key differences at positions 23-25 (Figure 14A). SGTx-1 features a serine, aspartate, and glycine, while Pn3a features an arginine, lysine, and methionine at these positions, respectively. In our SGTx-1 docking model these residues are positioned between the outer edge of the S2 and S3 (Figure 14B, 14C). The proximity of these distinct chemical features with the potential binding site of these VSD-binding toxins coupled with their high sequence and structural similarity suggests this portion of the toxins may play an important role the determination of specificity and action in trapping VSDII vs. VSDIV of hNav1.7. Another important difference between the two toxins is the solution structure of Pn3a

features a C-terminal region that folds back towards the β -sheet and a dock similar to our model would position this portion over the S3-S4 loop and could be expected to play an important role in state dependence of binding (Figure 14C).

Conclusions

In this study I demonstrated a potential ability of SGTx-1 to modulate the inactivation kinetics of hNav1.7, modeled previously uncaptured states of the hNav1.7-VSDIV, and highlighted potential state-dependent interactions of this voltage-sensor with known gating modifier toxins. The conformation of the S3-S4 loop undergoes significant remodeling in its transition between different states and presents a highly variable target for VSD-toxins like SGTx-1 and ProTx-II, and Pn3a, where key sequence differences have could have drastic effects on relative potency state-dependence, and functional effect. Combined with future validation and the rapid increase in available structural data, these efforts could provide useful information towards the development of more targeted tools for ion channel research and potential therapeutics.

Acknowledgements

We thank Dr. William Catterall (University of Washington) and Dr. Cristoph Lossin (University of California, Davis) for providing cell lines, Dr. Kenton Schwartz (NINDS) for providing SGTx-1, and Drs. Heike Wulff, and Jie Zheng (University of California, Davis) and members of the Sack and Yarov-Yarovoy labs for helpful discussion. This research was supported by NIH Grant R01NS096317 to JTS, UC Davis Academic Senate Award to VYY, NIH T32 GM099608 to IHK, and AHA 17PRE33670204 to IHK.

Methods

Cell culture, transfection, and preparation: Electrophysiology experiments were performed based on methods previously reported as follows (47). Transiently transfected tsa-201 cells (gift from William Catterall). Cells were grown at 37°C, 5% CO₂ in DMEM with 4.5g/L D-glucose, L-glutamine, and 110 mg/L Sodium Pyruvate (Gibco cat# 11995-065) with 10% FBS, and 100 units/mL Penicillin/Streptomycin (Gibco cat# 15140-122). The stable cell line was raised in the same conditions with 500 µg/mL G418 as a selection agent. Cells were grown to 70% confluency in 35mm dishes and passaged every 2-3 days for tsa-201 and 3-4 days for the stable-cell line. Cells were washed with divalent-free DPBS (Gibco cat# 14190-144) and dissociated with 0.05% Trypsin-EDTA (Gibco cat# 25300-054) and seeded to fresh dishes with pre-warmed media. tsa-201 cells were transfected via Lipofectamine 2000 24-48 hours prior to experiments with 1 µg pCMV6-SCN9A (gift from Dr. Christoph Lossin, UC Davis) and 0.5 µg pMaxGFP (Lonza) for identification of transfected cells. Prior to experiments, cells were washed with DPBS and dissociated in 1mL Versene (Gibco cat# 15040-066) and scraped from the dishes and transferred to a 14mL conical tube with 3 mL DMEM. They were centrifuged at 1000 x g for 2 minutes and resuspended in a microfuge tube in 1mL extracellular solution (described below) with 10 mM D-glucose and rotated at RT until use.

Electrophysiology: Whole-cell voltage-clamp recordings were performed according to previous protocols as (47). Experiments were conducted at RT (21-22°C) in an RC-24N recording chamber fixed to a glass coverslip (Warner Instruments), mounted on a Zeiss Axiovert 35 microscope illuminated with a Zeiss HBO 100W AttoArc lamp and filter set for epifluorescent detection of GFP expressing cells. The recording solutions were as follows in mM: External 3.5 KCl, 155 NaCl, 10 HEPES, 1 MgCl₂, 1.5 CaCl₂ adjusted to pH 7.4 with NaOH, and 315 mOsm; Internal: 35 NaCl,

70 CsCl, 50 CsF, 1 EGTA, 10 HEPES adjusted to pH 7.4 with CsOH at 310 mOsm. Lyophilized SGTx-1 was a gift from Kenton Schwartz and was resuspended in water, diluted to final working concentration in 1X External Saline with 0.1% BSA. GxTx-1E was produced by solid state synthesis as described previously (48) and prepared as above. Approximately 40 μ L of cell suspension was added to the pre-filled chamber and allowed to adhere to the glass bottomed chamber for 2-10 minutes. Fresh external solution was perfused through the chamber prior to patching. Borosilicate pipettes (1.5 mm OD, 0.86 mm ID, Sutter instruments cat # BF150-86-7.5HP) were pulled to resistances of 1-2 M Ω , fire-polished, coated with Sylgard, and filled with the internal recording solution. GFP expressing cells were patched and signals were amplified with an Axon Axopatch 200-B (Molecular Devices) and acquired with an Instrutech LIH 8+8 ADC board (HEKA). G Ω seals were obtained, and pipette capacitance was corrected for prior to break-in achieved by suction. Access resistance (R_s) was typically 1-4 M Ω . 60%-80% R_s compensation (10 μ s lag) and prediction was used to reduce voltage error to less than 10 mV as determined from the product of the peak current and uncompensated R_s . P/5 leak subtraction protocol was used during recording. Signals were pre-filtered with a low-pass Bessel filter at 5 or 10 kHz before digitizing at 20 kHz and recorded with Patchmaster (HEKA, version 2x90.2) on a Windows 7 PC. After break-in, cells were held at -120 mV and tested for stable Na⁺ current with depolarizing 35 ms voltage steps to -10 mV from -120 mV collected every 5 s for up to 5 minutes to allow for a stable level of current prior to vehicle addition. Once stable current levels were achieved, 150 μ L of vehicle was added to the bath via pipette with displaced solution removed via an overflow vacuum line. After approximately 5 minutes, whole cell parameters were checked, and toxin was added via pipette as with vehicle during recording, with vacuum suction removing displaced bath solution. Once apparent kinetic effect plateaued, whole cell parameters were re-checked.

Voltage-dependence of activation was determined from an IV protocol as follows, cells were held at -120 mV then stepped to a single 35 ms voltage step between -80 mV and +60mV ($\Delta+5\text{mV}$) every 2 s. To measure dissociation, gravity fed perfusion with fresh external solution was started at a rate 1-2 mL/min during recording. Cells with stable leak and R_s allowing fitting to a single-exponential function (see below) throughout the experiment were included for analysis. The inactivation of sodium currents from association and dissociation data were fitted with a single-exponential function to determine

Electrophysiology analysis: Electrophysiology data were analyzed and plotted in IGOR 7 Pro (Wavemetrics). Geometric means of kinetic parameters were determined using Excel (Microsoft) and plotted in IGOR 7 Pro. Curve fitting was performed in IGOR Pro 7 as described previously (47, 49). To determine time constants of toxin association and dissociation (τ_{on} and τ_{off} , respectively), sodium currents from depolarizing voltage steps were fit with a single exponential function, equation 1:

$$[1] \quad I_{Na^+} = I_{Na^+_0} + Ae^{-t-t_0/\tau}$$

The time constants of these fits were plotted against real time each voltage step occurred to track association rate by the change in sodium current inactivation with equation 2.

$$[2] \quad \tau_{inact} = \tau_{inact_0} + Ae^{-t-t_0/\tau}$$

The association rate k_{on} was determined by equation 3:

$$[3] \quad k_{on} = \frac{\frac{1}{\tau_{on}} - k_{off}}{[tox]}$$

The dissociation rate, k_{off} , was determined in the same manner as k_{on} , but from sodium currents during dissociation experiments and calculated with equation 4:

$$[4] \quad k_{off} = \frac{1}{\tau_{off}}$$

Affinity was determined kinetically as the dissociation constant K_d via equation 5:

$$[5] \quad K_d = \frac{k_{off}}{k_{on}}$$

Conductance-voltage relationships were determined on normalized current data fit with a Boltzmann equation assuming 22°C equation 6:

$$[6] \quad f(V) = offset + \left(\frac{1}{1 + e^{-\frac{z(V-V_1)}{25.46}}} \right)^n$$

Modeling of the Nav1.7 VSD-IV activated and resting states: Homology modeling of human Nav1.7 channel VSD-IV based on bacterial NavAb channel structure (pdb id: 3RVY) was performed using Rosetta cyclic coordinate descent (CCD) and kinematic (KIC) loop modeling applications with membrane environment specific energy function(50). The activated state model of Nav1.7-VSD-IV was based on NavAb VSD state. The voltage sensors of the homotetramer NavAb are captured in an active state in the crystal structure, so an initial model was built by threading the hNav1.7-VSDIV sequence onto the template of the NavAb voltage sensor. The resting state models of Nav1.7-VSD-IV were generated by shifting Nav1.7 S4 sequence down one, two, and three helical turns with respect to NavAb S4 sequence to simulate one, two, and three step transition of the S4 gating-charge-carrying arginines between resting states(31). The S1-S2 and S3-S4 loops were rebuilt with successive rounds of cyclic-coordinate descent (35) and subsequent kinematic closure protocols (36), followed by a final local all-atom refinement (37). 30,000 models were generated for each VSD state and best 1,000 scoring models were clustered to identify the most frequently sampled conformations. Models

representing top 10 clusters were visually evaluated based on experimental data to select the best models for toxin docking. Resting state models based on TPC1 and NavPas were generated as above with threading of hNav1.7-VSDIV sequence followed by loop modeling of S1-S2 and S3-S4 as described above, but the S4 alignment was not shifted.

Docking of SGTx1 to the hNav1.7-VSDIV resting state model: Docking of SGTx-1 NMR structures (PDB ID: 1LA4) (21) to the TCP1-based resting state of hNav1.7-VSDIV was performed using Rosetta protein-protein docking (37) with membrane environment specific energy function. 50,000 models were generated and the best 10% scoring models were evaluated based on the difference in score between unbound and bound states. The top 10 clusters were to select the best models and visually inspected.

EM-density guided docking of ProTx-II to the hNav1.7-VSDIV activated state: the VSDIV region of the hNav1.7 structure (PDB: 6J8I) and related EM-density map were isolated in UCSF Chimera(51). NMR structures of the toxin (PDB:2N9T) were placed in proximity to the S3-S4 loop and aligned in UCSF Chimera to SGTx-1 docking model prior to docking with Rosetta protein-protein docking (37). ProTx-II – hNav1.7 models were then relaxed to fit the toxin – channel complex into the EM-density using Rosetta EM-relax approach (52). The resulting top 1,000 models were clustered and top scoring models visually inspected.

Figures

Figure 10

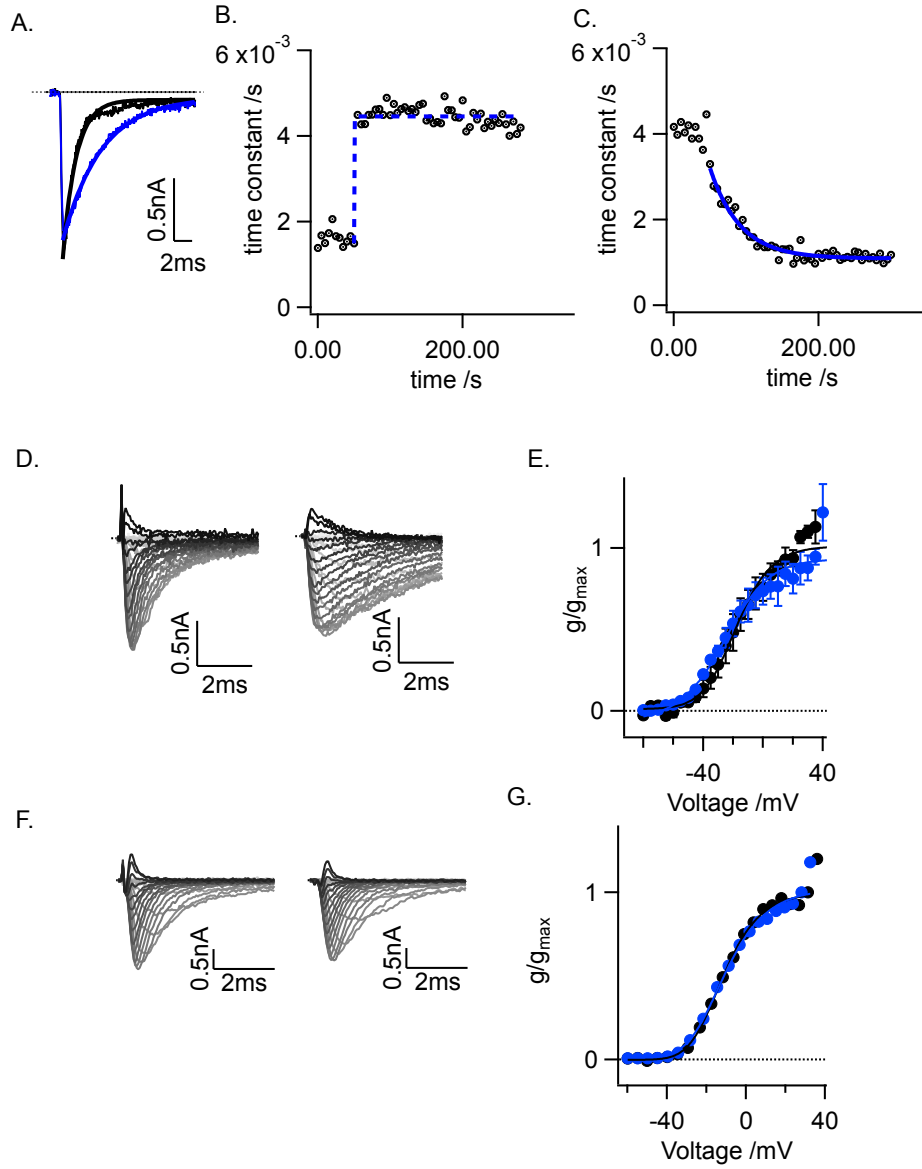


Figure 10: Electrophysiological characterization of SGTx-1 activity on hNav1.7. A) Whole cell voltage-clamp experiments showed 5 μ M SGTx-1 addition produced slowed inactivation of sodium currents during depolarizing voltage steps (-120 mV to +10 mV) compared to vehicle controls, with raw traces and single exponential fits shown before (black) and after (blue) toxin addition. Single exponential fits of time-course of kinetic effect during toxin association (B) and dissociation during washout (C). Toxin association was too rapid to accurately fit the time constant of association (τ_{on}), so the pulse width of 5s was used to estimate an upper bound affinity (n=2). (D) Example traces from control (left) and SGTx-1-treated (right) during an IV protocol. (E) Conductance-voltage relationship in vehicle and SGTx1 treated cells. (F) Example traces from control (left) and GxTx-1-treated (right) during an IV protocol. (G) Conductance-voltage relationship in vehicle (black) and GxTx-1E (blue) (n=1).

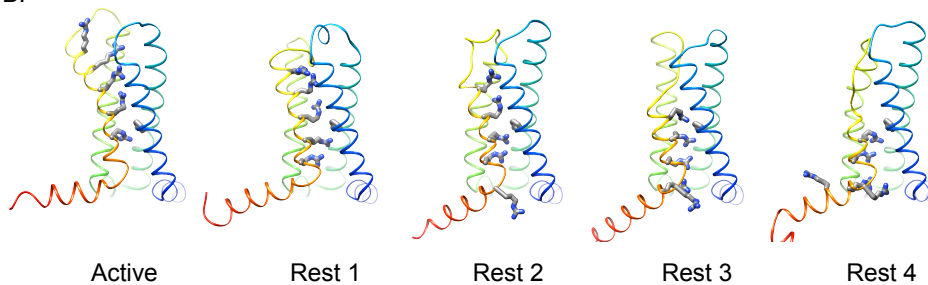
Figure 11

A.

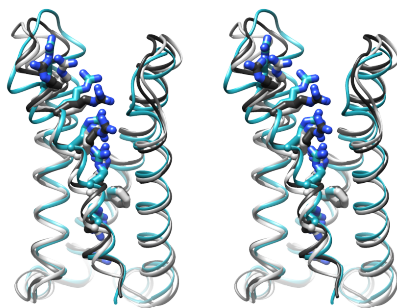
NavAb/2-114	2	YLRITNIVES	FFTKFI	YLIVLNGI	TMGLE	TSKTFMQS	-FGVY	TLFNQ	IVITIFTI	EII	LRIVVHRI	69	
Active/1494-1617	1494	GGCIFDLV	TNQAFDIS	IMVLI	CLNMVTMMVE	KEGQSC	--HMT	EVL	WNVVFI	ILFT	GCVLK	LSLRH	1560
Rest1/1494-1617	1494	GGCIFDLV	TNQAFDIS	IMVLI	CLNMVTMMVE	KEGQSC	--HMT	EVL	WNVVFI	ILFT	GCVLK	LSLRH	1560
Rest2/1494-1617	1494	GGCIFDLV	TNQAFDIS	IMVLI	CLNMVTMMVE	KEGQSC	--HMT	EVL	WNVVFI	ILFT	GCVLK	LSLRH	1560
Rest3/1494-1617	1494	GGCIFDLV	TNQAFDIS	IMVLI	CLNMVTMMVE	KEGQSC	--HMT	EVL	WNVVFI	ILFT	GCVLK	LSLRH	1560
Rest4/1494-1617	1494	GGCIFDLV	TNQAFDIS	IMVLI	CLNMVTMMVE	KEGQSC	--HMT	EVL	WNVVFI	ILFT	GCVLK	LSLRH	1560

NavAb/2-114	70	FFKDPWS	LDFVVA	ISL	VP	TSSG	-----	FEI	LRV	LRV	LRF	RLV	TAVP	114	
Active/1494-1617	1561	YFFTVGWN	IFDFV	VVVIS	IVGM	FLADL	ISTYFVS	PTL	FRV	IRL	ARIGR	ILRL	LVKGAK	1617	
Rest1/1494-1617	1561	YFFTVGWN	IFDFV	VVVIS	IVGM	FLADL	ISTYFVS	-----	PTL	FRV	IRL	ARIGR	ILRL	LVKGAK	1617
Rest2/1494-1617	1561	YFFTVGWN	IFDFV	VVVIS	IVGM	FLADL	ISTYFVS	-----	PTL	FRV	IRL	ARIGR	ILRL	LVKGAK	1617
Rest3/1494-1617	1561	YFFTVGWN	IFDFV	VVVIS	IVGM	FLADL	ISTYFVS	-----	PTL	FRV	IRL	ARIGR	ILRL	LVKGAK	1617
Rest4/1494-1617	1561	YFFTVGWN	IFDFV	VVVIS	IVGM	FLADL	ISTYFVS	-----	PTL	FRV	IRL	ARIGR	ILRL	LVKGAK	1617

B.



C.



D.

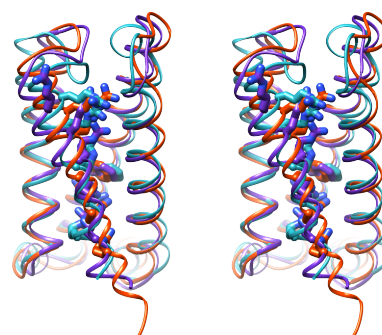
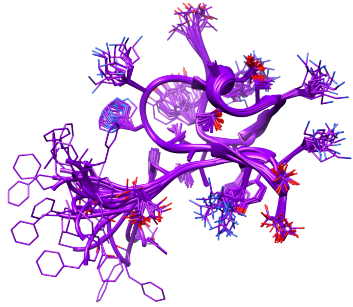


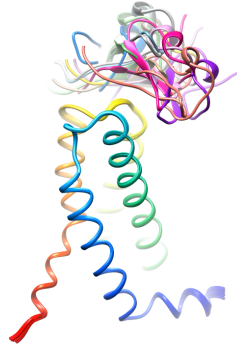
Figure 11: State-modeling of hNav1.7-VSDIV. Homology modeling of hNav1.7-VSDIV based on the structural alignment (A) with the NavAb VSD (PDB ID: 3RVY) (32). Initial resting-state templates were produced from shifting alignment of S4 gating charges by 3 residues to simulate one-turn of the 3-10 helix found in the crystal structure. (B) Renderings of top-scoring active and resting state models as labeled, gating charge arginine and hydrophobic gasket phenylalanine side chains depicted in stick representation. (C) Stereo-view comparison of the active-state VSDIV model (cyan) with recent hNav1.7-VSDIV cryo-EM structure (PDB ID: 6J8I, light grey) (26), and the hNav1.7-VSDIV-NavAb chimera crystal structure (PDB ID: 5EK0, dark grey) (27). (D) Stereo-view comparison of 3 resting-state models generated from NavAb (cyan), Arabidopsis TCP1-VSDII (PDB ID:5E1J (26), orange) (26), and American cockroach NavPas (PDB ID:5X0M, purple) (34).

Figure 12

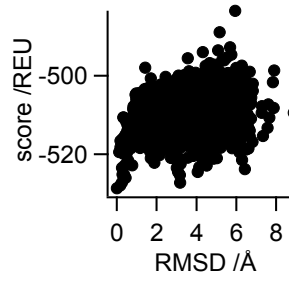
A.



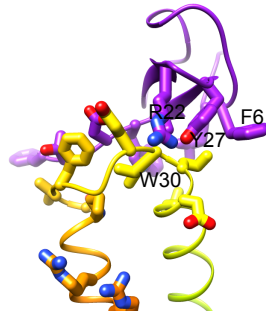
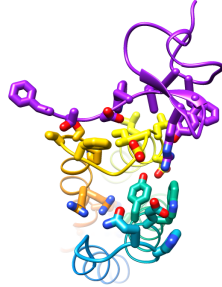
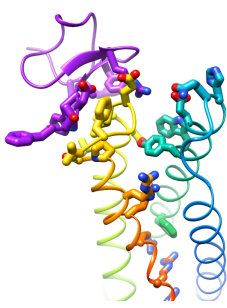
B.



C.



D.



E.

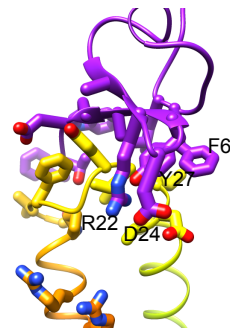
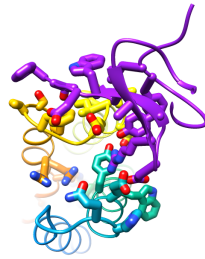
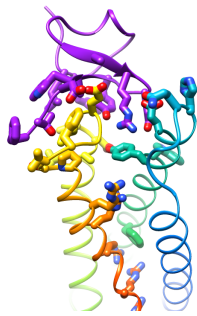
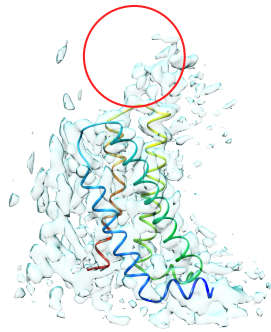


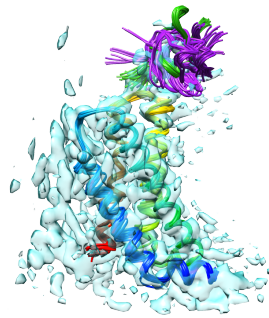
Figure 12: Docking of SGTx-1 to hNav1.7-VSDIV resting state. (A) Rendering of SGTx-1 solution structure (PDB ID: 1LA4) (21). (B) Top 20 scoring clusters centers of 5E1J-based resting state model of hNav1.7 docked SGTx-1 from the 1000 best scoring models showing a broad sampling of toxin positions focused on the S3-S4 loop. (C) Plotting Rosetta score (Rosetta energy units, REUs) vs. RMSD in comparison to the highest scoring pose shows some convergence towards a single docking pose though other high scoring models were present. (D) Multiple views of the docking details of the highest scoring pose with interface residues and gating charge residues shown in stick representation, SGTx-1 is shown in purple and the VSDIV in rainbow. (E) A second high scoring and well-represented pose with SGTx-1 oriented more towards the outside of S3 and making contact with the S2 sidechains.

Figure 13

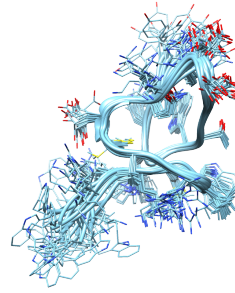
A.



B.



C.



D.

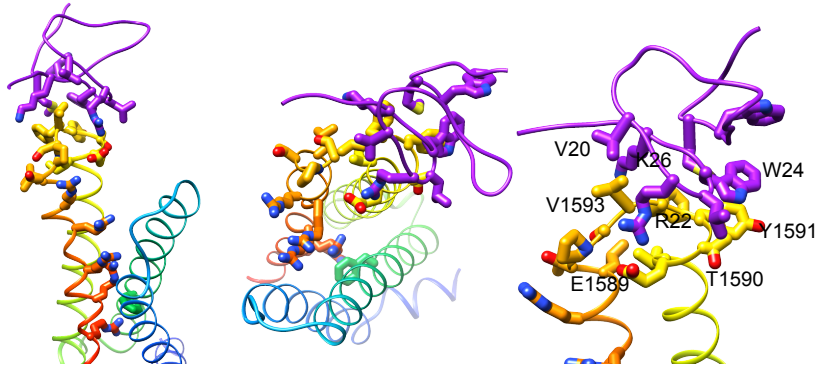


Figure 13: EM-Density guided docking of ProTx-II to hNav1.7-VSDIV active state. (A) Render of the hNav1.7-VSDIV from the cryo-EM structure (PDB ID:6J8I) (26) with the EM-density map in light cyan. Unfilled density believed to be from ProTx-II is circled in red. (B) ProTx-II was docked to the VSD structure from the starting position in green, followed by all-atom minimization with EM-density constraints, with top scoring docking poses shown in purple. (C) Solution structure of ProTx-II used in these simulations (PDB ID:2N9T) (53). (D) Top scoring pose with interface residues and gating charges in stick representation.

Figure 14: hNav1.7-VSDIV toxin comparison. (A) Sequence alignment of potential VSDIV targeting spider toxins SGTx-1, Pn3a, and ProTx-II. The boxed region of high variability near the putative binding interface from these modeling efforts is highlighted. (B) Structural alignment of the resting-state dock of SGTx-1 from Figure 12 (cyan) and the toxin Pn3a (PDB ID: 5T4R, purple) (46) with the highlighted residues in stick representation (boxed region in A) near the toxin-channel interface.

References

- Alexander SP, *et al.* (2015) The Concise Guide to PHARMACOLOGY 2015/16: Voltage-gated ion channels. *British journal of pharmacology* 172(24):5904-5941.
- Bennett DL, Clark AJ, Huang J, Waxman SG, & Dib-Hajj SD (2019) The Role of Voltage-Gated Sodium Channels in Pain Signaling. *Physiol Rev* 99(2):1079-1151.
- Dib-Hajj SD & Waxman SG (2019) Sodium Channels in Human Pain Disorders: Genetics and Pharmacogenomics. *Annu Rev Neurosci*.
- Mulcahy JV, *et al.* (2019) Challenges and Opportunities for Therapeutics Targeting the Voltage-Gated Sodium Channel Isoform Na(V)1.7. *J Med Chem* 62(19):8695-8710.
- Payandeh J & Hackos DH (2018) Selective Ligands and Drug Discovery Targeting the Voltage-Gated Sodium Channel Nav1.7. *Handb Exp Pharmacol* 246:271-306.
- Kwong K, *et al.* (2008) Voltage-gated sodium channels in nociceptive versus non-nociceptive nodose vagal sensory neurons innervating guinea pig lungs. *The Journal of physiology* 586(5):1321-1336.
- Muroi Y, *et al.* (2011) Selective silencing of Na(V)1.7 decreases excitability and conduction in vagal sensory neurons. *The Journal of physiology* 589(Pt 23):5663-5676.
- Bosmans F & Swartz KJ (2010) Targeting voltage sensors in sodium channels with spider toxins. *Trends in pharmacological sciences* 31(4):175-182.
- Murray JK, *et al.* (2015) Engineering potent and selective analogues of GpTx-1, a tarantula venom peptide antagonist of the Na(V)1.7 sodium channel. *J Med Chem* 58(5):2299-2314.
- Wulff H, Christophersen P, Colussi P, Chandy KG, & Yarov-Yarovoy V (2019) Antibodies and venom peptides: new modalities for ion channels. *Nat Rev Drug Discov*.
- Beeton C, *et al.* (2005) Targeting effector memory T cells with a selective peptide inhibitor of Kv1.3 channels for therapy of autoimmune diseases. *Mol Pharmacol* 67(4):1369-1381.
- Tarcha EJ, *et al.* (2012) Durable pharmacological responses from the peptide ShK-186, a specific Kv1.3 channel inhibitor that suppresses T cell mediators of autoimmune disease. *J Pharmacol Exp Ther* 342(3):642-653.
- Kaspar AA & Reichert JM (2013) Future directions for peptide therapeutics development. *Drug discovery today* 18(17-18):807-817.

14. Tanner MR, *et al.* (2017) Prolonged immunomodulation in inflammatory arthritis using the selective Kv1.3 channel blocker HsTX1[R14A] and its PEGylated analog. *Clinical immunology (Orlando, Fla.)* 180:45-57.
15. Bhardwaj G, *et al.* (2016) Accurate de novo design of hyperstable constrained peptides. *Nature* 538(7625):329-335.
16. Catterall WA, *et al.* (2007) Voltage-gated ion channels and gating modifier toxins. *Toxicon* 49(2):124-141.
17. Sokolov S, Kraus RL, Scheuer T, & Catterall WA (2008) Inhibition of sodium channel gating by trapping the domain II voltage sensor with protoxin II. *Molecular pharmacology* 73(3):1020-1028.
18. Wisedchaisri G, *et al.* (2021) Structural Basis for High-Affinity Trapping of the Na(V)1.7 Channel in Its Resting State by Tarantula Toxin. *Molecular cell* 81(1):38-48.e34.
19. Xu H, *et al.* (2019) Structural Basis of Nav1.7 Inhibition by a Gating-Modifier Spider Toxin. *Cell*.
20. Jiang D, *et al.* (2021) Structural basis for voltage-sensor trapping of the cardiac sodium channel by a deathstalker scorpion toxin. *Nature Communications* 12(1):128.
21. Lee CW, *et al.* (2004) Solution structure and functional characterization of SGTx1, a modifier of Kv2.1 channel gating. *Biochemistry* 43(4):890-897.
22. Wang JM, *et al.* (2004) Molecular surface of tarantula toxins interacting with voltage sensors in K(v) channels. *J Gen Physiol* 123(4):455-467.
23. Jung HH, *et al.* (2010) Structure and orientation of a voltage-sensor toxin in lipid membranes. *Biophys J* 99(2):638-646.
24. Bosmans F, Martin-Eauclaire MF, & Swartz KJ (2008) Deconstructing voltage sensor function and pharmacology in sodium channels. *Nature* 456(7219):202-208.
25. Capes DL, Goldschen-Ohm MP, Arcisio-Miranda M, Bezanilla F, & Chanda B (2013) Domain IV voltage-sensor movement is both sufficient and rate limiting for fast inactivation in sodium channels. *J Gen Physiol* 142(2):101-112.
26. Shen H, Liu D, Wu K, Lei J, & Yan N (2019) Structures of human Nav1.7 channel in complex with auxiliary subunits and animal toxins. *Science*.
27. Ahuja S, *et al.* (2015) Structural basis of Nav1.7 inhibition by an isoform-selective small-molecule antagonist. *Science* 350(6267):aac5464.
28. Bowman CL, Gottlieb PA, Suchyna TM, Murphy YK, & Sachs F (2007) Mechanosensitive ion channels and the peptide inhibitor GsMTx-4: History, properties, mechanisms and pharmacology. *Toxicon* 49(2):249-270.
29. Suchyna TM, *et al.* (2004) Bilayer-dependent inhibition of mechanosensitive channels by neuroactive peptide enantiomers. *Nature* 430(6996):235-240.
30. Gupta K, *et al.* (2015) Tarantula toxins use common surfaces for interacting with Kv and ASIC ion channels. *Elife* 4:e06774.
31. Yarov-Yarovoy V, *et al.* (2012) Structural basis for gating charge movement in the voltage sensor of a sodium channel. *Proc Natl Acad Sci U S A* 109(2):E93-E102.
32. Payandeh J, Scheuer T, Zheng N, & Catterall WA (2011) The crystal structure of a voltage-gated sodium channel. *Nature* 475(7356):353-358.
33. Guo J, *et al.* (2016) Structure of the voltage-gated two-pore channel TPC1 from *Arabidopsis thaliana*. *Nature* 531(7593):196-201.
34. Shen H, *et al.* (2017) Structure of a eukaryotic voltage-gated sodium channel at near-atomic resolution. *Science* 355(6328).

35. Wang C, Bradley P, & Baker D (2007) Protein-protein docking with backbone flexibility. *J Mol Biol* 373(2):503-519.
36. Mandell DJ, Coutsiaris EA, & Kortemme T (2009) Sub-angstrom accuracy in protein loop reconstruction by robotics-inspired conformational sampling. *Nat Methods* 6(8):551-552.
37. Bender BJ, *et al.* (2016) Protocols for Molecular Modeling with Rosetta3 and RosettaScripts. *Biochemistry* 55(34):4748-4763.
38. Clairfeuille T, *et al.* (2019) Structural basis of alpha-scorpion toxin action on Nav channels. *Science*.
39. Wisedchaisri G, *et al.* (2019) Resting-State Structure and Gating Mechanism of a Voltage-Gated Sodium Channel. *Cell* 178(4):993-1003.e1012.
40. Mihailescu M, *et al.* (2014) Structural interactions of a voltage sensor toxin with lipid membranes. *Proc Natl Acad Sci U S A* 111(50):E5463-5470.
41. Gao S, *et al.* (2020) Employing NaChBac for cryo-EM analysis of toxin action on voltage-gated Na(+) channels in nanodisc. *Proc Natl Acad Sci U S A* 117(25):14187-14193.
42. Schmalhofer WA, *et al.* (2008) ProTx-II, a selective inhibitor of Nav1.7 sodium channels, blocks action potential propagation in nociceptors. *Molecular pharmacology* 74(5):1476-1484.
43. Xiao Y, Blumenthal K, Jackson JO, 2nd, Liang S, & Cummins TR (2010) The tarantula toxins ProTx-II and huwentoxin-IV differentially interact with human Nav1.7 voltage sensors to inhibit channel activation and inactivation. *Molecular pharmacology* 78(6):1124-1134.
44. Xiao Y, Blumenthal KM, & Cummins TR (2014) Gating Pore Currents Demonstrate Selective and Specific Modulation of Individual Sodium Channel Voltage Sensors by Biological Toxins. *Molecular Pharmacology*:mol.114.092338.
45. Milescu M, Lee HC, Bae CH, Kim JI, & Swartz KJ (2013) Opening the shaker K⁺ channel with hanatoxin. *J Gen Physiol* 141(2):203-216.
46. Deuis JR, *et al.* (2017) Pharmacological characterisation of the highly Nav1.7 selective spider venom peptide Pn3a. *Scientific Reports* 7:40883.
47. Kimball IH, Nguyen PT, Olivera BM, Sack JT, & Yarov-Yarovoy V (2019) Molecular Determinants of μ -Conotoxin KIIIA Interaction with the Voltage-Gated Sodium Channel Nav1.7. *bioRxiv*:654889.
48. Tilley DC, *et al.* (2014) Chemoselective tarantula toxins report voltage activation of wild-type ion channels in live cells. *Proc Natl Acad Sci U S A* 111(44):E4789-4796.
49. Dockendorff C, *et al.* (2018) Synthetic Analogues of the Snail Toxin 6-Bromo-2-mercaptotryptamine Dimer (BrMT) Reveal That Lipid Bilayer Perturbation Does Not Underlie Its Modulation of Voltage-Gated Potassium Channels. *Biochemistry* 57(18):2733-2743.
50. Yarov-Yarovoy V, Schonbrun J, & Baker D (2006) Multipass membrane protein structure prediction using Rosetta. *Proteins* 62(4):1010-1025.
51. Pettersen EF, *et al.* (2004) UCSF Chimera--a visualization system for exploratory research and analysis. *Journal of computational chemistry* 25(13):1605-1612.
52. Wang RY, *et al.* (2016) Automated structure refinement of macromolecular assemblies from cryo-EM maps using Rosetta. *Elife* 5.

53. Henriques ST, *et al.* (2016) Interaction of Tarantula Venom Peptide ProTx-II with Lipid Membranes Is a Prerequisite for Its Inhibition of Human Voltage-gated Sodium Channel NaV1.7. *The Journal of biological chemistry* 291(33):17049-17065.